Fabrication of Quasi-Phase-Matching Waveguides for Blue/Green Generation by Rapid Thermal Annealing of Proton-Exchanged $LiTaO_3$

Cangsang Zhao
B.S. (Physics), Peking University, Beijing, China, 1988
M.S. (Solid-State Physics), Peking University, Beijing, China, 1991
M.S. (E. E.), Oregon Graduate Institute, 1993

A dissertation submitted to the faculty of the
Oregon Graduate Institute of Science & Technology
in partial fulfillment of the
requirements for the degree
Doctor of Philosophy
in
Electrical Engineering

July 1996

The dissertation "Fabrication of Quasi-Phase-Matching Waveguides for Blue-Green Generation by Rapid Thermal Annealing of Proton-Exchanged $LiTaO_3$" by Cang-sang Zhao has been examined and approved by following Examination Committee:

Reinhart Engelmann, Thesis Advisor
Professor

J. Fred Holmes
Professor

Rajendra Solanki
Associate Professor

Don Ackley
Manager, Motorola Inc.

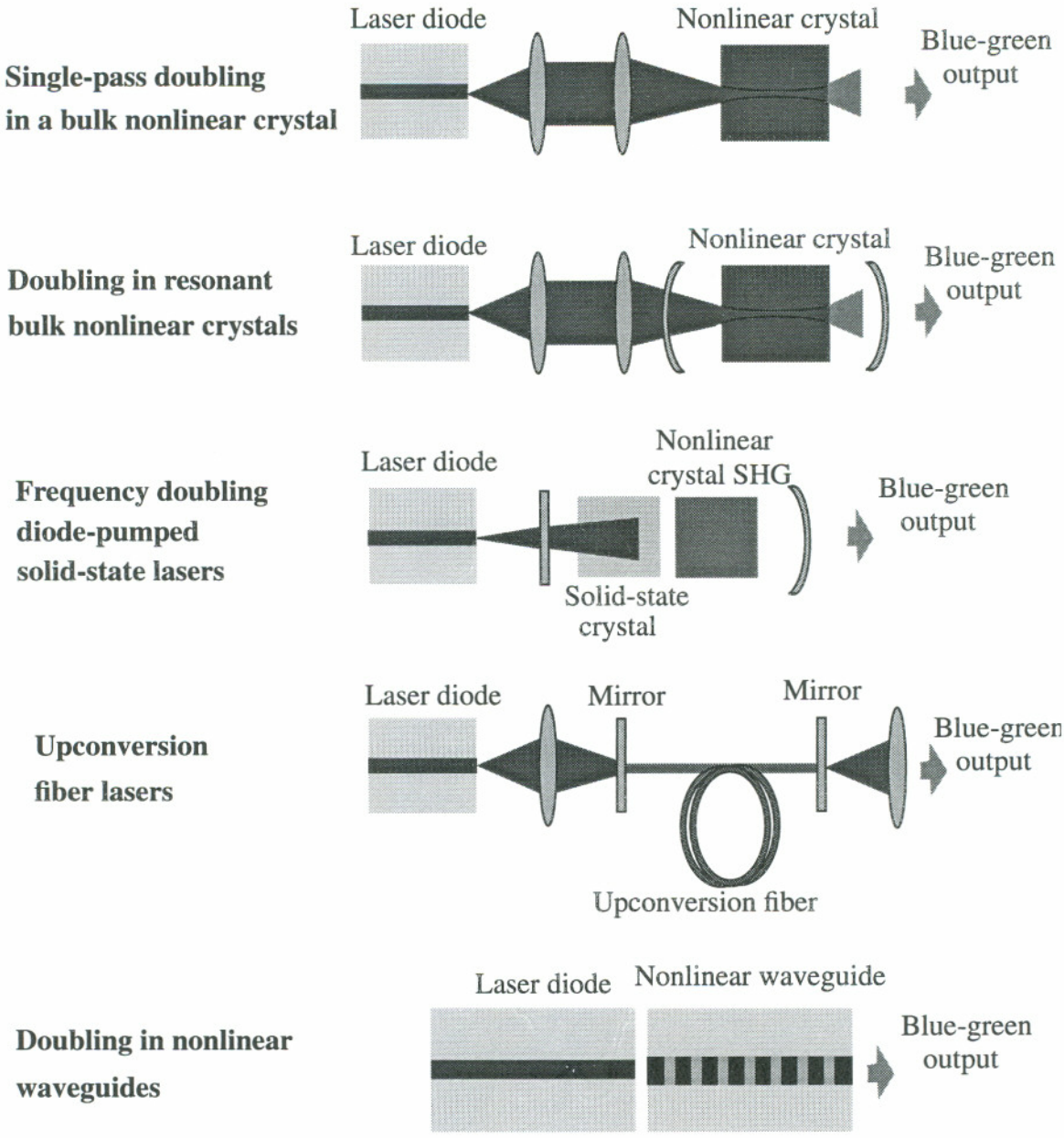

Figure 1.1 Various techniques exist for frequency conversion of laser-diode output, such as single-pass doubling in a bulk nonlinear crystal and doubling in a resonant bulk crystal. Others involve frequency-doubling diode-pumped solid-state lasers, upconversion in a fiber, and doubling in a nonlinear waveguide.

waveguides has the potential for highly efficient blue or green operation in a compact and robust package not only due to its mode-confinement of optical light in the waveguide but

ACKNOWLEDGMENTS

For me to come through all the things in the last five years to this point, there are so many people who have helped and supported me. I wish I could express enough of appreciation here to thank them all.

First of all, I would like to express my gratitude to my supervisor, Dr. Reinhart Engelmann, whose invaluable guidance, support, and funding are critical for the successful completion of this thesis. He taught me not only how to do better scientific research but also how to become a good professional. His encouragement to me to improve my communication skills is extremely beneficial. I consider myself very fortunate and lucky to have such an incredibly supportive professor as my advisor in my five-year period at OGI.

This work was supported in part by a Motorola-University Partnership in Research Grant. I wish to thank Drs. Don Ackley and Fred Richard of Motorola Inc. for this funding and their continuous support on this project. I am very thankful to Dr. Don Ackley's participation on my thesis examination committee and his valuable time and comments. To Dr. Fed Richard, I am very grateful for his patience and efforts to offer me whatever he could from Motorola's side to make this project progress.

I wish to thank Dr. Rajendra Solanki and Dr. J. Fred Holmes for their participation on my thesis examination committee and their valuable time and comments. I would also like to thank Dr. Rajendra Solanki for providing necessary equipment from his lab to my research.

I cannot image where this thesis would be without having the opportunity to use Dr. James Parsons's lab and clean room. (Thank you, Jim) I would also like to thank

Gregg Kruaval for his help and suggestions. His flawless and careful attitude on process experiments certainly had influenced me.

I wish to thank all the Chinese friends at OGI for their friendship, help, and support during my up-and-downs. I am indebted to Song Yu of Princeton Univ. and Baiyan Yang of UCLA for their friendship and help.

I would like to thank George Gollick, Linda Cunningham, and Ed Fisk of Motorola Inc. for fabricating the photo masks and preparing the Ti-masked $LiTaO_3$ wafers. I am grateful to Matthew E. Anderson and Roger Webb of University of Oregon for access to and assistance in using their Ti:Al_2O_3 lasers. I thank Dr. Keren Bergman of Princeton University for letting me use her Ti:Al_2O_3 laser and Radha Venkat for her assistance. (I still owe you two beers, Keren) I thank Dr. John Connolly of David Sarnoff Research Center for his nice suggestions for my research. I would also like to thank Dr. Jack McCarthy of MSE for providing necessary equipment to my research and for his help and advice on SEM equipment. I thank Dr. Jun Ding of MSE for helping me to obtain good SEM images. I also thank Brian Baird of ESI for letting me use his Ti:Al_2O_3 laser.

It is also a pleasure to thank the fellow workers in my research area: Dr. Fredrik Laurell of Sweden, Dr. Williams P. Risk of IBM, Dr. Martin M. Fejer of Stanford, Dr. John D. Bierlein of Dupont, Drs. Eric. J. Lim and Suzanne D. Lau of Unipahse, Dr. Lifeng Li of OSC, Dr. Qibiao Chen of LiCONiX, and Carrie S. Cornish and Dr. Randy Babbitt of Univ. of Washington for their valuable discussions and suggestions. I thank also the Optical Society of America (OSA) for the funding supporting me to attend conferences.

Thanks go to John Hunt for his many helps on electronics and computers. Thanks to Doug David for his help in the machine shop. Thanks to Barbara Olsen, Cathy Feyer,

and Don Johansen for their advice, help, and their patience with my English. Thanks to Jerry Boehme for his advice on electronics. Thanks to all the library staff, for their patience with my English and their outstanding jobs helping me get resources. Thanks to Margaret Day and Julie Wilson for their various helps.

Thanks to my fellow students, Shafqat Ahmed, Zhuoyu Bao, Chris Barbero, Yijun Cai, Feng Chen, John Ferguson, Gengying Gao, Weiran Kong, Raghuraman Ranganathan, Badih Rask, Jin Wu, and Chunyan Zhou for their friendship at EEAP.

Thanks to the basketball friends, Badih, Feng, Long-man, Hui, Money, Hammer, Shi-Liang, Jun, Yijun, Wei, Luke, Love, Baseline Jones, Leo, Haibing, Legs,..., all of them. (You know how much I have enjoyed playing with all of you guys. Dr. Badih, you better watch out your 55-continuous-free-throws record, I am not giving up on it)

Thanks go to my parents Shixing Zhao and Sheng Ye for their many years of support and encouragement which have helped to bring me to this point, to my sister Zhengrong and sister-in-law Jian for their financial support for me to come to USA.

Finally, very special thanks to my wife Liujin Yu for her love, patience, and understanding. Her acute perception on science and research definitely had influences on me.

TABLE OF CONTENTS

LIST OF TABLES

LIST OF FIGURES

LIST OF SYMBOLS

A_{eff}	Effective overlap area
C	the factor of enhancement on bandwidth
C_{ex}^{H}	Uniform proton concentration in the initial PE region
$C^{H}(z, y)$	Proton concentration profile in $H_xLi_{1-x}TaO_3$ layer
C_0^{H}	Maximum proton concentration in $H_xLi_{1-x}TaO_3$ layer with $z, y = 0$
D	Constant duty cycle of the QPM structure
$D(z)$	Duty cycle of the QPM structure at depth z
$D_{ez}(T)$	Proton-exchange diffusion coefficient in the depth direction
D_{az}	Annealing diffusion coefficient along the depth direction
D_{ay}	Annealing diffusion coefficient along the width direction
$E(z, y)$	Mode electric field distribution
$E_1(z, y)$	Mode electric field distribution for the fundamental wave
$E_2(z, y)$	Mode electric field distribution for the second-harmonic wave
$G(z)$	The Fourier coefficient of the spatial frequency of the domain-inversion modulation at depth of z
H^+	Protons
L	Waveguide length
Li^+	Lithium ions
M	Fitting parameter in eq. (3.14)

N	Effective refractive index
N_1	Effective refractive index at the fundamental wavelength
N_2	Effective refractive index at the second-harmonic wavelength
N_{high}	Local mode index in the ion-exchanged region of PS waveguides
N_{low}	Average effective index in the substrate region of PS waveguides
$N_{q_z p_y}$	Channel waveguide mode index
P_1	Initial Fundamental power
P_2	Generated second-harmonic power
P_s	Spontaneous polarization
Q	Fitting parameter in eq. (3.16)
R	Reflectivity
T	Temperature
T_c	Curie temperature
a	Constant length of the reversed domain
$a(z)$	Length of the reversed domain at depth z
c	Vacuum speed of light
d_{33}	The largest nonlinear coefficient
d_e	Proton-exchange depth
d_y	Characteristic annealing depth in the width direction
d_z	Characteristic annealing depth in the depth direction
$f(z)$	Normalized proton profile in the depth direction

$g(y)$	Normalized proton profile in the width direction
k_0	Free-space wave number
l_c	Coherence length
l_u	Length of the un-diffused region in PS waveguides
m	Distributed-Bragg-reflection grating order
n_1	Index of refraction at the fundamental wavelength
n_2	Index of refraction at the second-harmonic wavelength
$n_{eff}(y)$	Effective index, used for the solution of waveguiding in the width direction
n_o	Substrate ordinary refractive index
n_e	Substrate extraordinary refractive index
p_y	Mode order in the width direction
q	Quasi-phase-matching grating order
q_z	Mode order in the depth direction
r	Dispersion parameter
t_a	Annealing time
t_e	Proton-exchange time
w	Mask opening width of the channel waveguide
Δk	Phase mismatch
$\Delta n_e(\lambda)$	Maximum extraordinary-index increase in $H_xLi_{1-x}TaO_3$ layer with $z, y = 0$
$\Delta n_e(\lambda, z, y)$	Extraordinary-index increase in $H_xLi_{1-x}TaO_3$ layer
$\Delta n_{e\text{-}ave}$	Weighted average index increase

$\overline{\Delta n_e}$	Index increase in the equivalent step-index waveguide
Λ	Quasi-phase-matching grating period
α	Coefficient of the linear thermal expansion
γ	Constant relating proton concentration to the extraordinary-index increase in the $H_xLi_{1-x}TaO_3$ layer
$\delta\lambda$	FWHM wavelength acceptance bandwidth
δT	FWHM temperature acceptance bandwidth
δk or u	Fluctuation of the phase-mismatch quantity
ε_0	Vacuum permittivity
η	Conversion efficiency
η_{nor}	Normalized conversion efficiency
η_{norL}	Length-normalized conversion efficiency
κ	Coupling coefficient of DBR
λ_{QPM}	quasi-phase-matching wavelength
λ_{DBR}	Distributed-Bragg-reflection wavelength
λ	Wavelength of the fundamental wave
ξ	Fitting parameter in eq. (3.16)
σ	Square-root mean value of the phase-mismatch variation δk
χ	Fitting parameter in eq. (3.14)
ω_1	Frequency of the fundamental wave
ω_2	Frequency of the second-harmonic wave

LIST OF ACRONYMS

1-D	One dimensional
2-D	Two dimensional
APE	Annealed proton-exchanged
CW	Continuous wave operation of a laser
DBR	Distributed Bragg reflector or Distributed Bragg reflection
FG	Flux grown
FWHM	Full width of half maximum
HG	Hydrothermally grown
PE	Proton exchange or proton exchanged
PS	Periodically segmented
QPM	Quasi-phase-matching
RTA	Rapid thermal annealing
SH	Second harmonic
SHG	Second-harmonic generation
SIMS	Secondary-ion mass spectrometry
TE	Transverse electric
Ti:Al_2O_3	Titanium-doped sapphire
TM	Transverse magnetic

ABSTRACT

Fabrication of Quasi-Phase-Matching Waveguides for Blue/Green Generation by Rapid Thermal Annealing of Proton-Exchanged $LiTaO_3$

Cangsang Zhao

Oregon Graduate Institute of Science & Technology

Supervising Professor: Reinhart Engelmann

Industry has been impatiently waiting for inexpensive, reliable, solid-state, compact blue and green lasers for various applications such as digital printing, high-density data storage, color displays etc. Semiconductor blue-green diode lasers are the desirable candidates. Although a lot of research is being carried out all over the world to realize such laser diodes, the (CW) lifetimes of existing devices are still only about 100 hours at room temperature. It is difficult to anticipate when the life-time problems will be solved. Since high-power infrared diode lasers are available commercially, frequency conversion of diode-laser output is an alternative for such compact devices.

This thesis is aimed at fabricating such compact blue and green lasers by using quasi-phase-matching (QPM) second harmonic generation (SHG) in $LiTaO_3$ crystals.

Practical considerations will be reviewed and discussed for such compact blue and green lasers. Device design modeling has been performed to estimate QPM conversion efficiencies and acceptance bandwidths, to estimate QPM wavelengths, distributed Bragg reflection (DBR) wavelengths, reflectivity, and the concurrent QPM & DBR conditions in a periodically segmented waveguide. Proton exchange (PE) and rapid thermal annealing (RTA) were used to fabricate both periodically domain-inverted structures and QPM waveguides. The domain inversion mechanism has been investigated and discussed. Fabrication of periodically domain-inverted structures in $LiTaO_3$ by PE in benzoic acid followed by RTA has been investigated and developed. It was demonstrated that short-period domain-inverted gratings with considerable inversion depth can be formed by PE in benzoic rather than pyrophosphoric acid followed by RTA. This procedure allowed the fabrication and characterization of first-, second-, and third-order domain inverted gratings. Annealing for extremely short time (~6 s) is crucial for achieving small structures (< 4 μm period) and straight domain walls. A pre-annealing process has been developed to form better QPM structures and allow fabrication of a 2.2 μm depth, 0.6 duty cycle periodically domain-inverted structure with a period of 3.7 μm. Strongly confining waveguides can be fabricated at high temperature (540-610°C) by short-time (6-12 s) RTA, and the simultaneous fabrication of waveguide and domain inversion structures for QPM-SHG is accomplishable by single-step photolithography.

Chapter 1

INTRODUCTION

A broad range of applications need cost-effective, compact blue and green laser sources before their full potential can be realized. These include optoelectronics, high-density optical storage, printing, displays, flow-cytometrey, and medical applications. To be viable, such a source must also deliver high output power with high efficiency and good reliability. Currently, however, there are no ideal blue or green laser sources. Existing blue lasers, such as argon-ion lasers, are too large, inefficient, and costly.

The ultimate blue or green laser sources in terms of size, robustness, efficiency, and cost are semiconductor lasers. Current research on blue and green semiconductor laser diode devices has been concentrated on high-bandgap semiconductor materials such as ZnCdSe/ZnSeS [1] and InGaN [2]. Although a lot of research is being carried out to realize such laser diodes, the CW lifetime of existing devices is still only on the order of about 100 hours at room temperature [1]. Alternative technologies for such laser sources relying on frequency conversion of infrared laser-diode output are, therefore, being pursued. These include frequency doubling of laser-diode output, upconversion lasing in optical fibers, and laser-diode-pumped frequency-doubled solid-state lasers etc. as shown in Fig. 1.1 [3]. Contrary to most of the other techniques the frequency doubling in nonlinear

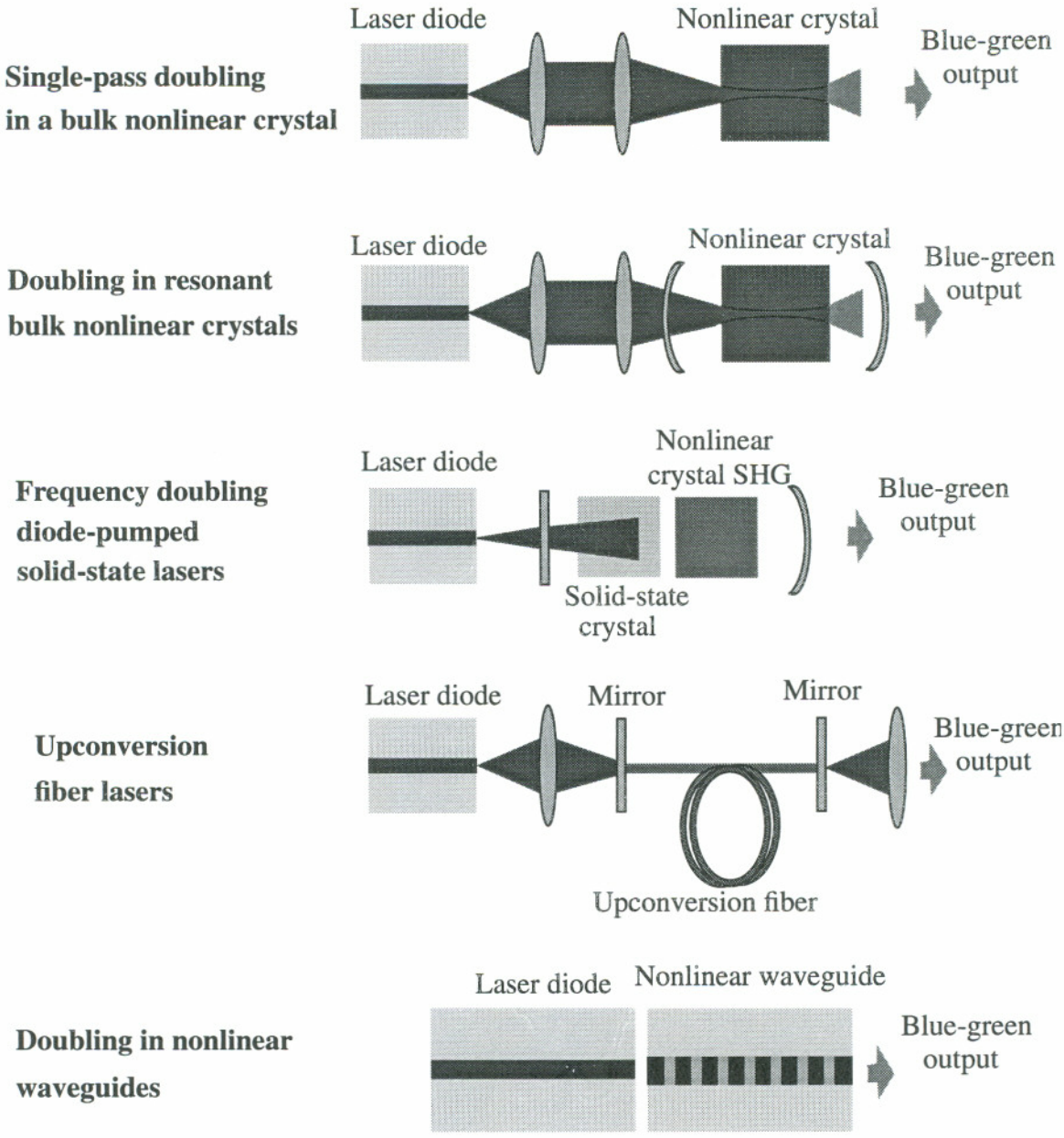

Figure 1.1 Various techniques exist for frequency conversion of laser-diode output, such as single-pass doubling in a bulk nonlinear crystal and doubling in a resonant bulk crystal. Others involve frequency-doubling diode-pumped solid-state lasers, upconversion in a fiber, and doubling in a nonlinear waveguide.

waveguides has the potential for highly efficient blue or green operation in a compact and robust package not only due to its mode-confinement of optical light in the waveguide but

also due to the possibility of realizing a device with laser-diode chip and waveguide integrated together as shown in Fig. 1.1.

Utilizing such a scheme of frequency doubling in nonlinear waveguides, a device configuration in $LiTaO_3$, which promises low cost, compactness, and robustness, has been proposed in this thesis. Aiming at forming such a device, this thesis work is performed in two major perspectives: (i) Device design modeling; (ii) Fabrication process development.

The bulk of this thesis is divided into five chapters. Chapter 2 contains background on quasi-phase-matching (QPM) second-harmonic generation (SHG) theory and practical considerations for device realization. Section 2.2 introduces the concept of the QPM-SHG scheme. Section 2.3 shows the relationship between QPM conversion efficiencies and the material, QPM structure, and waveguide parameters in waveguide devices. Section 2.4 discusses the QPM acceptance bandwidths: wavelength, temperature, and mode-index fluctuation bandwidths. Section 2.5 reviews the practical limitations and several device-design considerations for realizing QPM waveguide devices using diode lasers as pump sources. Section 2.6 presents the proposed device configuration referred to above as a conclusion of the review work presented in section 2.5.

In chapter 3, modeling and simulation of both uniform and periodically segmented (PS) QPM waveguides are performed. Section 3.2 provides modeling of uniformly annealed proton-exchanged (APE) channel waveguides, which gives analytical expressions of mode indices and mode field distributions. Section 3.3 shows a simplified method to simulate PS QPM waveguides, which includes the calculation of QPM wavelength, and distributed Bragg reflection (DBR) wavelength and reflectivity.

Chapter 4 studies domain inversion for QPM structures using RTA of proton-exchanged (PE) $LiTaO_3$. Section 4.2 reviews the domain-inversion fabrication in $LiTaO_3$. Section 4.3 discusses the broad-area domain-formation process and mechanisms. In section 4.4, fabrication of high-quality periodically domain-inverted QPM structures is presented.

Chapter 5 contains fabrication of simultaneous QPM structure and strongly confining waveguides at high temperatures. Section 5.2 introduces high-temperature waveguide fabrication and characterizations. In section 5.3, QPM-SHG of blue light is demonstrated showing high-quality QPM structures and waveguiding.

Finally, chapter 6 summarizes the work of the preceding chapters and gives suggestions for future work in this field.

Chapter 2

QUASI-PHASE-MATCHING SECOND-HARMONIC GENERATION

2.1 Introduction

The accurate design and fabrication of high-quality QPM-SHG devices rely on thorough understanding of the physical principles of the QPM scheme and the device optimization mechanisms. Practical considerations for QPM-device design are also critical for realizing low-cost, compact, and robust products. This chapter provides the fundamental principles of the QPM scheme and the relationships of QPM conversion efficiencies with the material, QPM structure, and waveguide parameters along with an overview of practical considerations for QPM-waveguide design.

2.2 Principles of QPM scheme

Frequency conversion of laser-diode output is possible because of advances in both nonlinear materials and conversion techniques, as well as in infrared laser diode sources such as high power (1 W) coherent lasers and frequency-stable DBR lasers [3]. SHG converts an infrared wave into a blue or green wave, in which a fundamental wave with frequency ω_1 (or wavelength λ) interacts with the second-order nonlinear susceptibility of a material to produce a polarization wave at the second-harmonic (SH) frequency ω_2

$= 2\omega_1$. Since the polarization wave is forced by the fundamental wave, it travels with the same velocity, determined by n_1, the index of refraction at the fundamental wavelength. The polarization wave radiates a free SH wave which travels at a velocity determined by n_2, the index of refraction at the SH wavelength. In general $n_2 > n_1$ because of normal dispersion in the material, so that the fundamental and SH waves travel at different phase velocities. Since the sign of power flow from one wave to the other is determined by the relative phase between the waves, the continuous phase flip between these waves caused by their differing phase velocities leads to an alternation in the direction of the flow of power. This situation is illustrated by curve C in Fig. 2.1. It can be seen that the alternation of the sign of power flow leads to a repetitive growth and decay of the SH intensity along the length of the interaction. The distance over which the relative phase of the two waves changes by π is the coherence length $l_c = \lambda/4(n_2-n_1)$ which is also the half period of the growth and decay cycle of the SH. If the refractive indices can be matched by some means, for example by making use of the birefringence of an anisotropic material, the SH field grows linearly with distance in the medium, and thus the intensity initially grows quadratically, as shown by curve A. This condition is called phase matching [4].

Another method for enabling continuous growth of the SH wave along the device, called QPM involves repeated inversion of the relative phase between the forced and free waves after an odd number of coherence lengths [4, 5, 6]. The phase is thus "reset" periodically so that on average, the proper phase relationship is maintained for growth of the SH. One way to invert the phase is to change the sign of the nonlinear coefficient. A practical approach in ferroelectric crystals like $LiNbO_3$, $LiTaO_3$, and KTP involves forming regions

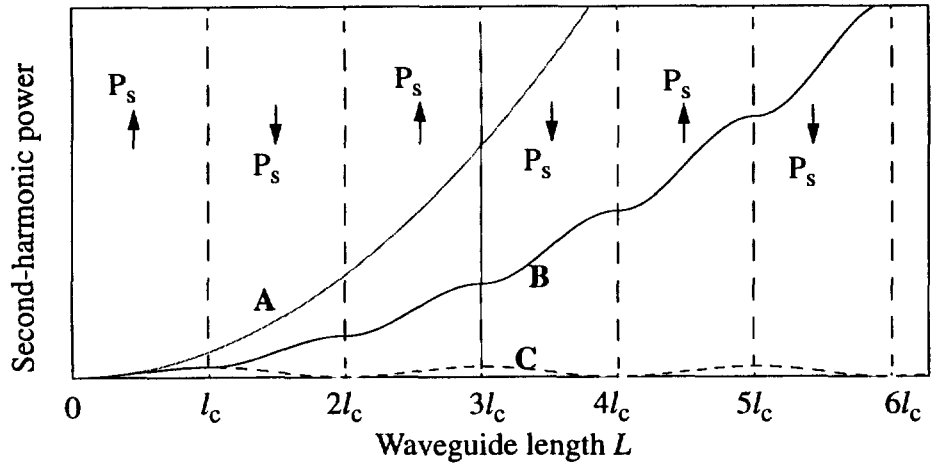

Figure 2.1 Effect of phase matching on the growth of second-harmonic intensity with distance in a nonlinear crystal. A: perfect phase matching in a uniformly poled crystal; C: Nonphase-matched interaction; B: QPM by flipping the sign of the spontaneous polarization every coherence length l_c of the interaction of curve C.

of periodically reversed spontaneous polarization P_s ("domain"). The most rapid growth of the SH, and hence the greatest conversion efficiency, is obtained by changing the sign of P_s (and thus the sign of the nonlinear coefficient) every coherence length. This situation, which we shall call first-order QPM, is illustrated by curve B in Fig 2.1. In general, the phase-matching condition in QPM is expressed as $\Delta k = 0$, where

$$\Delta k = \frac{4\pi}{\lambda}(N_2 - N_1) - \frac{2\pi q}{\Lambda}(q = 1, 2, \dots); \qquad (2.1)$$

here N_1 and N_2 are the effective refractive indices of the fundamental and SH waves respectively, q is the QPM grating order, Λ is the grating period, and Δk is the propagation constant difference. The birefringent phase-matching in homogeneous crystals is achieved

by making $N_1 = N_2$. But in QPM, the additional term $\frac{2\pi q}{\Lambda}$ in equation (2.1) offers a number of advantages:

(1) On the assumption that an appropriate QPM structure can be realized, any wavelength combination within the transparency range of the material can be phase-matched at room temperature.

(2) The polarization of the interesting fields can be chosen such that the largest nonlinear coefficient d_{33} can be used.

(3) Nonlinear materials with small or no birefringence, such as $LiTaO_3$, GaAs, or organics, can be used.

(4) Different orders q of the nonlinear processes can be phase-matched simultaneously in the same waveguide, which allows simultaneous SHG for multiple wavelengths.

(5) The width and shape of the acceptance bandwidth can be tailored by appropriate design of the modulated structure.

(6) A periodic modulation of the nonlinear optical coefficients also leads to periodic modulation of the electrooptic coefficients. This can reduce the detrimental photorefractive effect [7].

Bulk QPM with low efficiency was early demonstrated in stacks of differently oriented GaAs plates [8]. Attempts have also been made to grow $LiNbO_3$ and $LiTaO_3$ crystals with periodically alternating ferroelectric domains [7, 9, 10, 11]. However, in these experiments the conversion efficiencies were modest, primarily due to undesirable varia-

tions in the periodicity of the modulation. The first QPM waveguides in $LiNbO_3$ were reported in 1989 [12, 13, 14, 15]. Since then, several alternative methods for realizing periodically modulated structures have been demonstrated. Materials which have been used, in addition to $LiNbO_3$, include $LiTaO_3$ [16, 17], KTP [18], polymers [19, 20], organic crystals [21], germanium-doped silica [22] and SBN ($Sr_{0.75}Ba_{0.25}N_2O_6$) [23]. Recently, new methods to obtain a periodic modulation of the nonlinearity in the bulk of the crystal have revived the interest in bulk QPM, both for SHG and for difference frequency generation of parametric oscillation [24, 25, 26].

2.3 Conversion efficiencies in QPM waveguides

Probably the most important measure of the a QPM-SHG device is its conversion efficiency. There are three conversion efficiencies which are used in the literature to describe the efficiency of a fabricated QPM-SHG device, which are defined as:

Conversion efficiency $$\eta = \frac{P_2}{P_1} \tag{2.2}$$

Normalized conversion efficiency $$\eta_{nor} = \frac{P_2}{P_1^2} \tag{2.3}$$

Length-normalized conversion efficiency $$\eta_{norL} = \frac{P_2}{P_1^2 L^2} \tag{2.4}$$

where L is the waveguide length, P_2 is the generated SH power, and P_1 is initial fundamen-

tal power.

The basic theory of QPM has been discussed by several authors, with emphasis on various nonlinear optical applications [6, 27, 28, 26, 30] as well as for traveling-wave electrooptic modulators [31]. Fig. 2.2 shows a typical channel waveguide with a periodic domain-inversion configuration and the coordinate system. When the input fundamental

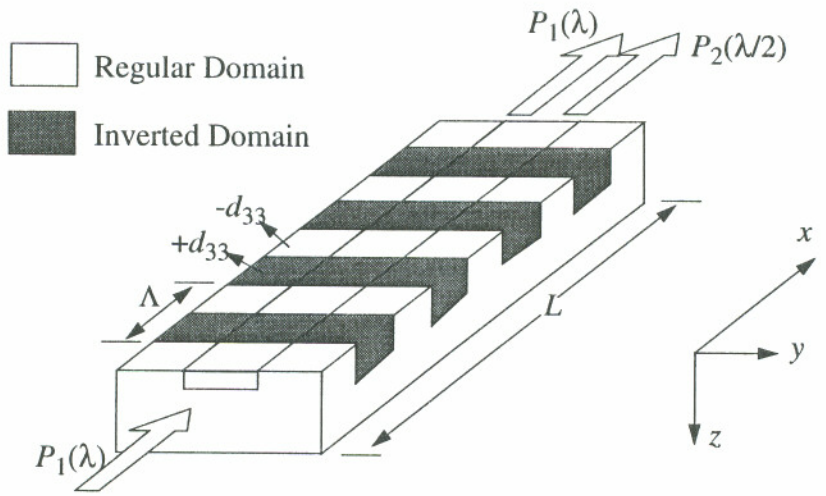

Figure 2.2 QPM channel waveguide

mode is propagating through this waveguide, the SH mode is generated due to the coupling induced by the periodically perturbed nonlinear coefficient as discussed in section 2.2. In most cases P_1 is much larger than P_2 (see section 2.5.1 for detailed discussions). Also, by assuming the slowly varying amplitude equation for governing the growth of the SH field, CW or long-pulse interaction, and no losses for the fundamental or SH modes, the length-normalized conversion efficiency is theoretically given [32, 33] by

$$\eta_{norL} = \frac{8\pi^2 {d_{33}}^2}{N_2 {N_1}^2 c\varepsilon_0 \lambda^2}\left|\int_{-\infty}^{\infty}\int_{-\infty}^{\infty} G(z)\, {E_1}^2(z,y)E_2(z,y)dzdy\right|^2\left(\frac{\sin\left(\frac{\Delta kL}{2}\right)}{\frac{\Delta kL}{2}}\right)^2 \quad (2.5)$$

providing both

$$\eta_{nor} = \eta_{norL}L^2 \quad (2.6)$$

and

$$\eta = \eta_{norL}L^2 P_1 \quad (2.7)$$

where d_{33} is the nonlinear coefficient of the crystal, N_1 and N_2 are the mode effective indices for the fundamental and SH waves, respectively, c is the vacuum speed of light, ε_0 is the vacuum permittivity, λ is the fundamental wavelength, y and z are the channel waveguide width and depth coordinates, respectively, $E_1(z, y)$ and $E_2(z, y)$ are the mode electric field distributions for the fundamental and SH waves, respectively, which are normalized as

$$\int_{-\infty}^{\infty}\int_{-\infty}^{\infty}\left|E_{1,2}(z,y)\right|^2 dzdy = 1 \quad (2.8)$$

$G(z)$ is a function that describes the reduction in the effective nonlinear coefficient when the modulation of the nonlinear coefficient varies with depth. This reduction factor $G(z)$ is

actually the Fourier coefficient of the spatial frequency of the domain-inversion modulation along x that accomplishes QPM,

$$G(z) = \frac{2}{\pi q} \sin [\pi q D(z)] \tag{2.9}$$

where q is the order of the Fourier component used for QPM, also called QPM grating order, and $D(z)$ is the duty cycle of the QPM structure at depth z,

$$D(z) = \frac{a(z)}{\Lambda} \tag{2.10}$$

with $a(z)$ as the length of the reversed domain at depth z, and Λ as the grating period.

According to eq. (2.5), high conversion efficiencies from the material point of view can be obtained in materials with high nonlinear coefficient d_{33}. From the QPM structure point of view, equation (2.5) shows that $D(z)$ needs to be maintained as constant D within the waveguiding region, which means the QPM structure needs to be deep enough with straight domain walls as shown in Fig. 2.3. The influence of the triangular and semi-circular shapes for the domain boundary on the conversion efficiency for QPM-SHG has been reported in Refs. [34] and [35]. Also, the optimum duty cycle D varies with QPM grating orders q. Equation (2.9) shows that the optimum duty cycle for odd q is 50% (actually, as q grows larger, there is more than one optimum duty cycle which makes the sine term equal to 1). For $q = 2$, D needs to be 25% or 75%. Equation (2.9) also shows that

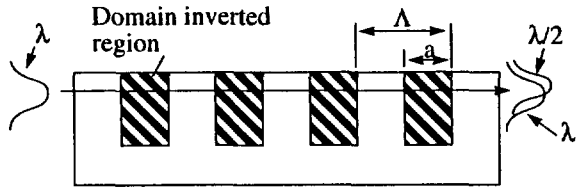

Figure 2.3 Deep straight-domain-wall QPM structure

smaller q gives higher efficiency. According to the phase-matching condition in (2.1) it is seen that the smaller the grating order q, the shorter period the QPM structures have to be fabricated with. For instance, the domain-inversion periods for QPM at 860 nm in $LiTaO_3$ waveguides are 3.7 μm, 7.4 μm, and 11.1 μm for first-, second-, and third-order gratings respectively. One challenge is thus to fabricate deep short-period QPM structures with straight domain walls and proper duty cycles.

By assuming that $D(z)$ is a constant D and the domain inversion structure is deeper than the propagating modes, an important parameter called the effective overlap area A_{eff} can be defined as

$$A_{eff} = \frac{1}{\left| \int_{-\infty}^{\infty} \int_{-\infty}^{\infty} E_1^{\,2}(z,y) E_2(z,y) dz dy \right|^2} \tag{2.11}$$

With the proper D generating $\sin^2[\pi q D(z)] = 1$, eq. (2.5) can be optimized as

$$\eta_{norL} = \frac{32{d_{33}}^2}{N_2{N_1}^2 c\varepsilon_0 \lambda^2 q^2 A_{eff}} \left(\frac{\sin\left(\frac{\Delta kL}{2}\right)}{\frac{\Delta kL}{2}} \right)^2 \tag{2.12}$$

which shows that optimizing A_{eff} is needed to enhance the performance of QPM-SHG waveguides. Usually, when both fundamental and SH waves are transverse magnetic TM_{00} modes, the better the mode confinement, the smaller A_{eff} can be obtained.

2.4 QPM acceptance bandwidths

To evaluate the utility of QPM devices for practical application, it is important to analyze tolerances for variations in temperature and wavelength etc. by evaluating their effects on the efficiency of the device. For a device of total length L containing uniform periods, the phase-matching factor in the expression for the power conversion efficiency is as previously shown in (2.5)

$$\eta_{norL} \propto \left(\frac{\sin\left(\frac{\Delta kL}{2}\right)}{\frac{\Delta kL}{2}} \right)^2 \tag{2.13}$$

where Δk is given in (2.1). The full width at half maximum (FWHM) acceptance bandwidths for several quantities which affect Δk when they are varied can be obtained using the fact that this factor goes to 1/2 when $\Delta kL/2 = 0.4429\pi$. The thus obtained FWHM

wavelength and temperature bandwidths are [36]

$$\delta\lambda = \frac{0.4429\lambda}{L}\left|\frac{N_2 - N_1}{\lambda} + \frac{\partial N_1}{\partial\lambda} - \frac{1}{2}\frac{\partial N_2}{\partial\lambda}\right|^{-1} \tag{2.14}$$

and

$$\delta T = \frac{0.4429\lambda}{L}\left|\frac{\partial (N_2 - N_1)}{\partial T} + \alpha (N_2 - N_1)\right|^{-1} \tag{2.15}$$

where α is the coefficient of the linear thermal expansion defined as $\alpha = l^{-1}\partial l/\partial T$, and the derivatives are evaluated at their respective wavelengths or temperatures. Although N_1 and N_2 are mode indices in the waveguide, to the first-order approximation the material indices and dispersion can be used in (2.14) and (2.15) to calculate the bandwidths. The indices and dispersion in $LiNbO_3$ and KTP can be obtained numerically, for example, from published Sellmeier fits [37, 38, 39]. Using the experimental data of refractive index at different wavelengths [40], the Sellmeier fits for the extraordinary index in $LiTaO_3$ have been performed for the dispersion relations at room temperature (24.5°C)

$$n_e^2 = A_1 + \frac{A_2}{\lambda^2 - A_3^2} - A_4\lambda^2 \tag{2.16}$$

where λ is in nm, n_e is the substrate extraordinary index, and $A_1 = 4.52996$, $A_2 = 84459.7$ nm^2, $A_3 = 203.314$ nm, and $A_4 = 2.40 \times 10^{-8}$ nm^{-2}. Fig. 2.4 shows the fitting curve and the measured data in Ref. [40]. It is seen that a good Sellmeier fit has been obtained. Equation

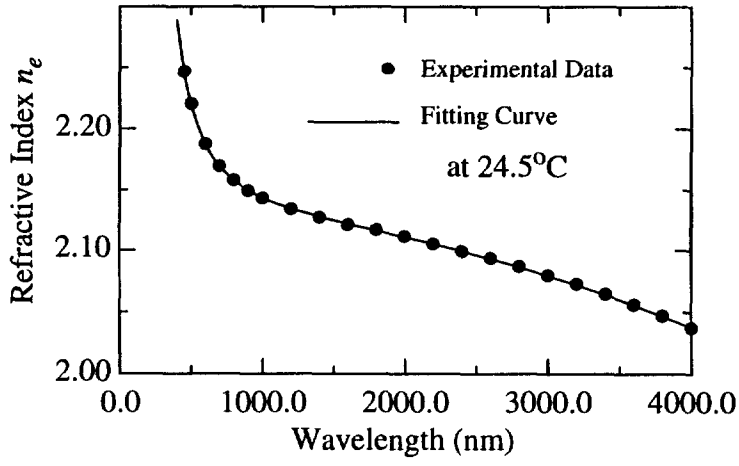

Figure 2.4 Sellmeier fitting for the extraordinary index n_e in $LiTaO_3$

(2.16) will then be used to calculate the extraordinary index n_e in this thesis. Table 2.1 shows the calculated or measured numbers of the wavelength and temperature acceptance bandwidths in the most popular ferroelectric crystals for QPM. At longer wavelengths the spectral and thermal bandwidths tend to increase because of the decrease in dispersion.

Another important acceptance bandwidth is the mode index fluctuation in a non-uniform waveguide, in which phase-matching condition cannot be maintained over long interaction lengths. Since the propagation constant of the guided mode depends not only on the material dispersion, but also on the waveguide dispersion, inhomogeneities in the material refractive and waveguide index profile can seriously limit the phase-matchable

interaction length and consequently, the conversion efficiency. Consider the case of QPM-SHG and assume that due to the waveguide nonuniformity, the fluctuation of the phase-

Table 2.1 FWHM acceptance bandwidth-length product in QPM at 860 nm
* Calculated ★Experimental data

	$LiNbO_3$	KTP	$LiTaO_3$
Wavelength acceptance-length product ($\delta\lambda \cdot L$)	0.07 nm•cm* [37]	0.12 nm•cm* [38], [39]	0.09 nm•cm* Eq. (1.17)
Temperature acceptance-length product ($\delta T \cdot L$)	0.7 °C•cm* [37]	3.0 °C•cm★ [18]	2.9 °C•cm★ [41]

mismatch quantity, $\delta k = (2\pi/\lambda)\,\delta(N_2 - N_1)$, is distributed randomly over the interaction length L, with a Gaussian probability distribution

$$P(\delta k = u) = \frac{1}{\sqrt{2\pi}\sigma} e^{-u^2/2\sigma^2} \tag{2.17}$$

where σ is the square-root mean value of the phase-mismatch variation δk. Then the consequent reduction in the conversion efficiency is given by [42]

$$\eta_{norL} \propto \exp\left(-\sigma^2 L^2/2\right) \tag{2.18}$$

For at least 50% of the SH power to be maintained over the phase-matching length L_{pm},

the maximum value of σ should satisfy $\sigma L_{pm} < 1.2$, and the fluctuations in the mode index mismatch $\delta(N_2 - N_1)$ at $\lambda = 860$ nm must be $< 1.6 \times 10^{-5}$ for $L_{pm} = 1$ cm. This turned out to be the most stringent requirement on waveguides for SHG and has been confirmed experimentally [43].

2.5 Practical considerations for QPM waveguide devices

2.5.1 Limitations on efficiency and power

It is shown in equation (2.5) that when L is small enough ($\Delta kL \ll 1$), η_{norL} becomes independent of waveguide length L, and thus accounts for the material and geometrical aspects of the device: the overlap of the modes, the nonlinear coefficient, and the effective nonlinear coefficient determined by the implementation of QPM. Table 2.2 shows the nonlinear coefficients d_{33} and the theoretical predictions of the length-normalized conversion efficiency η_{norL} assuming a 15 μm^2 (typical value for channel waveguides with $w = 4$ μm) effective overlap area A_{eff} in $LiTaO_3$, $LiNbO_3$, and KTP.

Other important measures for a QPM device are, of course, the normalized conversion efficiency η_{nor} and the generated SH power P_2. Firstly, η_{nor} is a measure of the entire quality of a QPM-SHG waveguide as shown in (2.6) since it takes into account the waveguide length. As discussed in section 2.4, mode-index fluctuation becomes the major reduction factor for conversion efficiency when waveguide length is very long, as shown in eq. (2.18). Usually, L is limited within 1 cm due to the mode index fluctuation present in most of the fabricated waveguides. It should be pointed out that high-quality crystal and

Table 2.2 Nonlinear optical coefficient d_{33} and theoretical η_{norL} @ $\Delta k \ll 1$

Description	Symbol	LiNbO3	KTP	LiTaO3
Nonlinear coefficient	d_{33}	34.4 pm/V [44]	13.7 pm/V [39]	19.4 pm/V [40]
η_{norL} for ideal QPM structure and $A_{eff} = 15\ \mu m^2$	η_{norL}	1200% $cm^{-2}W^{-1}$	308% $cm^{-2}W^{-1}$	417% $cm^{-2}W^{-1}$

uniform waveguide quality is essential for the use of longer waveguides, and consequently for the generation of high normalized conversion efficiency η_{nor}. SH power P_2 seems to be quadratically enhanced by increasing the fundamental power P_1 with given η_{nor} and L as shown in (2.7). But, the photorefractive effect [45, 46, 47], through which high-intensity illumination of a crystal induces a local increase of refractive index, causes problems, often referred to as optical damage. The change of the refractive index results in violation of the phase-matching condition and degraded waveguiding properties. This effect sets an upper limit to the useful power levels in QPM waveguides. Thus, it has been difficult to achieve high conversion efficiency η (>20%) in QPM waveguide devices mainly due to mode index fluctuation and photorefractive effect. Efficient blue-light generation by frequency doubling of infrared light from a titanium-sapphire (Ti:Al_2O_3) or a diode laser has been reported in QPM waveguides fabricated in $LiTaO_3$, $LiNbO_3$, and KTP. Table 2.3 summarizes some high-efficiency QPM devices reported so far. Notice that some length-normalized efficiencies in KTP devices in Table 2.3 are bigger than the theoretical values in Table 2.2. This phenomenon has been carefully investigated in Ref [50] and it was suggested there that the Bb/Ba-exchange process might increase the nonlinear coefficient d_{33} in KTP. Also,

it can be seen that in Table 2.3 the conversion efficiencies in $LiNbO_3$ and $LiTaO_3$ are already close to theoretical predictions as shown in Table 2.2.

Table 2.3 Selected results of high-efficiency QPM waveguide devices

	P_1 *(mW)*	P_2 *(mW)*	L *(cm)*	η (%)	η_{nor} *(%/W)*	η_{norL} *(%/Wcm^2)*	q	Pump source	Refs.
$LiNbO_3$	196	20.7	0.3	10.6	54	600	1st	Ti:Al_2O_3	[48]
KTP	120	9	~0.32	7.5	63	600	1st	Ti:Al_2O_3	[49]
	~50	~3	0.38	6	120	800	1st	Ti:Al_2O_3	[50]
	146	12	0.36	8.2	56	430	1st	Ti:Al_2O_3	[51]
$LiTaO_3$	145	31	1.0	21	150	150	1st	Ti:Al_2O_3	[52]
	72	8	1.0	11	150	150	1st	diode laser	[52]

2.5.2 QPM-SHG using diode lasers as pumps

As has been discussed in the previous section, the difficulty in achieving practical QPM devices results from the stringent tolerances placed on the periodic structure, which includes wavelength acceptance bandwidth, temperature bandwidth, and mode index fluctuation etc. [36]. In order to realize compact QPM-SHG blue and green sources by using laser diodes as the pump source, the QPM tolerances would require the laser diodes to have single transverse and longitudinal modes. Also, reflections from the waveguide and other optical components tend to destabilize the laser and make it difficult to maintain lasing within the narrow acceptance bandwidth for efficient doubling. Furthermore, both the

laser and the waveguide should have accurate temperature controlling and tuning. Approaches to solve this problem are to use stabilized (DBR) lasers or extended-cavity configurations with bulk diffraction gratings as wavelength-selective elements [52, 53] as shown in Fig. 2.5. In both cases a half-wave plate needs to be put in between laser diode

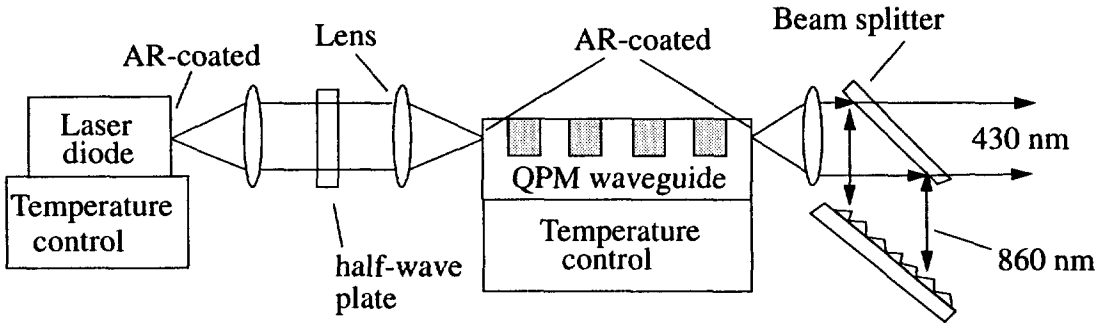

Figure 2.5 Experimental setup for frequency doubling a laser diode in QPM waveguide with a grating feedback systems

and waveguides to convert the transverse electric (TE) mode out of the laser diode to a transverse magnetic (TM) mode into the QPM waveguide, which results in a less-compact and high-cost device comparing to the coplanar-mounted and butt-coupled QPM device to be discussed in section 2.5.5.

2.5.3 PS waveguides for concurrent QPM-SHG and DBR

A more attractive and practical scheme of achieving coherent compact blue or green laser sources is to make a concurrent QPM-SHG and DBR waveguide [54, 55]. The waveguide itself then functions not only as the QPM-SHG device but also as an extended-cavity mirror to stabilize the diode laser source. In the PS waveguide suitable for QPM-

SHG [18], in addition to the non-linear optical coefficient, the linear optical constant (refractive index) is also periodically modulated along the propagation direction. This allows the waveguide to serve simultaneously as a DBR [56, 57, 58]. For a simple PS waveguide to achieve both QPM SHG and Bragg reflection at the same wavelength λ the QPM condition (order q):

$$(N_2 - N_1)\,\Lambda = \frac{q\lambda}{2} \quad (q = 1, 2, \ldots, \infty) \tag{2.19}$$

and the DBR condition (order m):

$$N_1\Lambda = \frac{m\lambda}{2} \quad (m = 1, 2, \ldots, \infty) \tag{2.20}$$

have to be concurrently satisfied. Fig. 2.6 shows the concurrent QPM & DBR wavelengths in a $LiTaO_3$ segmented waveguides by inserting refractive indices of $LiTaO_3$ calculated by (2.16) into equations (2.19) and (2.20) for N_2 and N_1. Careful calculations for N_2 and N_1 will be discussed in chapter 3 for APE channel waveguides in $LiTaO_3$. In this concurrent QPM and DBR scheme, the DBR wavelength λ_{DBR} must coincide with the QPM wavelength λ_{QPM} for efficient generation of SH light. This coincidence is obtained at a particular wavelength by selecting the period that simultaneously satisfies both DBR and QPM conditions (see Fig. 2.6). The temperature tuning rates of the DBR and QPM wavelengths are therefore of practical significance, because achieving coincidence requires

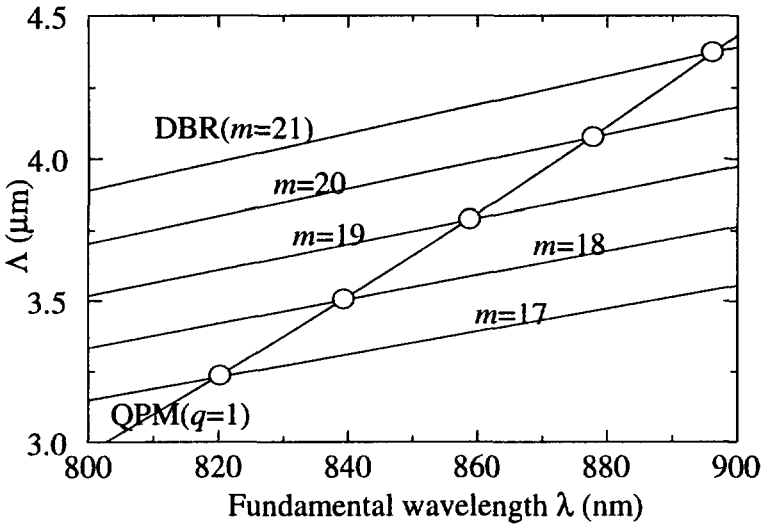

Figure 2.6 PS-waveguide periods which satisfy both DBR and QPM conditions in $LiTaO_3$

adjusting the waveguide temperature to compensate for any processing errors in the waveguide period. Control of the waveguide temperature may also be necessary to ensure stable SH output power. The temperature tuning of the QPM wavelength for a $LiTaO_3$ waveguide was measured as 0.06 nm/°C reported in Ref. [59]. Temperature tuning of the DBR wavelength for a $LiTaO_3$ waveguide can be obtained by taking the derivative with respect to temperature T on equation (2.20) using for simplicity n_1 to replace N_1:

$$\frac{d\lambda_{DBR}}{dT} = \frac{2}{m}\left(\Lambda\frac{dn_1}{dT} + \alpha n_1 \Lambda\right) \tag{2.21}$$

where dn_1/dT was measured as ~1.0 x 10^{-5} /°C [60], α = 1.6 x 10^{-5} /°C [40]. By inserting Λ = 3.8 μm, m = 19, and n_1 = 2.14 into (2.21), the temperature tuning of the DBR wave-

length is estimated to be 0.018 nm/°C. The difference in the tuning rates of the DBR and QPM wavelengths may be used to obtain and maintain coincidence of the DBR and QPM peaks. For example, given a practical temperature tuning of the waveguide by ± 10°C, there is a ± 0.42 nm difference in the QPM and DBR tuning range. Consequently, by using (2.20), it can be found that there would be only ± 0.002 μm fabrication tolerance of the average grating period, which is very difficult to be maintained. The requirement on fabrication tolerance can be relaxed by increasing the QPM acceptance bandwidth. For example, if the QPM acceptance bandwidth increases to 3 nm, the fabrication allowance of the average grating period would become ± 0.007 μm, and, in addition, temperature tuning of the waveguide becomes unnecessary, which would introduce a more robust device configuration.

2.5.4 Broadband QPM scheme

Broadband QPM becomes important in order to ease the tolerances in practical QPM device realization and requirements on the stability of the diode laser. Acceptance bandwidths could principally be increased by reducing interaction length as shown in eqs. (2.15), (2.16), and (2.18). In a uniformly phase-matched nonlinear optical interaction the bandwidth scales inversely with length, however, the conversion efficiency scales quadratically with length, as shown below:

$$\text{Efficiency: } \eta = A \bullet L^2 \tag{2.22}$$

$$\text{Bandwidths:} \quad \delta\lambda,\ \delta T = B \bullet \frac{1}{L} \tag{2.23}$$

where A and B are constants. Thus, with the conversion efficiencies for QPM-SHG, reducing the length results in an unacceptable trade-off between conversion efficiency and acceptance bandwidth. By using a nonuniform QPM structure, on the other hand, it is possible to achieve an approximately linear trade-off between conversion efficiency and bandwidth as such

$$\eta \cong \frac{A' \bullet L^2}{C} \tag{2.24}$$

$$\delta\lambda,\ \delta T \cong B' \bullet \frac{C}{L} \tag{1.25}$$

where C is the factor of enhancement on bandwidth and the factor of decrease on efficiency. C is dependent on the nonuniform QPM structures. It was theoretically analyzed that the bandwidth of QPM can be broadened with approximately a linear trade-off against efficiency using randomized nonlinear gratings [36], linearly chirped nonlinear gratings [61], and pseudorandom polarity reversal (Barker codes) [62]. It was also experimentally demonstrated that broadening of QPM bandwidths can be achieved by using a Barker-code structure (phase reversal after propagation for a certain distance) [63], a segmented QPM structure (with different periods or channel width in each segment) [64], and an optimal periodic domain-inverted structure having preferred phase-matching characteristics,

e.g. a widest acceptance bandwidth at a given peak conversion efficiency [65]. As an example, Fig. 2.7 shows theoretical tuning curves of a conventional and a 13-bit Barker-coded [63] QPM structure in a $LiTaO_3$ PS waveguide with a 0.5 duty cycle. Typical

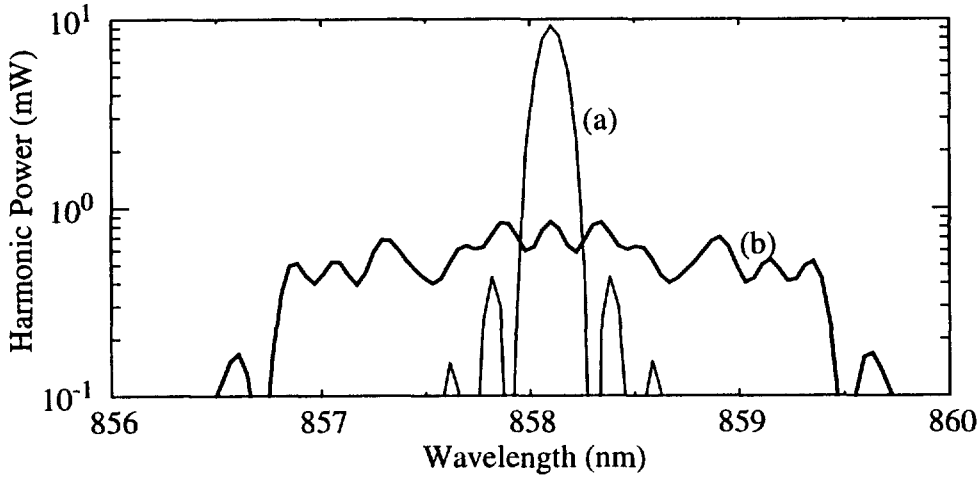

Figure 2.7 Theoretical wavelength-acceptance tuning curves in $LiTaO_3$: (a) 4.9 mm long conventional PS QPM waveguide; (b) 4.9 mm long PS QPM waveguide with 13-bit Barker code.

waveguide parameters (w = 4 μm, d_z = 2.5 μm) have been chosen, and a 100 mW fundamental power has been assumed, which is a typical output power of a commercial high power diode laser. The SH power is calculated assuming one-pass of the fundamental light through the waveguide. In a 4.9 mm long conventional PS QPM waveguide, the peak SH power could approach 9 mW with a 0.16 nm FWHM acceptance bandwidth. On the other hand, in a 4.9 mm long PS QPM waveguide with a 13-bit Barker code, the peak SH power can be as high as 0.9 mW with a dramatic increase of the 3dB acceptance bandwidth to 2.6 nm, which allows for the design of a PS QPM waveguide device operated without any temperature control.

2.5.5 Coplanar-mounted and butt-coupled QPM waveguide devices

High SHG conversion efficiencies and high SH powers have been reported in QPM waveguides fabricated in nonlinear crystals like $LiNbO_3$ [48], $LiTaO_3$ [52], and KTP [50] as had been shown in Table 2.3. The waveguides need to support TM modes that are polarized parallel to the c axis in order to utilize the largest nonlinear coefficient d_{33} in these materials. Using semiconductor diode lasers as pumps in such a QPM scheme has the potential of making compact coherent blue and green sources. Commercially available laser diodes operate in a TE mode with the polarization axis parallel to the plane of the device. A configuration based on coplanar-mounting and butt-coupling (Fig. 2.8) is very promising for realizing a simpler, lower cost, more compact, and mechanically stable device as compared to the configuration in Fig. 2.5. There are two key issues to be

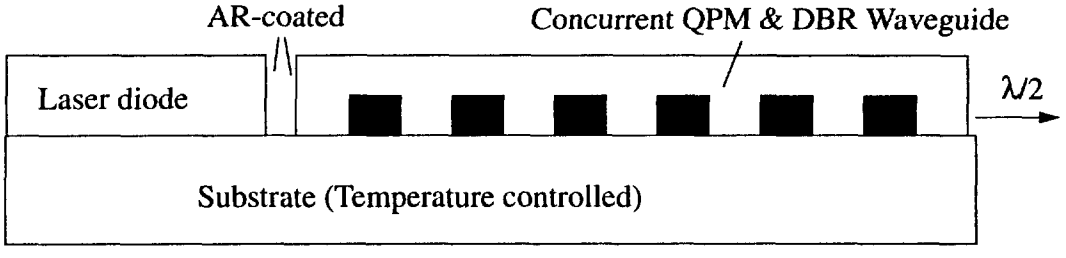

Figure 2.8 Coplanar-mounted and butt-coupled QPM-SHG device configuration

addressed for such a geometry. The first issue is to realize coplanar mounting of the laser diode and the SHG waveguide on a common substrate without requiring an extra element, e.g. a half-wave plate, that would provide the necessary TM-mode excitation in the

waveguide. This approach has been demonstrated [66] with APE $LiTaO_3$ and $LiNbO_3$ waveguides since, there, only TM modes can be supported due to the increase of the extraordinary index and the decrease of the ordinary index in the proton-diffused region of these waveguides and, thus, force TM mode operation if placed within the lasing cavity. The second issue is to integrate a DBR structure with the QPM waveguide for the lasing feedback. Such a scheme has been demonstrated in Rb/Ba-exchanged PS QPM waveguides in KTP [55] thanks to the high anisotropy of ion diffusion, being greater along the c axis [67]. In the PS waveguide, in addition to the non-linear optical coefficient, the linear optical constant (refractive index) is also periodically modulated along the propagation direction. But the Rb/Ba-exchanged waveguides in KTP are relatively deep and support several modes both TE and TM, which makes it difficult to achieve the coplanar-mounted approach in KTP. It has been shown [16, 68] that with proper APE on the -c face of z-cut $LiTaO_3$ the domain-inverted region is closely associated with the proton-diffused region of higher extraordinary refractive index and, thus, in principle allows formation of the periodic domain inversion and waveguiding in a single fabrication process. In addition, such a process has the potential of realizing PS waveguides with a DBR structure by one-step photolithography. The DBR structure thus formed would only have feedback with TM polarization, which is crucial for the device concept described in Fig. 2.8.

2.6 A compact QPM device configuration in $LiTaO_3$

Based on the practical considerations discussed previously, one can expect an integrated compact device which has only a laser diode and a PS waveguide on a single

substrate wafer as shown in Fig. 2.9 by properly patterning the PS structure with a broadband QPM scheme as shown in Fig. 2.7. Furthermore, if the DBR structure can have a

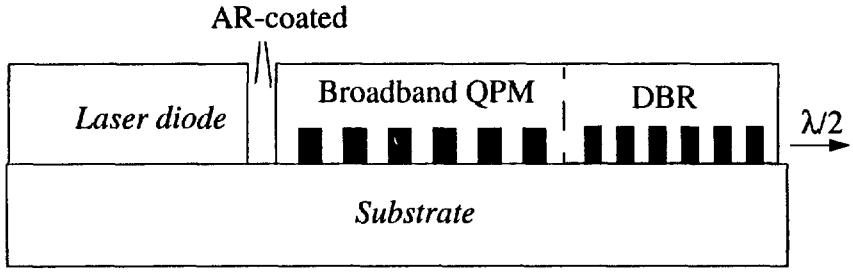

Figure 2.9 Design of a compact QPM device in $LiTaO_3$

high reflectivity on the fundamental wave, the device can be considered as an intra-cavity SHG laser so that the SH power can be much higher than the one-pass SH power. Compared to the design of Fig. 2.8, the advantages of a thus designed device are: (1) Fabrication tolerances are greatly eased due to broadband QPM; (2) Temperature tuning is not necessary due to broadband QPM, and a much more stable operation is expected; (3) Separate optimization of QPM and DBR structures is possible; (4) A potential intra-cavity SHG laser is expected also to enhance conversion efficiency. The limitation on such a device configuration is that its application is limited to low power devices (< 10 mW).

2.7 Summary and conclusions

QPM conversion efficiency and acceptance bandwidths have been analyzed in order to have a better understanding for the waveguide device design. QPM device performance has been related to the material, QPM structure, and waveguide parameters. It has

been found that high-quality QPM structures are required, in particular, to exhibit the lowest-order QPM grating (short period), to have straight domain walls, to be deep enough (comparable with mode sizes), and to have optimized duty cycles. Also, the mode confinement in QPM waveguides needs to be tight to obtain a high conversion efficiency.

A compact QPM device configuration has been proposed in $LiTaO_3$ based on the reviewing of practical considerations for QPM waveguide devices. In this thesis, our work is focused on the device-design modeling (chapter 3), process development of domain-inversion fabrication (chapter 4), and process development of simultaneous QPM structure and waveguide fabrication (chapter 5) for the feasibility of forming such a device configuration.

Chapter 3

MODELING AND SIMULATION OF QPM WAVEGUIDE DEVICES

3.1 Introduction

Conversion efficiency and acceptance bandwidths are the major concerns regarding the performance of a QPM device. In chapter 2, we had reviewed the relationship of them to the material, QPM structure, and waveguide parameters. In this chapter particular interest is placed on building up physical models to calculate the waveguide parameters such as mode indices and mode field distributions for both uniform and PS waveguides, as well as DBR wavelength and reflectivity for PS waveguides for our device design purpose.

3.2 Modeling of uniform APE channel waveguides

As has been discussed in the previous chapter, to design a APE QPM channel waveguide device in $LiTaO_3$, it is essential to be able to estimate the mode indices N_1 and N_2 for the phase-matching condition (2.1) to be satisfied at desired wavelengths and temperatures. The field distributions $E_1(z, y)$, $E_2(z, y)$ need also to be calculated to estimate the conversion efficiency as shown in (2.5).

3.2.1 Index profile

The PE process is an ion-exchange process in which lithium ions (Li^+) in the crystal are replaced by protons (H^+) from a hydrogen-rich source. For $LiTaO_3$, the process can be expressed as

$$LiTaO_3 + x\,H^+ \longleftrightarrow H_xLi_{1-x}TaO_3 + x\,Li^+ \qquad (3.1)$$

When the concentration of protons increases during the exchange, the crystalline cells tend to expand [69], but for the boundary conditions to be satisfied (i.e., in the surface plane, the exchanged layer and the substrate lattice parameters must be identical), elastic deformations must occur and expansion must take place perpendicularly to the surface [70]. This induces stresses in the exchanged layer, which, through the elastic-optic effect and the combination of the piezoelectric and the electro-optic effects, create index variations that add to the index increase because of composition variation. Contrary to the increase of the extraordinary refractive index (n_e), this process results in a local decrease of the ordinary refractive index (n_o). This is then used to form optical waveguides guiding light polarized parallel to the optical axis, the crystal c axis (TM guiding), which is appropriate for exploiting QPM-SHG involving the largest second-order nonlinear coefficient d_{33}.

Fig. 3.1 shows a typical APE waveguide with coordinate system defined according to the crystal axes. The proton concentration in the APE layers needs to be related to the

PE and annealing conditions. This has been investigated using secondary-ion-mass-spec-

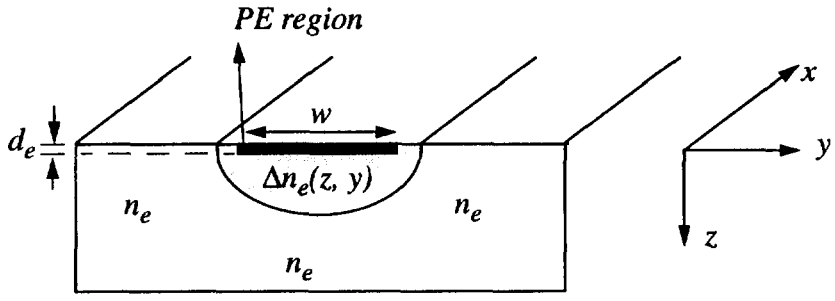

Figure 3.1 Cross-sections of an APE channel waveguide; black: PE region, grey: diffused region

trometry (SIMS) studies [71] at various diffusion and annealing conditions, where PE has been carried out in benzoic acid. It has been found [71] that proton concentration has a step-like profile after PE as indicated in Fig. 3.1, and the PE depth d_e can be estimated as

$$d_e = 2\sqrt{D_{ez}(T)\, t_e} \tag{3.2}$$

where t_e is the PE time, and $D_{ez}(T)$ is the PE diffusion coefficient for the z direction measured in $LiTaO_3$ as [71]

$$D_{ez}(T) = \left(3.309 \times 10^9\right)\exp\left(-\frac{1.080eV}{kT}\right)\left(\frac{\mu m^2}{h}\right) \tag{3.3}$$

For the PE condition used in our studies and throughout this thesis, i.e., 235°C for 40 min

in benzoic acid, we calculated using eqs. (3.2) and (3.3) that $d_e = 0.42$ μm. Since d_e is usually small, it would be reasonable to assume that the proton concentration of the as exchanged region can be approximated by a rectangle of width w, equal to the mask opening width, i.e. ignoring lateral diffusion in the PE process. The annealing process can be described by a two-dimensional (2-D) diffusion from a finite source with the diffusion in the lateral and vertical directions being independent. However, the effective diffusion coefficients for the two directions are different. Thus, the proton concentration profile $C^H(z, y)$ due to the thermal annealing can be modeled as the solution of the following 2-D diffusion equation

$$D_{az}\frac{\partial^2}{\partial z^2}C^H + D_{ay}\frac{\partial^2}{\partial y^2}C^H = \frac{\partial C^H}{\partial t} \tag{3.4}$$

with the depth, width, and the proton concentration of the initial exchanged region as the initial conditions. Here D_{az} and D_{ay} are the diffusion coefficients along the depth and width, respectively, assumed to be constant during the annealing process. For a rectangular initial exchange region (depth = d_e, width = w), the solution to eq. (3.4) is given by [72]

$$C^H(z, y) = C_0^H f(z)\, g(y) \tag{3.5}$$

with normalized distribution functions $f(z)$ and $g(y)$

$$f(z) = \frac{\mathrm{erf}\left((d_e - z)/d_z\right) + \mathrm{erf}\left((d_e + z)/d_z\right)}{2\mathrm{erf}\left(d_e/d_z\right)} \tag{3.6}$$

$$g(y) = \frac{\mathrm{erf}\left((w - 2y)/(2d_y)\right) + \mathrm{erf}\left((w + 2y)/(2d_y)\right)}{2\mathrm{erf}\left(w/(2d_y)\right)} \tag{3.7}$$

where d_z and d_y are the characteristic annealing depths in the vertical and lateral directions, respectively, related to annealing time t_a and diffusion coefficients $D_{az}(T)$ and $D_{ay}(T)$ as such

$$d_z = 2\sqrt{D_{az}(T)\,t_a} \tag{3.8}$$

$$d_y = 2\sqrt{D_{ay}(T)\,t_a} \tag{3.9}$$

$D_{az}(T)$ has been obtained [71] for $LiTaO_3$ as

$$D_{az}(T) = \left(1.284 \times 10^{11}\right)\exp\left(-\frac{1.366eV}{kT}\right)\left(\frac{\mu m^2}{h}\right) \tag{3.10}$$

by using a straight line best-fit of the SIMS data to the Arrhenius law. Although the SIMS data were measured for an anneal temperature range of 360-400°C, the calculated $D_{az}(T)$ = 308 $\mu m^2/h$ extrapolated to 525°C according to eq. (3.10) is comparable to the measured

anneal diffusion coefficient at 525°C of 264 $\mu m^2/h$ obtained from waveguide depth measurement [68]. 525°C is so far the highest temperature at which the anneal diffusion coefficient was measured. So, we decided to use eq. (3.10) for estimating proton diffusion depth in this thesis even for higher temperatures (540-610°C) as will be seen in chapter 5. Even though there is no published data for the temperature dependent diffusion coefficient $D_{ay}(T)$, we can approximately relate $D_{ay}(T)$ to $D_{az}(T)$ according to the ratio of the measured values at 360°C [71] as

$$D_{ay}(T) \approx 0.70 D_{az}(T) \tag{3.11}$$

by assuming that the activation energies are similar for both the z and y directions as has been observed in the PE process [71].

Under the assumption of the conservation of total proton number, C_0^H in eq. (3.5) can be determined as follows:

$$C_{ex}^H \cdot d_e \cdot w = C_0^H \int_{-\infty}^{\infty} g(y)\, dy \int_0^{\infty} f(z)\, dz \tag{3.12}$$

where C_{ex}^H is the uniform proton concentration in the initial PE rectangular region. C_{ex}^H was found to be independent of PE time or temperatures, and the SIMS-measured C_{ex}^H values suggested that about 80% of the Li^+ are exchanged by hydrogen, which gives the

exchange factor x in $H_xLi_{1-x}TaO_3$ system a value of 0.8 in the benzoic-acid PE experiments [71].

The index change in APE layers then needs to be related to the proton concentration. Even though investigations [73, 74] have been done to show qualitatively the phase diagram of the $H_xLi_{1-x}TaO_3$ waveguiding layer on top of a z-cut substrate, there is no published data yet to directly relate the index profile to the proton concentration in the APE layer in $LiTaO_3$. The phase of interesting of the $H_xLi_{1-x}TaO_3$ waveguiding layer for our application is the α phase, where the index increase is approximately proportional to the proton concentrations [73, 74]. Here then we assume that the index increase $\Delta n_e(\lambda, z, y)$ in APE $LiTaO_3$ is proportional to the proton concentration. With this assumption we can write

$$\begin{aligned} \Delta n_e(\lambda, z, y) &= \Delta n_e(\lambda, 0, 0) f(z)\, g(y) \\ &= \gamma C_0^H f(z)\, g(y) \end{aligned} \tag{3.13}$$

with $\Delta n_e(\lambda) = \Delta n_e(\lambda, 0, 0)$ as the wavelength dependent maximum index change at the surface and γ is a constant which relates proton concentration to the extraordinary-index increase in the APE layer. Typical $\Delta n_e(\lambda)$ values at λ = 860 nm are between 0.008 and 0.02 for APE waveguides used for QPM-SHG. Mode distribution measurements for planar APE waveguides in $LiTaO_3$ will be used to approximately determine the γ value in chapter 5 so that the design and simulation of a APE QPM waveguide becomes possible

with given fabrication conditions.

3.2.2 Solution of mode indices

The 2-D waveguiding problem with an index distribution as given by eq. (3.13) usually needs numerical methods to solve for the mode index and field distribution. A practical and quick way of determining the mode index and field distribution is to use the effective index method [75]. By this method a 2-D problem is analyzed in terms of a problem for one-dimensional (1-D) effective waveguides. This latter problem may be solved analytically by simpler methods than required for the 2-D case. The method is accurate especially when the mode-guiding in the vertical direction is much stronger than that in the lateral direction, which is usually the case in the APE waveguides we are dealing with.

Fig. 3.2 shows that a 1-D waveguide with graded-index profile can be first used to

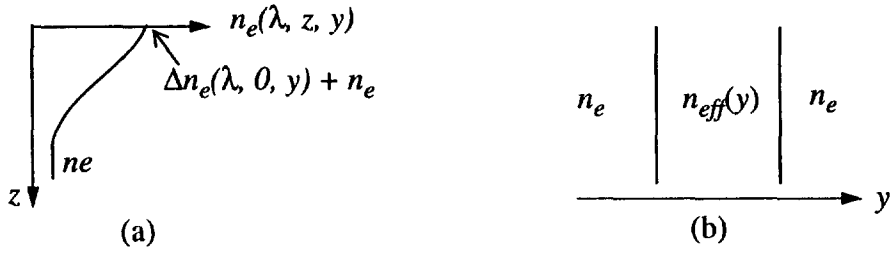

Figure 3.2 Effective index method: (a) graded-index one-dimensional waveguide in z direction with mode index of $n_{eff}(y)$; (b) equivalent planar effective guide in the y-direction

obtain the effective index $n_{eff}(y)$, a function of y. For the lateral guide, $n_{eff}(y)$ is used in the analysis of a planar waveguide.

In order to obtain analytical solutions for mode indices and field distribution, we adopt the approach of Strake et al. [71, 77]. First, we notice that for an APE waveguide the index profile $\Delta n_e(\lambda, z, y)$ described by eq. (3.13) can be approximated by the following function for which the 1-D Helmholtz equation can be solved analytically [76]

$$\Delta n_e(\lambda, z, y) = \Delta n_e(\lambda, 0, 0)\, g(y) \left[1 - M \tanh^2\left(\frac{\chi z}{d_z}\right)\right] \tag{3.14}$$

where M and χ are fitting parameters of the order of unity. The fitting of the APE index profile is shown in Fig. 3.3 for the case $d_e = 0.42$ μm and $d_z = 2.0$ and 3.0 μm, which are typical waveguide depths. It is apparent that the approximation of using (3.14) is acceptable. Better fitting can be obtained for higher d_z/d_e value, which indicates that the index profile approaches a Gaussian function as annealing time increases. It is noteworthy that

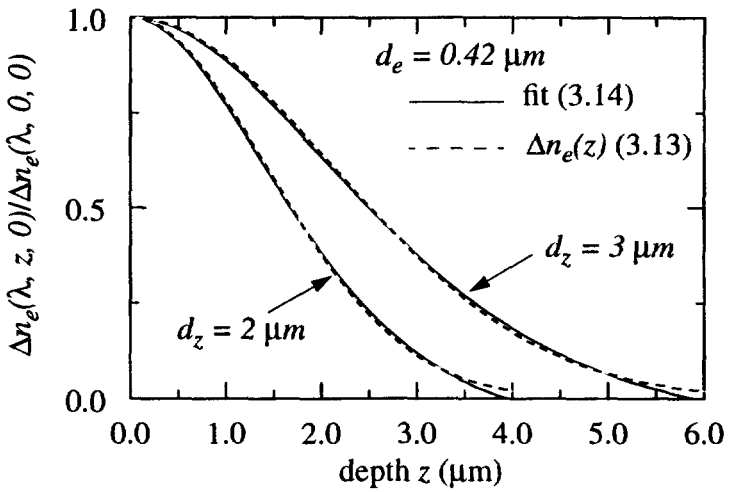

Figure 3.3 Comparison of the index profile $\Delta n_e(\lambda, z, 0)$ from eq. (3.13) and the theoretical fits from eq. (3.14) in the depth direction. For $d_z = 2$ μm, $M = 1.086$, $\chi = 0.983$. For $d_z = 3$ μm, $M = 1.086$, $\chi = 0.991$.

the approximated index profile (3.14) should be limited only to well-annealed waveguides with $d_z/d_e > 3$.

Next, we assume the boundary condition that the electric field at the surface is zero, which is a fairly good assumption owing to the large refractive-index difference between the $LiTaO_3$ crystal and the cover material (air). Thus, the 1-D wave equation in the z direction for such an index profile (3.14) can be solved analytically, and the mode index $n_{eff}(y)$ as a function of y can be determined [76]:

$$n_{eff}^2(y) = n_e^2 + (1-M)\,\rho(y) + (\chi/(\alpha_z k_0 d_z))^2 (2q_z + 1 + \mu'(y))^2$$

with

$$\mu'(y) = \frac{1}{2}\left[1 - \left(1 + 4M\rho(y)\,(\alpha_z k_0 d_z/\chi)^2\right)^{1/2}\right] \qquad (3.15)$$

where $k_0 = 2\pi/\lambda$ is the free-space wave number, n_e is the bulk extraordinary index, $\rho(y) = 2n_e\Delta n_e(\lambda, 0, y)$, and $\alpha_z = n_o/n_e$ for quasi-TM optical polarization in z-cut waveguides, n_o being the ordinary index. q_z is the mode order in the depth direction. The fitting parameters M and χ were determined by fitting the squared hyperbolic tangent profile (3.14) to the profile described by eq. (3.13).

In order to solve for the mode index of the channel waveguide, the effective index profile in the lateral direction $n_{eff}(y)$ is used as the index profile in the 1-D Helmholz equation. To obtain an analytical solution, once again we fit $n_{eff}^2(y)$ with the function

$$n_{eff}^2(y) = n_e^2 + \Delta n_{eff0}^2\left[1 - Q\tanh^2\left(\frac{2\xi y}{w}\right)\right] \tag{3.16}$$

where $\Delta n_{eff0}^2 = n_{eff}^2(0) - n_e^2$ and Q and ξ are the fitting parameters. The fitting of the effective index profile is shown in Fig. 3.4 for the d_e and d_z values as in Fig. 3.3 (for $d_z = 2$ μm, $d_y = 1.8$ μm and for $d_z = 3$ μm, $d_y = 2.5$ μm). Obviously the validity of this approxi-

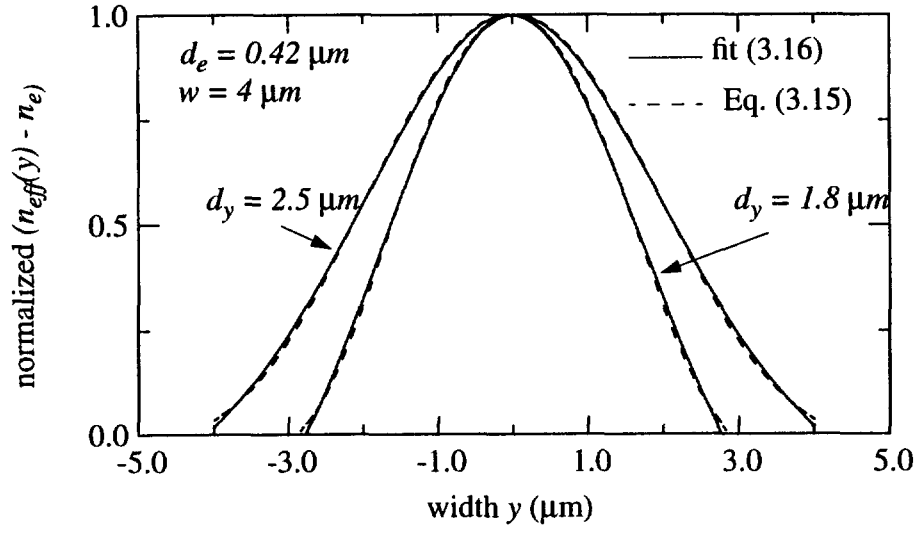

Figure 3.4 Comparison of the effective index profile $\Delta n_{eff}(y)$ according to eq. (3.15) and the theoretical fits from eq. (3.16) in the width direction. For $d_y = 1.8$ μm, $Q = 1.535$, $\xi = 0.659$. For $d_y = 2.5$ μm, $Q = 1.402$, $\xi = 0.659$.

mation is also limited, since the lateral index profile initially resembles a flat top bell shaped function while (3.16) represents a nearly Gaussian function. However, as shown in Fig. 3.4, for narrow width channels (usually $w/d_y < 4$), the approximation appears to be acceptable.

A similar treatment will lead to the expression for the channel waveguide mode index $N_{q_z p_y}$ given by [76]

$$N_{q_z p_y}^2 = n_e^2 + (1 - Q)\,\Delta n_{eff0}^2 + (2\xi/\alpha_y k_0 w)^2 (p_y + \mu)^2$$

with

$$\mu = \frac{1}{2}\left[1 - \left(1 + 4Q\Delta n_{eff0}^2 (\alpha_y k_0 w/(2\xi))^2\right)^{1/2}\right] \qquad (3.17)$$

where $p_y = 0, 1, 2,...$ gives the mode order in the lateral direction, and $\alpha_y = 1$ for quasi-TM polarization. The cutoff condition is obtained when $N_{q_z p_y} = n_e$. On the other hand, the case $M > 1$ or $Q > 1$, which may occur in order to obtain a good index profile approximation near the waveguide axis, leads to cutoff effective index values deviating from n_e. This means, however, no additional restriction because the effective index method is in principle limited to well guided modes, due to the approximate nature of the decoupling of the 2-D wave equation into each dimension. Usually, in the application of QPM-SHG, only the fundamental modes with q_z, $p_y = 0$ will be considered.

3.2.3 Mode field distributions

The mode field distribution in APE channel waveguides can also be modeled by the quasi-analytical technique. Under the effective index approximation, the 2-D wave equation can be separated into two 1-D equations. This results in the mode field distribu-

tion [76]

$$E(z,y) = L_{q_z p_y} Y(y) Z(z;y) \tag{3.18}$$

with

$$Y(y) = \left(\cosh\frac{2\xi y}{w}\right)^{\mu} C_{p_y}^{(\mu)}\left(-i\sinh\frac{2\xi y}{w}\right) \tag{3.19}$$

$$Z(z;y) = \left(\cosh\frac{\chi z}{d_z}\right)^{\mu'} C_{2q_z+1}^{(\mu')}\left(-i\sinh\frac{\chi z}{d_z}\right) \tag{3.20}$$

where $C_{p_y}^{(\mu)}$ and $C_{2q_z+1}^{(\mu')}$ are Gegenbauer polynomials [78], μ can be obtained in eq. (3.17) and $\mu'(y)$ is a function of y according to (3.15). In order to obtain the mode overlap between the fundamental wave and SH wave, the mode distribution is normalized according to (2.8), which leads to the following expression of $L_{q_z p_y}$

$$\left|L_{q_z p_y}\right|^{-2} = \int_{-\infty}^{\infty} Y(y)\,dy \int_{-\infty}^{\infty} Z(z;y)\,dz \tag{3.21}$$

For the case the conversion is TM_{00} to TM_{00} mode, i.e. $q_z = 0$ and $p_y = 0$, $Y(y)$ and $Z(z; y)$ can be simplified as

$$Y(y) = \left(\cosh\frac{2\xi y}{w}\right)^{\mu} \tag{3.22}$$

$$Z(z;y) = \left(\cosh\frac{\chi z}{d_z}\right)^{\mu'} 2\mu'\left(-i\sinh\frac{\chi z}{d_z}\right) \tag{3.23}$$

As an example for d_e = 0.42 μm and d_z = 2 and 3 μm, using the deduced index increase equation (5.6) developed in chapter 5, the calculated intensity profiles of $|Z(z;0)|^2$ and $|Y(y)|^2$ are shown in Fig. 3.5. According to eq. (5.6), the surface index increases are $\Delta n_e(\lambda, z, y)$ = 0.018 and 0.010 for d_z = 2 and 3 μm respectively.

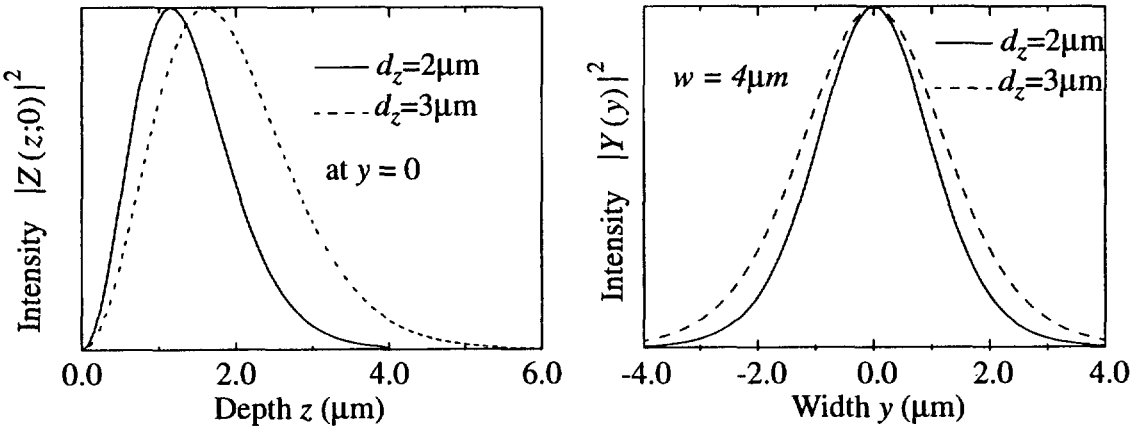

Figure 3.5 Calculated mode intensity distributions of TM_{00} modes. Solid lines are for d_z = 2 μm case and dashed lines are for d_z = 3 μm case. The surface index increase $\Delta n_e(\lambda, z, y)$ is 0.018 for d_z = 2 μm and 0.010 for d_z = 3 μm.

Thus, mode field distributions have been analytically related with the fabrication process conditions, which makes it very convenient to design the fabrication conditions

from the device-design point of view. In reality, there are both interstitial and substitutional diffusions involved in the PE and anneal processes. But, the simple method, which used a single diffusion coefficient to characterize the H^+ diffusions in both PE and anneal processes [71], seems good enough to describe the diffusion process so that reasonable results of simulation and modeling of APE waveguides have been achieved in this thesis.

3.3 Modeling of PS channel waveguides for QPM and DBR

As discussed in the previous chapter, it is very important to predict the mode indices N_2 and N_1 of the PS structure in order to design a concurrent DBR & QPM device. It has been verified [79, 80] that in order to calculate in a PS step-index slab waveguide the effective mode index and the field distribution, one can safely replace the PS waveguide with a uniform waveguide such that its refractive index is equal to the weighted average of the high and low indices. This procedure can also be applied to a PS step-index channel waveguide [80]. Without complicated numerical computation involved this averaged-index approach allows to calculate in a step-index PS waveguide the effective mode indices N_1 and N_2, from which the QPM wavelength and the DBR wavelength can be estimated as shown in eqs. (2.19) and (2.20). Since this approach only gives the information of the effective waveguiding, the intensity of the Bragg reflection will not be derived easily unless complicated numerical calculations are used [79, 80], which is time consuming and also too much cumbersome from the device design point of view. Also, the more realistic graded refractive index distributions in both vertical and lateral directions make it highly complicated or even impossible to find the effective mode indices and the Bragg

reflection intensity in PS channel waveguides. In the following a simplified method will be presented to calculate the mode indices and the Bragg reflection intensity in order to design a device which can simultaneously satisfy DBR and QPM-SHG conditions in a PS channel waveguide with step or graded-index distributions.

3.3.1 Modeling descriptions

In principle, a PS waveguide can be viewed as a lens waveguide whose guided modes periodically diffract and refocus with small diffraction loss [81]. When a mode is propagating in the PS waveguide, it is locally guided or "refocused" in the high index sections, and unguided or "diffracted" in the substrate index sections and it is the guiding region which leads to the overall waveguiding. So it is reasonable to expect a homogeneous waveguide to have an equivalent guiding behavior as the PS waveguide [79, 80]. As pointed out above and illustrated in Figs. 3.6(a) and 3.6(b) for a PS step-index channel waveguide with index increase Δn_e in the segmented rectangular region (width = w, depth = d_z, length = $\Lambda - l_u$) the mode index N and field $E(z, y)$ can be calculated from an equivalent homogeneous step-index channel waveguide with weighted average index increase $\Delta n_{e\text{-}ave}$ in the two sections [80]

$$\Delta n_{e-ave} = D\Delta n_e \tag{3.24}$$

where D is the duty cycle of the PS waveguide. In the high index sections the mode is guided locally as in a homogeneous step-index channel waveguide as shown in Fig. 3.6(c), and the local mode can be described by a mode index N_{high} calculated therefrom.

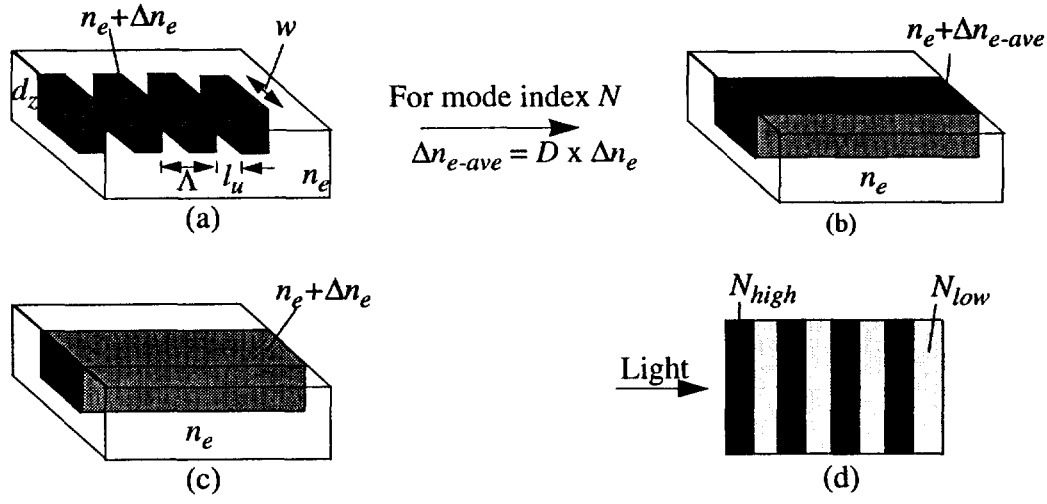

Figure 3.6 Models for PS step-index channel waveguides: (a) PS step-index channel waveguide; (b) Equivalent waveguide for calculating mode index N; (c) Equivalent waveguide for calculating mode index N_{high}; (d) Equivalent layered media for calculating DBR properties.

But in the substrate index sections the mode is actually unguided and cannot be described by a mode index locally. In order to estimate the DBR reflectance in such a waveguide, an average index N_{low}, which describes the mode propagating speed in the substrate index sections, can be calculated from

$$N = DN_{high} + (1 - D) N_{low} \tag{3.25}$$

Thus the reflectivity of the DBR can be calculated as in periodically layered media with index N_{high} and N_{low} as shown in Fig. 3.6(d) using coupled-mode theory[82]

$$R = \tanh^2(\kappa L)$$

with the coupling coefficient κ as

$$\kappa \approx \left| \frac{2\,(N_{high} - N_{low})}{m\lambda} \sin\,(mD\pi) \right| \tag{3.26}$$

Notice that N_{low} may be smaller than the material index n_e. This can be understood in terms of ray-optics since the light propagating in the undiffused sections has always a small angle to the mode propagation direction.

For more realistic graded-index distributions in a PS channel waveguide shown in Fig. 3.7(a), using the approach described above, the mode index N_{high} can be calculated by using the effective index method with a given index profile. As shown in Fig. 3.7(b), an equivalent step-index waveguide having the same local mode index N_{high} as in Fig. 3.7(a) can be found to simulate the guiding behavior in the high-index sections. The index increase $\overline{\Delta n_e}$ in the equivalent step-index waveguide is determined by assuming the depth of the segmented region is equal to the characteristic depth d_z of the graded-index and the

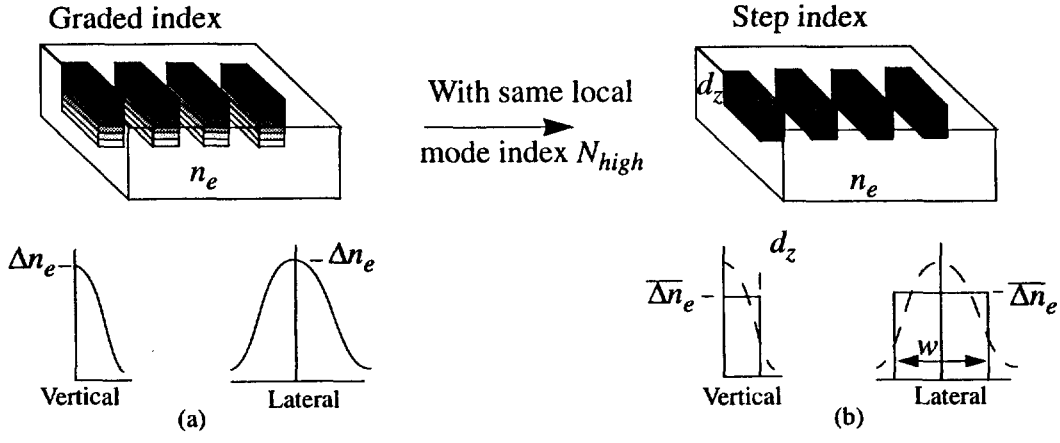

Figure 3.7 Models for PS graded-index channel waveguides: (a) PS graded-index channel waveguide; (b) Equivalent PS step-index channel waveguide.

width is the mask opening width *w*. These assumptions are reasonable especially when the diffusion in the segmented sections are highly anisotropic as in the case of the Bb/Ba-exchanged KTP waveguides [67]. Thus the waveguide problem reduces to a PS-step-index-waveguide problem, which has been solved previously. In real waveguides, as shown in Fig. 3.7(a), approximate index profiles are mostly Gaussian, exponential, or linear functions, and the mode index N_{high} can be calculated analytically (approximately, but accurately enough for mode index calculation). In case of the APE waveguides in $LiTaO_3$ or $LiNbO_3$, the method described in section 3.2 can be used to analytically calculate the mode index, as well as the field distributions. So, the simulation of the concurrent DBR and QPM-SHG device can be accomplished rapidly.

A similar procedure is used to simulate the generated SH modes. For the waveguiding behavior calculation, the index increase $\Delta n_e^{(2\omega)}$ at frequency of 2ω needs to be determined. The dispersion parameter

$$r = \Delta n_e^{(2\omega)} / \Delta n_e^{(\omega)} \tag{3.27}$$

varying depending on crystal and fabrication processes will relate $\Delta n_e^{(2\omega)}$ to the index increase $\Delta n_e^{(\omega)} = \Delta n_e$ at the fundamental wave. Usually r is insensitive to the wavelength with λ in the range of 700-1000 nm and can be determined from experiments.

3.3.1 Comparison of model calculation with experimental data

In a PS waveguide, given the waveguide depth d_z, period Λ, width w, length of the undiffused sections l_u (duty cycle $D = (\Lambda - l_u)/\Lambda$), surface index difference Δn_e and index

profiles, dispersion factor r, and the material indices as a function of wavelength, the model can calculate the performance of the waveguide such as the QPM and DBR wavelengths and the DBR reflectivity.

As has been mentioned in chapter 2, KTP is a promising candidate for fabricating PS waveguides because of its highly anisotropic diffusion characteristic when forming the diffused sections. Also because of that, published data on properties such as QPM and DBR wavelengths and DBR reflectivity are available only on concurrent QPM and DBR PS waveguides in KTP fabricated by Bb/Ba-exchange. Thus, we will test our model calculation on KTP and compare the results with reported experimental data [56], [57].

The index profiles of the ion-exchanged KTP waveguide depend strongly on the process conditions and are difficult to be determined in full detail experimentally, but it is possible to deduce the corresponding equivalent step-index waveguides as described above from optical measurements. This provides, e.g., the index difference $\overline{\Delta n}_e$ and the characteristic waveguide depth d_z as shown in Fig. 3.7(b), which are needed in order to calculate the DBR wavelengths, reflectivity and QPM wavelengths in the PS step-index channel waveguides. In our calculation, the dispersion factor was chosen as 1.59, which gave the best fit of the calculated QPM wavelengths to the measured ones in the range of 800-900 nm [58]. This is going to be demonstrated to be a reasonable value by determining the index difference $\overline{\Delta n}_e$ and depth d_z using the measured DBR wavelength and reflectivity performance reported by Ref. [57].

Only the quasi-TM_{00} modes in both fundamental and SH waves were considered in our calculations. The effective-mode-index method described in section 3.2 has been used to calculate the quasi-TM_{00} modes. The values of the hydrothermally-grown (HG)

and flux-grow (FG) KTP refractive indices as a function of wavelength at room temperature used for the calculations were taken respectively from Ref. [56] and [55].

For a systematic comparison between the results of our model calculations and reported experimental data by others, the various experimental configurations are summarized below:

Configuration A: Measurements of the TM_{00} mode for both 17th-order DBR and 1st-order QPM conditions versus temperature in a 4-μm-wide (w), 4-μm-period (Λ), 0.675-duty cycle (D), and 4.5-mm-long (L) PS waveguide [56]. The waveguide is commercially available and was fabricated by Dupont on HG KTP (Rb/Ba exchanging conditions not available). At room temperature, the measured values are λ_{DBR} = 866.8 nm (m = 17) and λ_{QPM} = 851.2 nm (q = 1), which will be used for generating Fig. 3.8.

Configuration B: Measurements of TM_{00} mode wavelengths for various orders of DBR and 1st order QPM conditions in a waveguide with period Λ [56]. a) The filled circles and the filled squares in Fig. 3.9 are, respectively, the DBR wavelengths and QPM wavelengths measured in HG-KTP waveguides fabricated by Dupont (Rb/Ba exchanging conditions not available but same as configuration A with a length L = 4.5 mm; width w = 4 μm; periods Λ = 3, 4, 5, and 6 μm; and undiffused section length l_u = 1.3 μm. b) The open circles in Fig. 3.9 are the DBR wavelengths measured from FG-KTP waveguides fabricated by ion exchange in a mixed Rb/Ba salt bath having a molar composition of 97%Rb/3%Ba at ~340°C for 45 min. The waveguides from the FG sample were L = 9.3 mm long, with w = 4.5 μm, Λ = 5.5 μm, and l_u = 2.5 μm.

Configuration C: Measurements of TM_{00} mode wavelength and the reflectivity performance for the 3rd-order DBR condition in FG-KTP waveguides fabricated by ion

exchange in a mixed Rb/Ba salt bath having a molar composition of 95%Rb/5%Ba at 350°C for 45 min with w = 4 μm, Λ = 0.7 μm, l_u = 0.3 μm, and various lengths [57]. The wavelength value is λ_{DBR} = 860 nm (m = 3). The best fitted curve of the reflectivity data will be reproduced in Fig. 3.10, solid line.

For the waveguide described in configuration A, d_z and $\overline{\Delta n_e}$ are the only unknown parameters when viewing the waveguide as an equivalent step-index PS waveguide as shown in Fig. 3.7(b). Using our model calculation, it can be found that for the waveguide to have the measured λ_{QPM} = 851.2 nm (q = 1) the parameter points ($\overline{\Delta n_e}$, d_z) would correspond the solid curve (Fig. 3.8). Similarly, for the waveguide to have the measured λ_{DBR} = 866.8 nm (m = 17), the parameter points ($\overline{\Delta n_e}$, d_z) would correspond the dashed curve (Fig. 3.8). The intersection point (0.009, 3.9) of these two curves provides the unknown waveguide parameters, which are typical for the Rb/Ba-exchange process and consistent

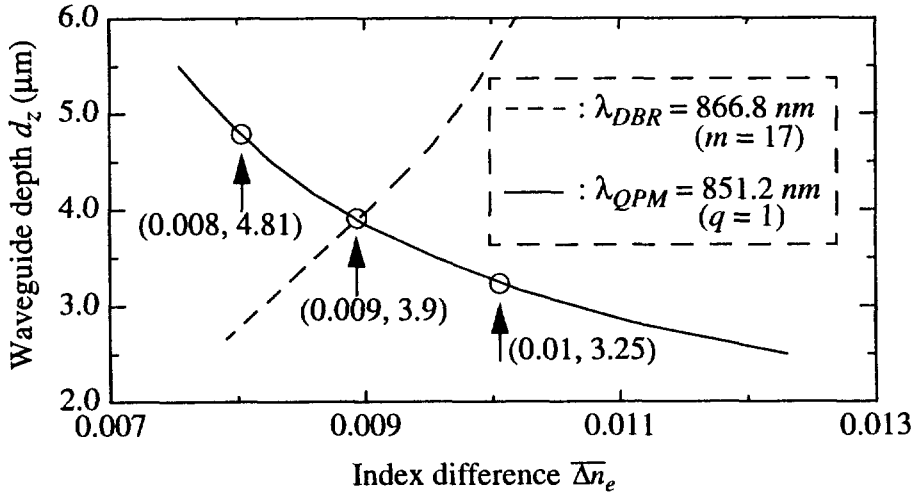

Figure 3.8 Calculated parameter points of waveguide index difference $\overline{\Delta n_e}$ and depth d_z corresponding to the 17th-order TM_{00} polarization DBR wavelength of 866.8 nm (dashed curve) and the 1st-order QPM wavelength of 851.2 nm (solid curve) in a periodically segmented (PS) waveguide with w = 4 μm, Λ = 4 μm, D = 0.675 on hydrothermally grown (HG) KTP [56].

with the measured refractive index distributions [67], [83].

The results of Fig. 3.8, i.e. d_z = 3.9 μm and $\overline{\Delta n_e}$ = 0.009 as the waveguide parameters, have been used to calculate the DBR and QPM wavelengths vs. waveguide periods Λ (l_u = 1.3 μm) in order to compare the calculations with the measured data in configuration B. The DBR wavelengths in HG-KTP waveguides with the same Rb/Ba-exchanging conditions as that in configuration A (configuration Ba) can be calculated as the solid lines in Fig. 3.9, which fit the reported experimental data points very well (Fig. 3.9: filled circles). The calculated QPM wavelengths in these waveguides are indicated by the long-dashed curve in Fig. 3.9 which fits well to the measured QPM wavelengths (Fig. 3.9: filled

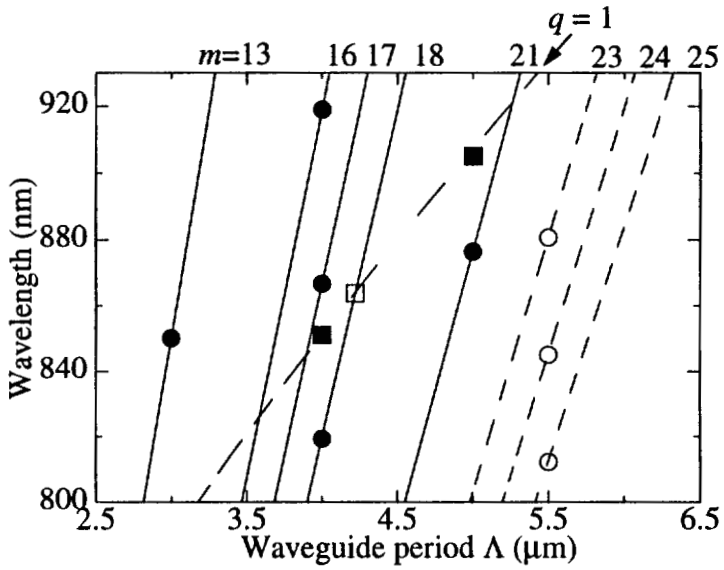

Figure 3.9 Calculated variation of TM_{00} polarization DBR wavelength with grating period Λ. DBR wavelengths for both hydrothermally grown (HG) KTP waveguides (solid lines, l_u = 1.3 μm) and flux-grown (FG) KTP waveguides (dashed lines, l_u = 2.5 μm) are shown. Data points are the measured DBR wavelengths for both HG-KTP waveguides (filled circles, l_u = 1.3 μm) and FG-KTP waveguides (open circles, l_u = 2.5 μm) [56]. The long-dashed line shows the calculated variation of the 1st-order QPM wavelength vs. period (l_u = 1.3 μm) in HG-KTP waveguides. The filled squares indicate experimentally measured 1st-order QPM wavelengths in HG KTP waveguides [56]. The open square is an example of a concurrent QPM/DBR-waveguide design.

squares) in the same HG-KTP waveguides with the periods of 4 and 5 μm. Also, by assuming the same $\overline{\Delta n_e}$ and d_z in Rb/Ba-exchanged FG-KTP waveguides (configuration Bb), the calculated DBR wavelengths (dashed lines in Fig. 3.9) fit quite well to the reported experimental data on FG KTP (Fig. 3.9: open circles).

The model also allows to calculate the DBR reflectivity vs. grating length in PS waveguides, and the calculated results on a 0.7-μm-period PS waveguide in FG KTP can be compared with the experiment described in configuration C. As predicted by coupled-mode theory, the reflectivity is calculated from eq. (3.26). In Fig. 3.10, by assuming $\overline{\Delta n_e}$ = 0.009 and d_z = 3.9 μm (Fig. 3.8), our calculation resulted in $\kappa = 4.56\ mm^{-1}$ (filled circles), which is almost in perfect agreement with the best fitted solid curve of $\kappa = 4.5\ mm^{-1}$ obtained from the experiment [34]. This agreement shows that the dispersion factor r = 1.59 used in our calculation is reasonable. In order to show the sensitivity of the model calculation, we arbitrarily chose two points, (0.008, 4.81) and (0.01, 3.25), on the QPM curve (solid) of Fig. 3.8, calculated the reflectivity vs. wavelength for these two points, as shown in Fig. 3.10 as the dashed curve and thick-solid curve, respectively. It is clearly demonstrated that the actual calculated point (0.009, 3.9) fits significantly better. Also, the calculated 3rd-order DBR wavelength in this case is 860.05 nm, which is very close to the wavelength of 860 nm measured in configuration C [57]. Conversely, from the experimental results of 3rd-order λ_{DBR} = 860 nm and $\kappa = 4.5\ mm^{-1}$ for the TM_{00} mode in the 0.7-μm-period PS waveguides in FG KTP [57], the ion-exchanged waveguide parameters $\overline{\Delta n_e}$ and d_z can be determined as shown in Fig. 3.11, in which the solid curve corresponds to the parameter points governed by λ_{DBR} = 860 nm (m = 3) and the dashed curve corre-

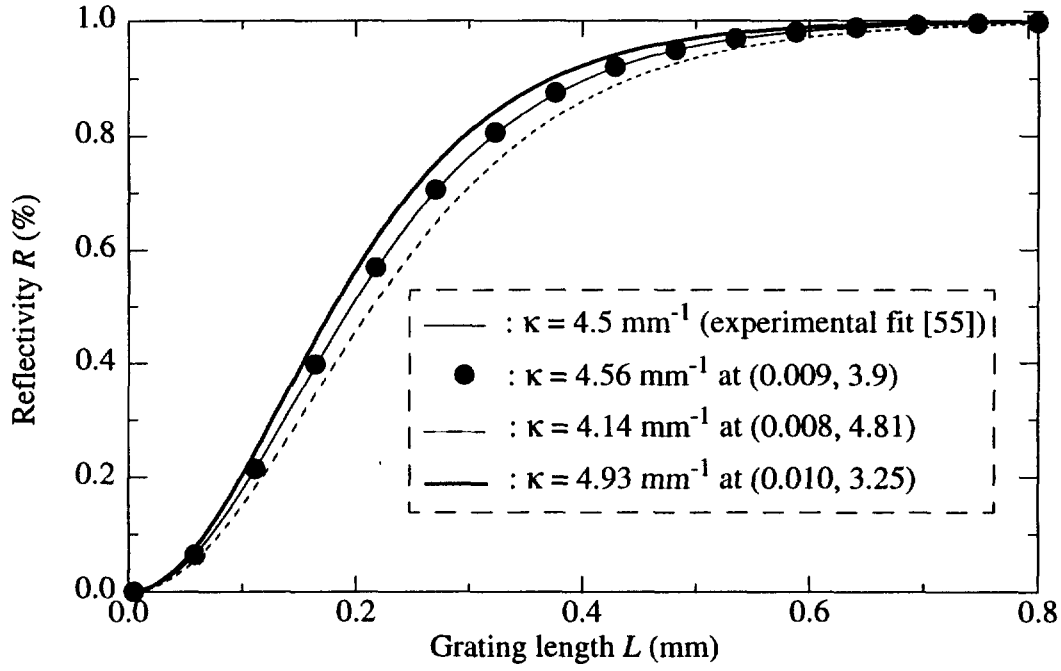

Figure 3.10 Reflectivity vs. DBR grating length in a 4-μm-wide, 4 μm-period ion-exchanged PS waveguide on flux grown (FG) KTP. The solid curve gives the best fit ($\kappa = 4.5$ mm^{-1}) to the experimental data [57]. The filled circles are the calculated reflectivity ($\kappa = 4.56$ mm^{-1}) with waveguide parameters $\overline{\Delta n}_e$ = 0.009, $d_z = 3.9$ μm. The thick-solid line is the calculated reflectivity ($\kappa = 4.93$ mm^{-1}) with $\overline{\Delta n}_e = 0.010$, $d_z = 3.25$ μm and the dashed line is the calculated reflectivity ($\kappa = 4.14$ mm^{-1}) with $\overline{\Delta n}_e = 0.008$, $d_z = 4.81$ μm.

sponds the parameter points governed by $\kappa = 4.5$ mm^{-1}. The deduced waveguide parameters are $d_z = 3.76$ μm and $\overline{\Delta n}_e = 0.009$, very close to the numbers determined from configuration A (Fig. 3.8).

With a PS step-index channel waveguide as shown in Fig. 3.7(b) exhibiting high-index sections with step-index functions in both the vertical and lateral direction ($w = 4$ μm, $d_z = 3.9$ μm, $\overline{\Delta n}_e = 0.009$, dispersion factor $r = 1.59$, and a spacing $l_u = 1.3$ μm), an example of concurrent DBR ($m = 18$) and QPM ($q = 1$) period Λ and fundamental wavelength λ can be calculated as 4.220 μm (duty cycle $D = 0.65$) and 863.3 nm, respectively

(open square in Fig. 3.9). With Rb/Ba-diffused waveguides in KTP, temperature tuning allows one to shift the relative position of λ_{DBR} (m =18) and λ_{QPM} (q =1) by 0.051 nm/°C [56]. Consequently, if one is constrained to temperature tuning of the KTP waveguide by say ± 10°C, then, at the center of the temperature band, λ_{DBR} (m =18) and λ_{QPM} (q =1) should match within 0.51 nm. This corresponds to a fabrication tolerance for the average grating period of ± 0.0024 μm deviation from 4.220 μm using equation (2.20). At 863.8 nm, the calculated material index n_e is 1.839, and the effective mode index N_{00} is 1.842; N_{high} and N_{low} are 1.845 and 1.837 respectively, which can be used to calculate the DBR reflectivity. Notice that N_{low} is less than the material index n_e = 1.839, which is predicted by its definition from eq. (3.25).

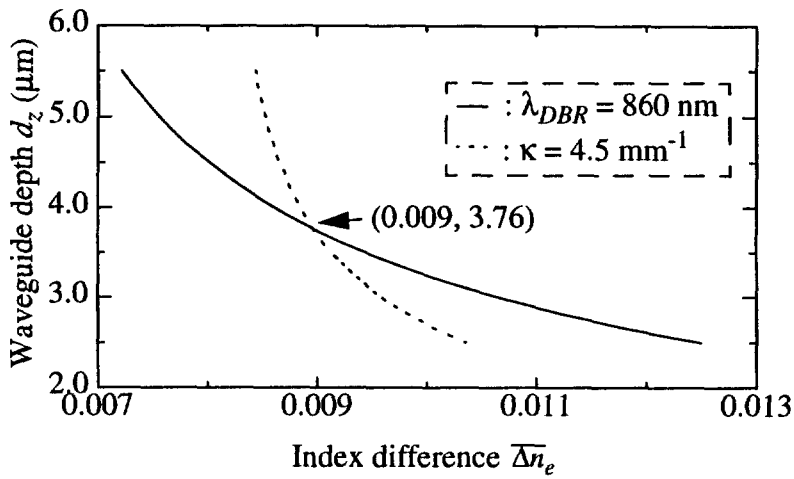

Figure 3.11 Calculated coordinate points of waveguide index difference $\overline{\Delta n_e}$ and depth d_z corresponding to a 3rd order DBR wavelength of 860 nm (solid curve) and a reflectivity performance $\tanh^2(\kappa L)$ with κ = 4.5 mm^{-1} (dashed curve) in a periodically segmented (PS) waveguide with w = 4 μm, Λ = 0.7 μm, D = 0.4/0.7 on flux grown (FG) KTP [57].

3.4 Summary and conclusions

A thorough and detailed characterization of APE uniform waveguides in z-cut $LiTaO_3$ has been performed. Analytical expressions for the mode indices and mode field profile have been directly related to PE and RTA conditions, in which the relationship between the index increase and the proton concentration (3.13) will be characterized using experimental data obtained in chapter 5.

A simplified method has also been developed to simulate the QPM and DBR properties in a PS channel waveguide with step or graded-index distributions for the practical design of a concurrent DBR and QPM-SHG device. It has been found that the model results fit well to the experimental data reported recently by others for KTP waveguides. A mode index N_{high} in the ion-exchanged sections and an average index N_{low} in the substrate index sections in a PS channel waveguide have been introduced for calculating the DBR reflectivity directly from the PS waveguide parameters. This method also allows to predict the QPM and DBR wavelengths. Additionally, by measuring the QPM wavelength and DBR wavelength (or DBR reflectivity performance), the waveguide parameters can be easily determined.

Chapter 4

STUDY OF DOMAIN-INVERSION FOR QPM STRUCTURES IN $LiTaO_3$

4.1 Introduction

As discussed in chapter 2, QPM waveguides fabricated by APE in $LiTaO_3$ have the potential to realize a compact, low cost, high-efficiency device as shown in Fig. 2.9. The analysis in chapter 2 has shown that for high conversion efficiency, deep domain inversion structures with the lowest-order QPM grating (short period), with straight domain walls, and optimized duty cycles need to be fabricated. In this chapter, the experimental investigations on understanding the domain-formation mechanism and developing new fabrication processes for high-quality QPM structures in $LiTaO_3$ are presented. The fabrication of actual QPM waveguides is presented in chapter 5.

4.2 Review of domain-inversion fabrication in $LiTaO_3$

A broad-area surface layer of domain inversion formed on the -c face of z-cut $LiTaO_3$ by PE in benzoic-acid melts at 200-250°C and subsequent heat treatment at 590°C was first realized by K. Nakamura et al [84] in 1990. Later, H. Åhlfeldt et al [16] reported on a 12-μm-period domain inversion structure with semi-circular cross sections again formed by using benzoic acid as PE source. On the other hand, by using pyrophosphoric

acid as the PE source at 260°C for 20-120 min with subsequent annealing at 510-590°C, the fabrication and characterization of smaller periods, such as the third-order (~11 μm period) and first-order (~4 μm period), have been reported in periodically domain inverted $LiTaO_3$ structures [85, 86].

In order to explain the domain inversion it has been proposed [84] that the Curie temperature (T_c = 610°C) of $LiTaO_3$ is decreased by PE since it lowers the Li content. Because of its high dissociation constant (Ka = 2 x 10^{-2}), which is proportional to proton concentration in the acid, compared to benzoic acid (Ka = 6.2 x 10^{-5}), pyrophosphoric acid as PE source will allow higher proton content, and hence lower Li content [87]. This is the major reason of choosing pyrophosphoric acid as the PE source [87] for forming periodically domain-inverted structures.

RTA, which features a rapid rising rate and short annealing time, has been proposed recently as a technique to suppress the lateral expansion and, at the same time, to increase the depth of the domain inversion in first-order periods [86]. RTA minimizes proton diffusion during anneal, therefore the rapid rising rate of temperature suppresses the diffusion of protons before nucleation of antiparallel domains, thus making it possible to suppress the width expansion of the nuclei of domains; additionally, thermal annealing with a rapid rising rate can maintain higher concentrations of protons during annealing time and thus induce a stronger inside electric field.

By utilizing this RTA process shorter-period (i.e. less than 12 μm) domain-inverted structures with considerable inversion depth might be realized also by using benzoic acid as the PE source. We investigated this question since benzoic acid is considerably cheaper than pyrophosphoric acid, and also, since most metals can be used as the selective mask

for PE in benzoic acid. We also investigated the mechanism of domain inversion in $LiTaO_3$ induced by PE followed by heat treatment and the fabrication processes for superior QPM structures.

4.3 Study of broad-area domain formation

In this section, the study of broad-area domain formation by RTA of PE $LiTaO_3$ is presented. Domain inversion phenomena and mechanisms are reviewed and discussed with particular focus on the domain formation by the RTA of PE $LiTaO_3$. Experimental studies are performed to better understand the domain-inversion process and mechanisms in the APE process.

4.3.1 Domain-formation phenomena and mechanisms

As discussed in chapter 3, the key process for realizing APE QPM waveguides is to fabricate a periodically domain-inverted structure with periods of several micrometers. Much research work has been performed to fabricate QPM structures and understand the domain-inversion mechanisms.

It has been reported that lithium oxide (Li_2O) out-diffusion [88, 89] or titanium (Ti) in-diffusion [90] near the Curie temperature (T_c) can induce domain inversion at the +c face of z-cut single-domain $LiNbO_3$ (T_c = 1140°C). Heat treatment at slightly below T_c causes domain inversion on the +c face also in *proton-exchanged* $LiNbO_3$ but on the -c face of *proton-exchanged* $LiTaO_3$ which has a substantially lower T_c (610°C) than $LiNbO_3$ [91]. Additionally, no domain inversion has been observed in non-exchanged

$LiTaO_3$ after heat treatment or Ti in-diffusion at below T_c [91]. It is believed that in $LiTaO_3$ temperatures below $T_c = 610^{\circ}C$ are not sufficient to achieve the proper Li_2O out-diffusion process or enough Ti in-diffusion to nucleate domain inversion. In fact, in $LiTaO_3$, single-domain surface layers have been formed on c faces following heat treatment sufficiently above T_c and it has been found that the polarization of these layers is the same as that of the domain-inverted layers in below-T_c heat-treated $LiNbO_3$ [92], i.e. oriented inward.

Domain inversion in Ti-diffused $LiNbO_3$ [90] can be attributed to an induced electric field by the impurity concentration gradient in the diffused layer [93]. For the Li_2O out-diffusion case, a microscopic model for the domain reversal mechanism has been proposed suggesting a built-in internal electric field induced by a nonuniform distribution of charged donor centers formed during the out-diffusion process at temperatures near $1100^{\circ}C$ [94, 95]. As donor centers both oxygen vacancies [94] and antisite defects (Nb_{Li}) [95] were considered. The physical mechanisms behind the domain formation in $LiTaO_3$ during annealing at temperatures *far above* T_c are believed to be closely related to these models [92]: It appears that at high temperatures (~$1100^{\circ}C$) Li_2O out-diffusion in both $LiNbO_3$ and $LiTaO_3$ will cause a built-in electric field directed inward to form domain reversal on the +c face of z-cut single-domain $LiNbO_3$, and single-domain layers with corresponding polarization (i.e. directed inward) on the two c surfaces of z-cut $LiTaO_3$ with the bulk becoming (or remaining) multidomain.

To explain domain reversal on the -c face of *proton-exchanged* z-cut single-

domain $LiTaO_3$, an inside-field model has also been proposed [96]. According to this model, proton (H^+) diffusion from the proton-exchanged region to the substrate and lithium-ion (Li^+) diffusion in the opposite direction take place during thermal annealing at the lower temperatures near 600°C, whereby H^+ diffuses faster than Li^+. As a consequence an internal electric field is built up between the positive space charge of the diffused H^+ and the negative space charge of the Li^+ vacancies formed after H^+ diffusion. This field, directed outward from the substrate, accounts for the observed nucleation of inverted domains on the -c face.

Recently, it has been shown that proton exchange followed by heat treatment at slightly below or above T_c can be used to form single-domain layers in multidomain $LiTaO_3$ [97, 98] and $LiNbO_3$ [99]. The formed single-domain layers in $LiTaO_3$ [97, 98] have polarizations directed outward from the substrate, which is consistent with the H^+/ Li^+ diffusion model. The observed polarizations in the formed single-domain layers in $LiNbO_3$ [99], however, are directed inward to the substrate consistent with the domain inversion found on the +c face in non-exchanged $LiNbO_3$ heat-treated near T_c as referred to above [88, 89]. This suggests that Li_2O out-diffusion (apparently enhanced by proton exchange) might be the dominant process for domain formation also here, even though another explanation has been proposed [99]. Thus, so far, the details of the physical processes leading to domain inversion or formation of single-domain layers in multidomain crystals are still relatively unclear.

4.3.2 Experimental studies

Our own experimental studies on domain formation in z-cut $LiTaO_3$ by proton exchange followed by RTA showed some more interesting phenomena. Experiments were performed at high temperatures (800-1030°C) where not only H^+ diffusion but also Li_2O out-diffusion can play a role in the process of domain formation. Since H^+ diffusion at such high temperatures could be extremely fast, RTA is crucial in order to allow studying the domain formation development from the very beginning (within seconds) of the annealing process. Indeed, we found that a double-layer of single domains may form on both c faces when the RTA duration was short. We investigated the domain formation development in the extended RTA time range of 2 s to 10 min and conclude that both the H^+ in-diffusion and Li_2O out-diffusion processes are relevant within this annealing range.

Z-cut single crystal $LiTaO_3$ was first annealed at 695°C for 5 min to provide multi-domain samples, the size of the domains being on the order of 1 μm as revealed on a z-face by selective etching in a solution of $HF:HNO_3$ = 1:2. The multidomain samples were then proton exchanged in benzoic acid at 245°C for 2 h and subsequently annealed in air in a RTA furnace (Model: ADDAX R1000-4) at temperatures between 800 and 1030°C. The temperature rise time was 7-9 s whereas the cooling rate started as 140°C/s and slowing down exponentially. The average cooling rate to T_c (610°C) was about 85°C/s. The temperature rising and cooling times are not included in the RTA annealing times quoted below.

Fig. 4.1 is a photograph of a $HF:HNO_3$ etched y face of a proton-exchanged sam-

ple, initially multidomain, that has been annealed at 900°C for 10 s. Two single-domain layers were formed symmetrically at both c faces (only one is shown). One can see well known spurious, characteristically needle-shaped, domains in both single-domain layers. The boundary between the two single-domain layers is somewhat wavy, a characteristic observed in all samples. In order to determine the polarizations of the single-domain layers the c faces were etched in $HF:HNO_3$ (1:2). Fig. 4.2 is a micrograph of an etched c surface of a sample polished to the boundary region between the two formed single-domain layers. Due to the wavy boundary, both single-domain layers can be revealed on this surface. Regions of -c face were etched, whereas regions of +c face were not. In particular, random scratches in the +c region were almost untouched and scratches in the -c region became washed-out, providing an easy means to distinguish the +c and -c faces. Using this method, it was found that the top single-domain layer has inward-directed polarization,

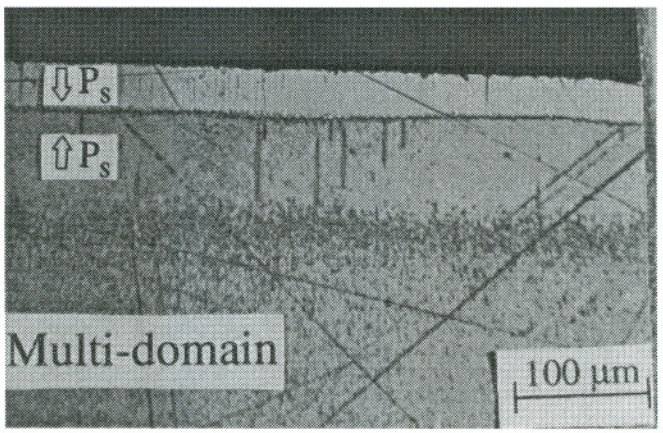

Figure. 4.1 The photograph of the etched y face of an initially multi-domain sample that has been proton exchanged for 2 h at 245°C and then annealed at 900°C for 10 s.

the single-domain layer underneath an outward-directed one.

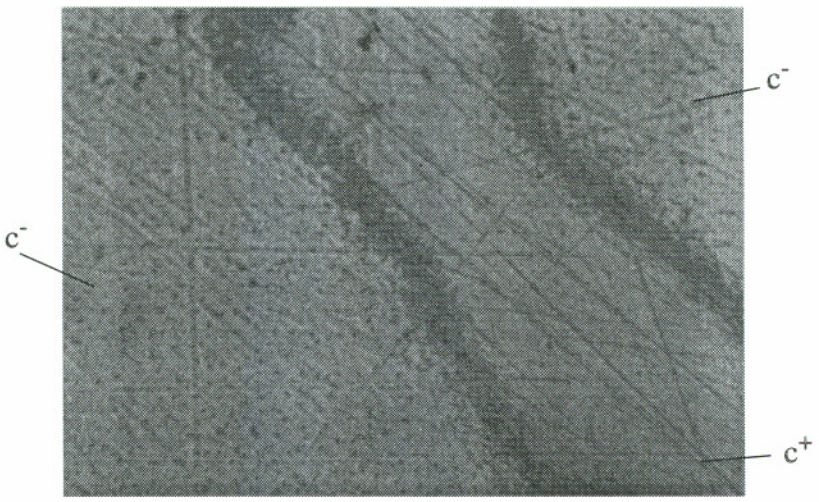

Figure. 4.2 The photograph of the etched c face of polished interface region between the formed single-domain layers of an initially multidomain sample that has been proton exchanged for 2 h at 245°C and then annealed at 900°C for 10 s.

Figure 4.3 schematically shows the domain formation development vs. RTA time at 900°C. With very-short annealing (< 4 s), relatively deep (~80 μm) single-domain layers were formed with polarization directed outwards, reminiscent of what has been observed in Refs [97] and [98] for heat treatment near T_c = 610°C. Somewhat longer annealing (4-60 s) caused the formation of a double-layer of single domains. Long-time annealing (60-300 s) produced multidomains everywhere. The transition from the double-layer to the multidomain formation appeared to be fast and the domain boundaries were barely distinguishable in the process (dashed lines in Fig. 4.3). Of particular interest is that very shallow single-domain layers (~5 μm) were formed again after annealing for a very-long time (> 300 s). The polarizations of these layers were found to be directed inward

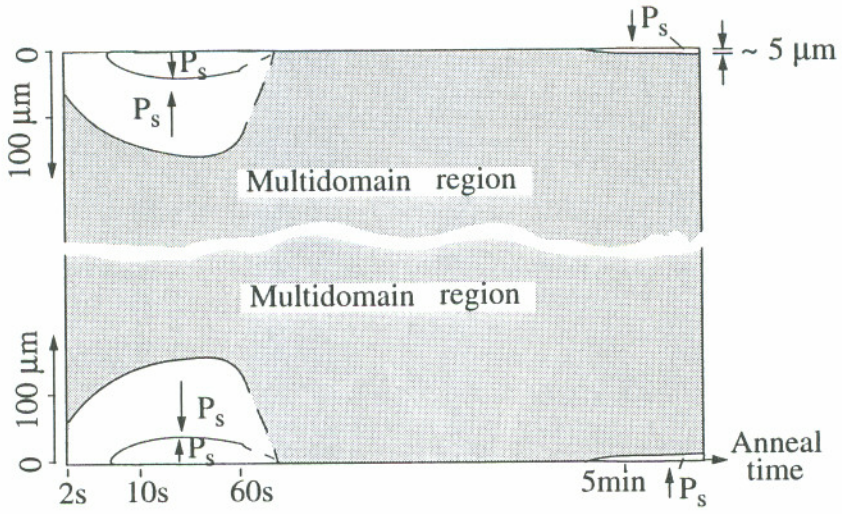

Figure 4.3 Development of the domain structure vs. annealing time. Initially multidomain samples have been proton exchanged for 2 h at 245°C and then annealed at 900°C for different period of time (not to scale).

consistent with the observations for $LiNbO_3$ in Refs. [88], [97], and [99]. Similar behavior vs. RTA time was also observed at 1030°C except that the formed double-layers vanished more quickly.

4.3.3 Discussions

Our observations regarding the formation of a single-domain layer with outward-directed polarization is similar to what has been reported in Ref. [98] for $LiTaO_3$ annealed at 640°C. As in that case it can be explained by the internal electric-field distribution model of H^+/Li^+ diffusion [96], [100]. However, the following significant differences in our observations need to be emphasized: First, the development of the single-domain layers with outward directed polarization proceeds very fast obviously due to the higher

annealing temperature; second, instead of a multi-domain layer as in Ref. [98], another relatively thick single-domain layer (~30-50 μm) of *inward*-directed polarization appeared at both c surfaces for annealing times in the range of 4-60 s; third, this inward-directed single-domain layer disappeared simultaneously with the outward-directed single-domain layer underneath for annealing times 60-300 s. Fourth, shallow outward-directed single-domain layers (~5 μm) at both c faces formed for annealing times > 300 s.

When multidomain samples of $LiTaO_3$ are heated up to 900°C (> T_c), they are in their paraelectric phase as opposed to ferroelectric phase. The domain structure will be determined by the electric-field distribution when the temperature falls below T_c. Based on the H^+/Li^+ diffusion model [96], single-domain layers with outward-directed polarizations are expected. With very short annealing (< 4 s) at 900°C such single-domain layers were formed at both c faces. Since the diffusivity of Li^+ is smaller than that of H^+, with a little longer annealing (4-60 s) H^+ diffuses deep into the substrate and a high concentration of lithium vacancies forms in the surface region, where Ta might be able to jump into some of the lithium-vacant sites forming positively charged Ta_{Li} antisites, similar to the Nb_{Li} antisites formation during Li_2O out-diffusion in $LiNbO_3$ [95]. Thus, an internal electric field directed inwards to the substrate is produced forming the observed inward-directed domain surface layer during cool-down. With further annealing (60-300 s) the H^+/Li^+ diffusion processes will dilute the H^+ concentration, as well as strongly reduce the Li vacancies which reverses the Ta_{Li} antisite formation. Consequently all the charges are more or less neutralized and multidomains form everywhere.

The shallow single-domain layers formed with very-long-time annealing (> 300 s) could then be considered as similar to what has been reported in Ref. [92], where renewed

lithium deficiencies are induced by Li_2O out-diffusion, which is expected to be a much slower process since in that case the diffusion sink is at the surface. That would also explain why the formed single-domain layers are only several micrometers thick in this case. We also found that no such shallow single-domain layers were formed with 300-600 s annealing in pure (non-exchanged) $LiTaO_3$ samples unless the annealing temperature was higher than 1110°C. This is similar to what has been observed in the $LiNbO_3$ case [91, 99, 101] where proton exchange seems to enhance the formation of inward-directed domains. The explanation to this could be that some structural change in the crystal might have occurred due to the prior H^+/ Li^+ diffusion enhancing the Li_2O out-diffusion process. It is very unlikely that a H^+ concentration gradient is the cause for the formation of the shallow single-domain layers formed in $LiTaO_3$ after 5 min annealing as has been proposed in the case of $LiNbO_3$ [99, 101, 102] since H^+ is expected to diffuse into the substrate for several hundred micrometers at such high temperature and for such long-time annealing according to the measured diffusion coefficient in Ref. [71]. Under certain conditions even a double-domain layer formed in $LiNbO_3$ [101] during 1100°C annealing where, according to our judgment, proton-enhanced Li_2O out-diffusion should occur. Interestingly, this double-domain layer has reversed polarizations to the one reported in this thesis and, based on the Li_2O out-diffusion model [95], could possibly be explained by Nb_{Li} depletion from the surface. More remains to be investigated, however, to fully understand the details of all the observed phenomena.

4.4 Fabrication of periodically domain-inverted QPM structures

Based on the domain-formation mechanism discussed in the previous section, periodically domain-inverted structures should be realized using selective PE and afterward RTA at below T_c. Extensive studies on the characteristics of the domain-inversion by RTA of PE $LiTaO_3$ have been reported [86] based on PE source of pyrophosphoric acid, which was thought crucial as mentioned in section 4.2. Here, experimental investigations on fabrication of periodically domain-inverted structures by RTA of benzoic-acid PE $LiTaO_3$ are performed.

4.4.1 Fabrication processes: proton exchange (PE) and rapid thermal annealing (RTA)

The fabrication process for domain inversion was as shown in Fig. 4.4. A 200 nm protective mask of Ti was evaporated by e-beam on the -z face of $LiTaO_3$ and the periodic pattern was defined by CHF_3 etching after the photoresist pattern was defined by photolithography process. Based on the modeling calculation in chapter 3, The first-order grating period for QPM-SHG from 860 nm to 430 nm (blue) is about 3.7 μm. Most of our domain-inversion investigations are carried out on samples with 3.7 μm (1st-order), 7.5 μm (2nd-order), and 11.2 μm (3rd-order) period gratings, for which the Ti-mask duty-cycles are 0.60, 0.80, and 0.50 respectively. PE was carried out at 235°C for 40 min in benzoic acid. The Ti mask was removed by HF etching for several minutes at room temperature after PE. RTA was performed in an air-filled RTA furnace (Model: ADDAX R1000-4) with precise temperature control of ±1°C. The temperature rise time was about 90°C/s, whereas the cooling rate was about 40°C/s slowing down exponentially. The temperature rising and cooling times are not included in the RTA times t_a quoted in this thesis.

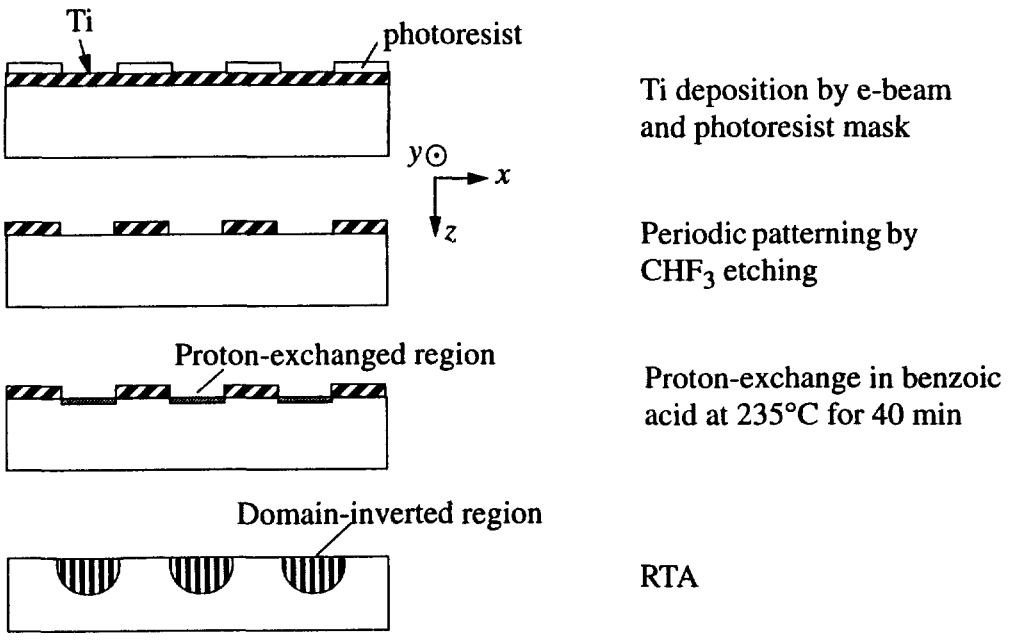

Figure 4.4 Fabrication process for domain inversion in $LiTaO_3$

Using the PE condition described above, investigations on various RTA processes have been performed and will be presented in three categories: (i) Rapid thermal annealing (RTA); (ii) Short-time RTA; (iii) Short-time RTA with pre-annealing.

4.4.2 Rapid thermal annealing (RTA)

To study the domain growth in vertical and lateral directions, we fabricated periodically domain-inverted structures with RTA times from 6 s to 300 s at various temperatures for the third-order grating (Λ = 11.2 μm). After RTA, samples were etched in a mixture of HF/HNO_3 to reveal the inversion structure on a y face. These were mostly semi-circles as has been previously reported [16], [85]. Figure 4.5(a) and 4.5(b) show the inversion depth (maximum depth) and the duty cycle (on the surface) as a function of RTA

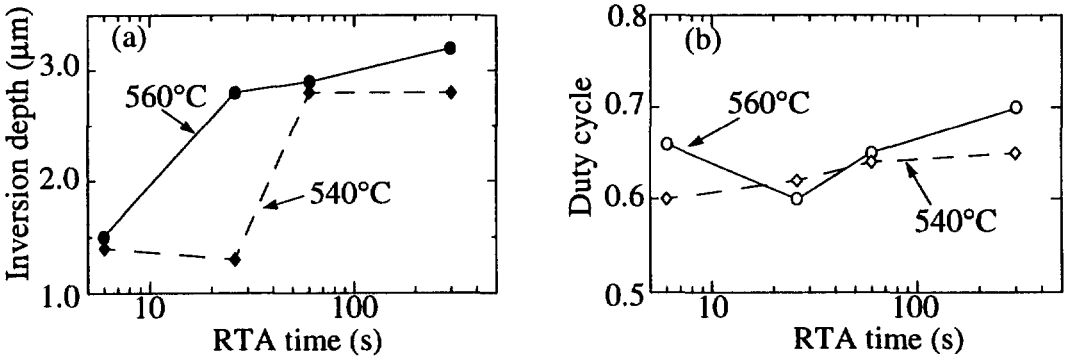

Figure. 4.5 (a) The domain inversion depth and (b) the inversion duty cycle vs. RTA time in the third-order gratings (Λ = 11.2 μm) for 540°C (diamonds) and 560°C (circles) anneal.

time at 540°C and 560°C. The inversion depth increases with longer annealing time and turns to saturate after a short RTA time of about 60 s. The maximum depth is similar to the depth of 2.7 μm observed in a third-order grating with 10 min heat treatment at 590°C after PE in pyrophosphoric acid for about 50 min [85]. The duty cycle varies between 0.6-0.7 with various annealing times at both temperatures, which shows that the lateral expansion (duty cycle from 0.50 to 0.6-0.7) is not strongly dependent on RTA time at 540-560°C in this third-order grating case probably due to a relatively large period. At 520°C (not shown), similar behavior was observed as in the 540°C case.

In the fabrication of the first-order QPM grating (Λ =3.7 μm), the inversion structures are also mostly semi-circles as in the third-order grating cases. Figure 4.6(a) and 4.6(b) show the inversion depth and duty cycle as a function of RTA time at 540°C and 560°C for the first-order gratings. It can be seen that good QPM structures were formed only with 6 s RTA. When the RTA is somewhat longer (12 s) the inversion structure spreads laterally in contrast to what was observed in the third-order grating case (Fig. 4.5).

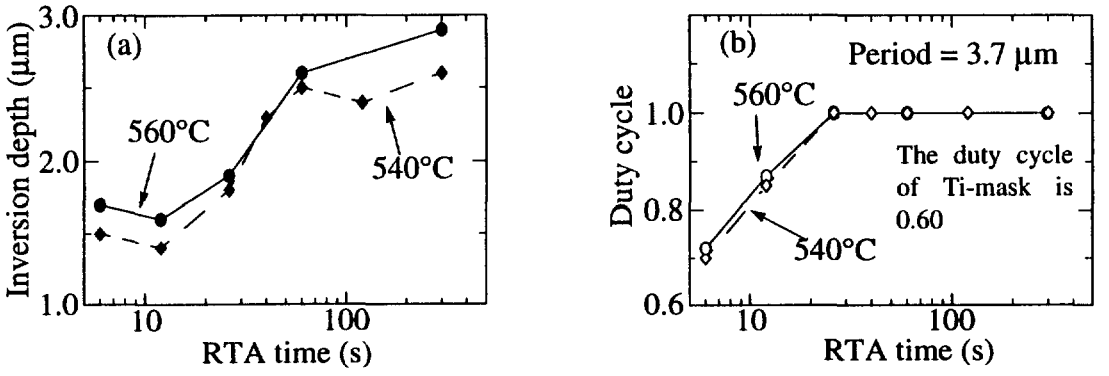

Figure 4.6 (a) The domain inversion depth and (b) the inversion duty cycle vs. RTA time in the first-order gratings (3.7 μm period) for 540°C (diamonds) and 560°C (circles) anneal.

The lateral spreading of the domain is much more sensitive to the increase of RTA time. At and beyond 26 s, the inversion regions overlap on the surface. At higher RTA temperatures (≥ 580°C) all samples with the first-order gratings revealed domain inversion overlapping even for the shortest annealing time (6 s). These experimental results show that RTA at very short time is a key requirement which allows fabricating short-period domain-inverted structures on the -z face of the benzoic-acid-proton-exchanged $LiTaO_3$. But the QPM structures formed are semi-circles and, additionally, it was found that forming deeper domain inversion (> 1.7 μm) with reasonable duty cycle in 3.7 μm-period gratings is a difficult task.

4.4.3 Short-time RTA

To explore forming QPM structures with improved properties, we investigated the domain inversion depth and duty cycles as a function of RTA temperatures with short-time RTA (6 s) and long-time RTA (5 min) respectively. As shown in Figures 4.7(a) and 4.7(b)

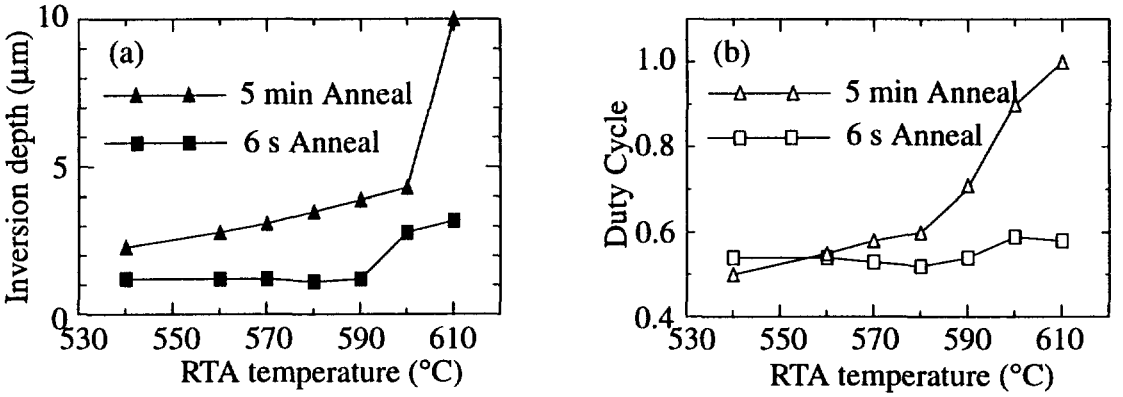

Figure 4.7 (a) The domain inversion depth and (b) the inversion duty cycle vs. RTA time in the third-order gratings (11.2 μm period) for 6 s (squares) and 5 min (triangles) anneal.

for the third-order grating, with short-time RTA (6 s) lateral expansion remains (duty cycle from 0.5 to 0.6) small at all RTA temperatures, and the domain inversion depth increases up to ~3 μm at RTA temperatures above 600°C. Inversion depth is always deeper with long-time RTA as expected, but the lateral expansion will now be substantial leading eventually to domain overlapping particularly at high temperatures. It is noteworthy that at short-time RTA domain inversion depth increases dramatically at temperatures near T_c. This phenomenon can be utilized to realize simultaneous fabrication of domain inversion and waveguide in a single-step process as will be discussed in section 5.2.3 of chapter 5.

Even though at certain RTA temperatures, e.g. 570°C, long-time RTA forms domain-inversion structures with reasonable depths and duty cycles, we found that they are semi-circle domain structures with tilted domain walls consistent with the observation in Refs. [16] and [85]. However, short-time RTA at proper temperatures allows to generate near-straight-domain-wall structures with limited lateral expansion. Figure 4.8(a) and 4.8(b) show the cross-sectional photographs of the second- and third-order near-straight-

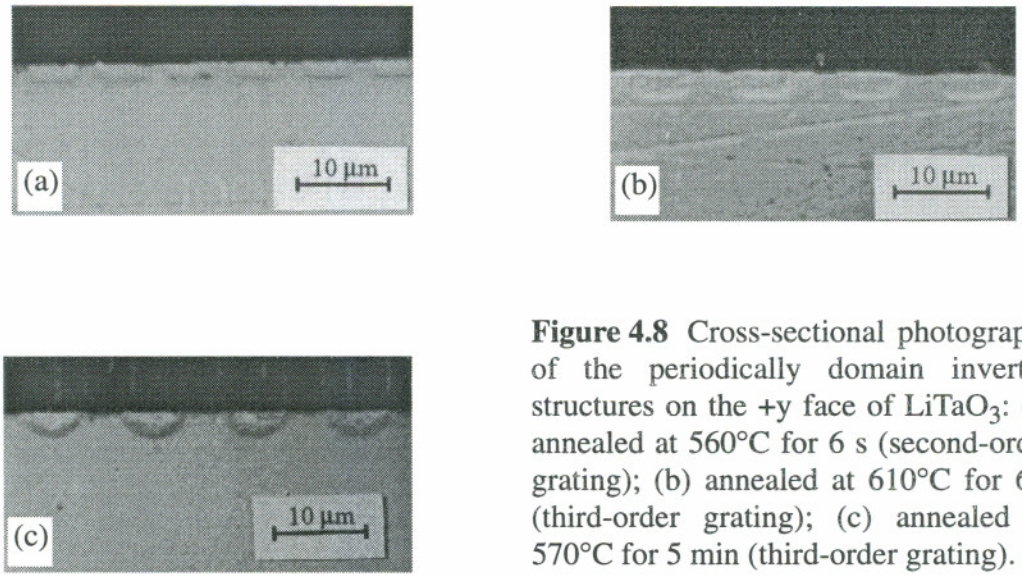

Figure 4.8 Cross-sectional photographs of the periodically domain inverted structures on the +y face of $LiTaO_3$: (a) annealed at 560°C for 6 s (second-order grating); (b) annealed at 610°C for 6 s (third-order grating); (c) annealed at 570°C for 5 min (third-order grating).

domain-wall structures viewed from +y face in $LiTaO_3$. The samples were annealed for 6 s at 560°C and 5s at 610°C respectively, and both etched in a mixture of HF/HNO_3 to reveal the structure. The 2.2 μm depth and near 0.75 duty cycle are both very significant for a second-order QPM-SHG, which will be demonstrated in section 5.3 of chapter 5. For comparison, Fig. 4.8(c) shows the semi-circle domain inversion structures formed by RTA at 570°C for 5 min. For the samples with the short-time RTA, the domain inverted regions are seen to be much closer to the ideal rectangular shapes than the semi-circles of the 5 min RTA. These experimental results indicate that short-time RTA is critical for realizing near-straight-domain-wall structures with less lateral expansion and considerable inversion depth.

4.4.4 Short-time RTA with pre-annealing

Near-straight-domain-wall structures can be realized by using higher temperature and short-time annealing for higher-order gratings shown in Fig. 4.8(a) and 4.8(b). In the fabricated domain-inverted structures of Fig. 4.6 for the first-order gratings (Λ = 3.7 μm), however, even 6 s RTA time appears to be too long for near-straight-wall-domain formation and the deepest inversion depth obtained without overlapping is only 1.7 μm. The reason of this could be due to a relatively wide open window (~2.2 μm) on the Ti-mask (D = 0.6) for the PE process in our samples and thus a narrow distance (1.5 μm) between the PE regions. However, we found that short-time RTA with a pre-annealing process at temperatures lower than 480°C allows fabricating deeper inversion structures with near-straight domain walls and least lateral expansion.

We suppose that pre-annealing at low temperatures drives protons deeper into the substrate, but domain inversion nucleation does not occur. Figure 4.9 shows the comparison of the 3rd-order-grating inversion structures between short-time RTA at 600°C with and without pre-annealing. Two different pre-annealing processes have been used: one is followed by the high-temperature anneal directly (Fig. 4.9(b)), and the other one by a cool down before the high-temperature anneal (Fig. 4.9(c)). For the third-order gratings, the RTA times of 6 s and 12 s at 600°C will usually generate similar inversion structures, so these two pre-annealing processes should have essentially the same impact on the domain formation. The lateral expansion in the three samples can be seen to be almost identical (with D = 0.53, 0.55, and 0.54 respectively in Fig. 4.9(a), (b), and (c)) but, with pre-annealing, the inversion depth increases by about 0.7 μm.

This pre-annealing technique is more essential for fabricating high-quality domain inversion structures with shorter periods. As shown in Fig. 4.10, with pre-annealing at

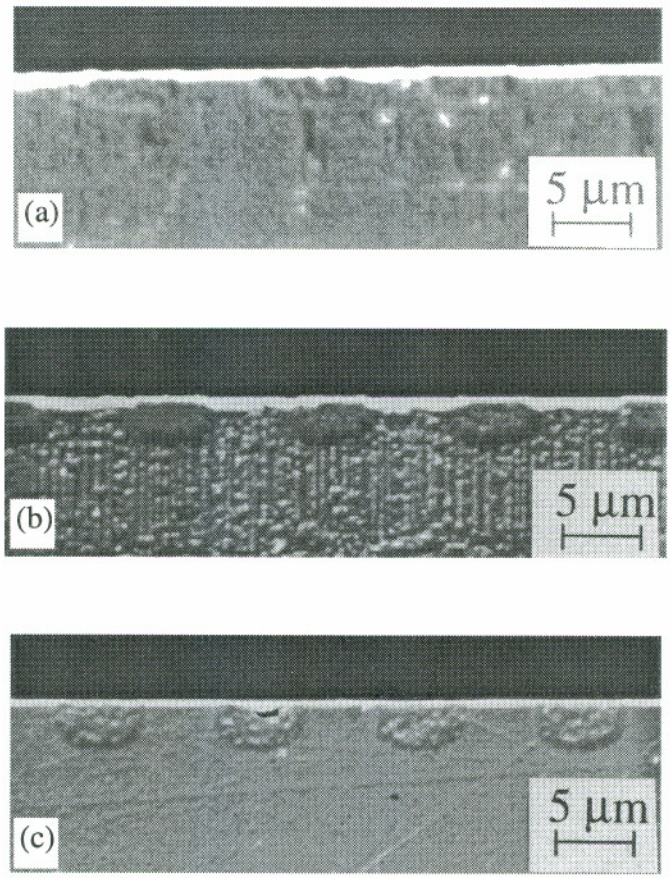

Figure 4.9 Cross-sectional SEM micrographs of the third-order periodically domain-inverted structures on the y face of $LiTaO_3$; anneal process: (a) 6 s at 600°C; (b) 60 s at 480°C, then immediately 6s at 600°C; (c) 60 s at 480°C, cool down to room temperature, then 12s at 600°C.

425°C for 30 s, a very good first-order QPM structure (~2.2 μm depth, ~0.6 duty cycle with a period of 3.7 μm) can be formed even at RTA temperatures as high as 600°C, where the domain lateral spread seems to become negligible with a duty cycle of 0.6 in the Ti-mask.

To study and understand the characteristic of this pre-annealing process, the dependence of the domain inversion depth on the pre-annealing times was examined in broad-area proton-exchanged $LiTaO_3$ samples. Figure 4.11 shows the inversion depth as a

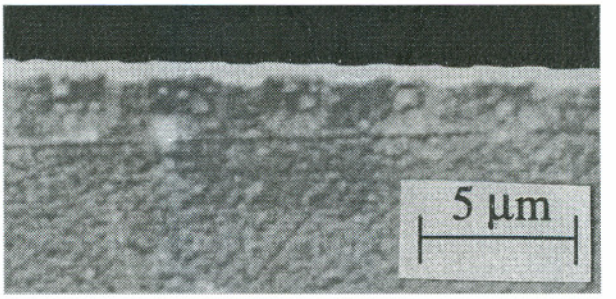

Figure 4.10 Cross-sectional SEM micrograph of the first-order periodically domain-inverted structures on the +y face of $LiTaO_3$; anneal process: 30 s at 425°C, then immediately 5 s at 600°C.

function of pre-annealing times at 425°C with RTA at 600°C for 6 s. Even though the inversion depth is a function of the inversion widths [86], the tendency of the domain-inversion behavior can be observed in Fig. 4.11, which indicates that deeper domain inversion occurs up to a certain time of pre-annealing. However, long pre-annealing drives protons too deep into the substrate so that domain inversion can only be formed near the

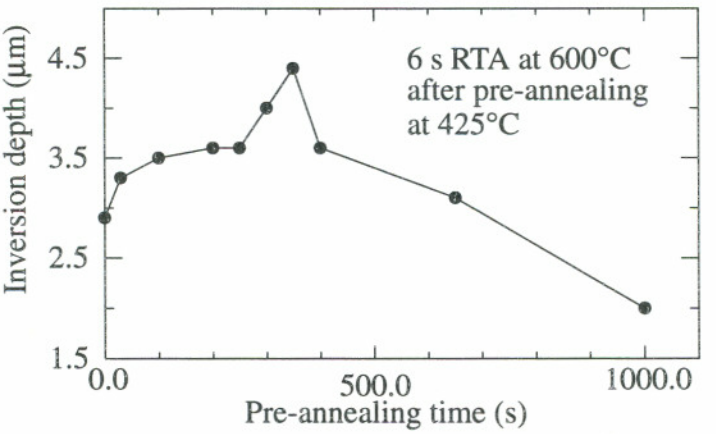

Figure 4.11 Domain inversion depth in broad area samples as a function of pre-annealing times. Short-time RTA was performed at 600°C for 6 s followed by pre-annealing at 425°C.

surface during the subsequent RTA step.

4.4.5 Discussions on domain-inversion fabrication

The domain inversion behavior we observed is in general similar to what was reported by K. Yamamoto et al. for their fabrication process [86], in which PE was performed at 260°C for 20 min in pyrophosphoric acid, and thus can be also understood by the inside-field model proposed by them [96] which we had discussed in section 4.3.1. Intuitively, the width of the initial proton-exchanged region and of the subsequently diffused-in H^+ composition profile, as determined by the width of Ti-mask and the PE conditions, will all affect the domain inversion during RTA. In our experiments, we found that PE at the lower temperature (235°C) in benzoic acid does not seem to have obvious drawbacks in order to form short-period domain-inverted structures in $LiTaO_3$. We have demonstrated that proper RTA time and temperature does allow for the formation of good domain inversion structures even with a relatively lower amount of exchanged H^+ in $LiTaO_3$.

In our RTA experiments, we found that short-time RTA usually generates near-straight-domain-wall structures with limited lateral expansion and longer time annealing usually generates semi-circle domain structures with more lateral expansion and tilted domain walls. We believe this behavior is closely related to the proton diffusion at RTA temperatures. In broad-area PE samples, we found that the domain inversion depth tends to saturate after short-time annealing, which indicates that a short-time RTA at proper temperatures is able to form deep enough inversion. Also, since H^+ diffusion is faster in the z direction than that in the x direction of $LiTaO_3$ [71], H^+ diffusion in z direction would

induce the stronger inside electric field necessary for domain inversion. Thus, it seems likely that the domain nucleation tends to start vertically from the original PE region and further annealing would result in lateral spreading of domain nucleation due to the advancing lateral diffusion of H^+. To avoid this lateral domain expansion, a short-time RTA at proper temperatures becomes crucial, which is evident from Fig. 4.7.

When considering the fabrication of first-order QPM gratings (period < 4 μm) for blue-light generation, the suppression of lateral domain growth without sacrificing vertical domain growth becomes more critical. For this purpose we developed the process of short-time RTA with pre-annealing. Fig. 4.12 depicts the conjectured situation created by RTA with and without pre-annealing. Domain inversion can be formed in the regions having higher inside field in the -c direction and higher H^+ content, e.g. lower Curie temperature. Pre-annealing here allows protons to diffuse both vertically and laterally into the substrate without domain nucleation occurring, so that the interface between the proton-diffused region and the substrate extends deeper and wider into the substrate during the RTA process. This may lead to a lateral overlap of the H^+ regions. Referring to Fig. 4.12(a), the H^+-diffusion-induced inside field would be small and the H^+ content would be low in the overlapping regions of the H^+-diffusion, where domain inversion will not be formed when proper short-time RTA is carried out. On the other hand, the RTA will induce relatively deep domain inversion in the central regions. In RTA without pre-annealing the interface between the proton-diffused region and the substrate will start to expand into the substrate from the PE region at high temperature and nucleate the domains simultaneously. Without pre-annealing this interface is closer to the surface as shown in Fig. 4.12(b). This would induce a stronger inside field in the lateral regions. In order to

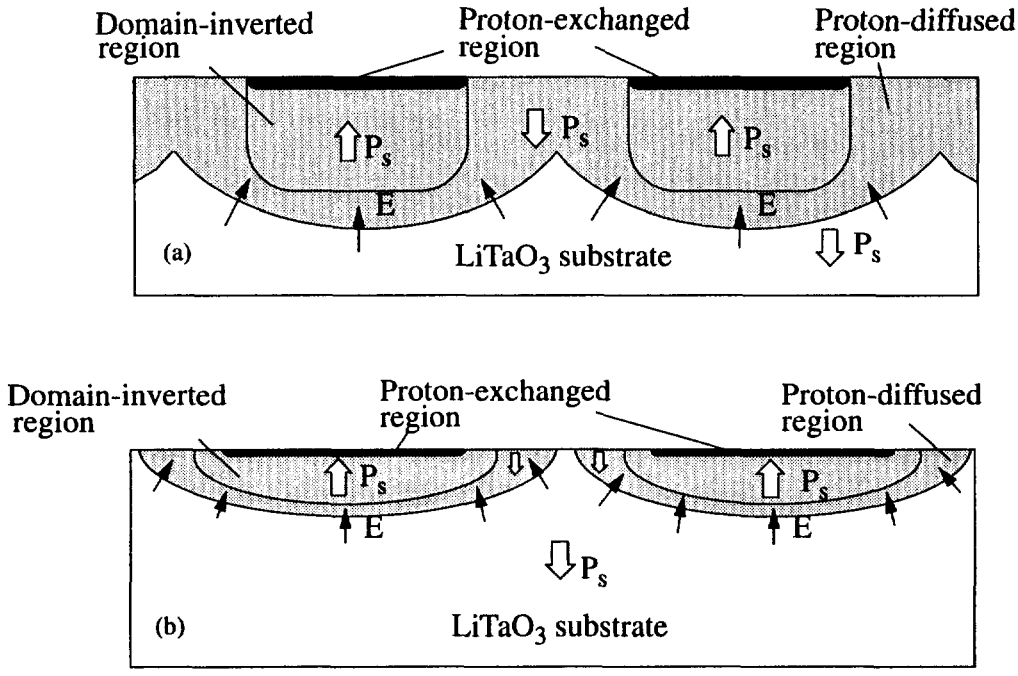

Figure 4.12 Schematic representation of domain-inversion formation in z-cut $LiTaO_3$ by short-time RTA: (a) with pre-annealing; (b) without pre-annealing.

form deeper domain inversion, relatively longer RTA is necessary, which then would induce more lateral domain expansion or even domain overlapping especially when the PE windows are relatively wide in very-short-period structure, as in our first-order structure.

4.5 Summary and conclusions

In our broad-area domain-inversion study, we have shown that a double-layer of single domains with opposing polarizations may form on both c faces by RTA of proton-exchanged z-cut $LiTaO_3$ at above T_c. Depending on the RTA temperature and time either one single-domain layer is formed on each of the two c-faces (very short anneal), or a dou-

ble-layer of two single domains with opposite polarization appears on each c face (somewhat longer anneal). Homogeneous multidomains are formed when annealing time is extended further. Very long anneal time generates shallow single-domain layers again. The results indicate that an internal electric field with inward direction close to the c face and outward direction somewhat deeper inside the substrate has formed at the early stage of RTA of proton-exchanged multidomain $LiTaO_3$.

Based on this understanding of domain formation, we have demonstrated periodic domain inversion in $LiTaO_3$ with short periods by using benzoic rather than pyrophosphoric acid for PE followed by RTA at temperatures around 520-610°C. This allows the fabrication of first-, second-, and third-order gratings for blue-light QPM-SHG. PE at the lower temperature (235°C) in benzoic acid does not seem to have obvious drawbacks in order to form short-period domain-inverted structures. It has been found that short-time RTA (~6-12 s) is critical for reducing lateral domain growth and achieving near-straight domain walls. Short-time RTA with pre-annealing at lower temperatures (< 480°C) has been developed to reduce lateral domain spreading for deep QPM structures, especially in case of short-period structures. A possible mechanism of this process has been discussed based on the inside-field model. Domain-inverted structures with near-straight domain walls and inversion depths as deep as 2.2 μm for the first-order gratings, 2.2 μm for the second-order gratings, and 3.3 μm for the third-order gratings have been realized by proton exchange in benzoic acid followed by RTA with or without a pre-annealing process.

Using the developed fabrication processes for QPM structures, waveguide fabrication is going to be investigated in the next chapter to realize QPM waveguide devices.

Chapter 5

FABRICATION OF QPM WAVEGUIDES IN $LiTaO_3$ AT HIGH TEMPERATURES

5.1 Introduction

The potential for use of APE QPM waveguides in $LiTaO_3$ to build the compact device configuration as shown in Fig. 2.9 will not be possible unless the PS waveguides with short-period and strongly confined modes can be fabricated. In the previous chapter, the fabrication processes for high-quality short-period QPM structures have been discussed, where the non-linear optical coefficient is periodically modulated. In addition to that, realization of well-guided APE waveguides with DBR structures (refractive index is also periodically modulated) is also needed for such a device configuration. In this chapter, we present our investigations on the single-step fabrication of PS QPM waveguides at high temperatures (540-610°C) using the same PE conditions and similar RTA conditions as for domain-inversion fabrication aiming at developing a process to realize DBR structures in APE QPM waveguides. We also present the determination of relationship between the index increase and the proton concentration in the PE $LiTaO_3$ layer.

5.2 Waveguide fabrication and characterization

Prior to this thesis work, the fabrication of APE waveguides in $LiTaO_3$ at high temperatures from 470-610°C was first studied by H.Åhlfeldt et al [16]. Simultaneous fabrication of domain inversion structures (semi-circles, depth = 3 μm, period = 12 μm) and APE planar waveguides (1/*e* mode size = 4 μm) was realized with PE at 220°C for 40 h and subsequent annealing at 470°C for 10 min, in which length-normalized conversion efficiency, measured as $0.4\%W^{-1}cm^{-2}$, is low due to non-rectangular QPM structures and low mode confinement [16]. Both Ref. [16] and another work [68], performed in parallel with this thesis work, suggested that two photolithography processes are necessary to fabricate strongly confining APE QPM waveguides in $LiTaO_3$. In the first step PE through a periodic mask followed by a high temperature anneal (470-610°C) is required for fabrication of the domain-inverted structure. In the second step PE through a waveguide mask followed by a low temperature anneal (360-430°C) is required for fabrication of a uniform channel waveguide.

As discussed in the previous chapter, even though domain inversion in the APE process is closely related to proton diffusion, periodically domain-inverted structures were only formed at temperatures near T_c, where protons diffuse so fast that it is not easy to achieve proper mode confinement to the relatively shallow domain inversion depth. Our investigations on fabrication of high-quality periodically domain-inverted QPM structures have shown that when the RTA temperature is very high, high-quality QPM structures may be formed with very-short annealing time. As has been shown in Fig 4.7(a), domain inversion depths take off when the RTA temperature gets closer to T_c in the 6-s-anneal case. If the annealing time necessary to form the periodically domain-inverted gratings is short

enough so that the proton diffusion depth is comparable to the inversion depth, strongly confined QPM waveguides would be achievable using only a single-step photolithography process, which is a prerequisite for a strongly confined waveguide with DBR structures.

The investigation starts with fabrication and characterization of uniform planar waveguides at 540 and 560°C to understand the waveguiding and domain-inversion behavior at such high temperatures and compare the results with APE waveguide modeling discussed in section 3.2. Based on this the fabrication of PS QPM planar waveguides (2nd-order QPM at 860 nm, period = 7.5 μm, duty cycle of Ti mask = 0.8; 1st-order QPM at 980 nm, period = 5.6 μm, duty cycle of Ti mask = 0.3, 0.4, 0.5) will be presented.

5.2.1 Fabrication process and experimental set-up for mode testing

The PE and RTA processes for the waveguide fabrication is the same as for domain-inversion process as discussed in section 4.4.1. Fig. 5.1 shows the experimental set-up to measure the near field of the guided mode in the fabricated waveguides. The 860 nm high-power (~100 mW) diode laser (SDL-5410C) was used as the source, which was temperature stabilized by a thermoelectric cooler (TEC) controlled according to the feedback from the detected temperature by the resistance temperature device (RTD). The output of the laser diode was collimated using a diode laser objective lens (N.A. of 0.55), transferred from TE polarization to TM polarization by a half-wave plate, and focused into the APE waveguide using another diode laser objective lens (N.A. of 0.47). The near field of the guided mode was imaged on to a CCD detector and its output signal was viewed on a standard 12 inch monitor, where the near field was enlarged and measured. Part of the output light from the waveguide was reflected by the beam splitter into a multimode fiber whose

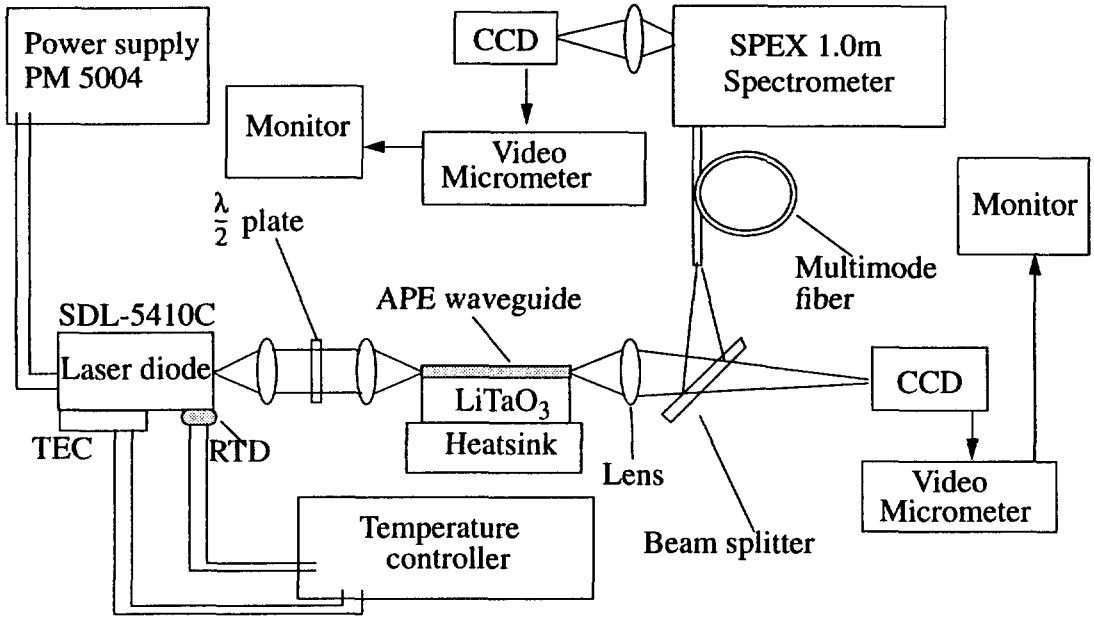

Figure 5.1 Waveguide-test experimental set-up

output was imaged on to the entrance slit of a SPEX 1m grating spectrometer (Model 1704) so that the spectrum could be monitored.

5.2.2 Uniform planar waveguides

Figure 5.2 shows the measured $1/e^2$ mode size (TM_0 mode) and the domain-inversion depth vs. RTA time in uniform (as opposed to PS) planar waveguides fabricated at 540°C and 560°C. The circles are the measured domain-inversion depths obtained using the etching method mentioned in section 4.3.2, and the diamonds are the measured mode sizes. The solid lines are the extrapolated proton-diffusion depths d_z calculated from eq. (3.8) and (3.10). It can be seen that in both Fig. 5.2(a) and 5.2(b) the domain-inverted layer is always less deep than the proton-diffusion depth, which is consistent with the inside-filed model [96] described in section 4.3.1 and also schematically shown in Fig.

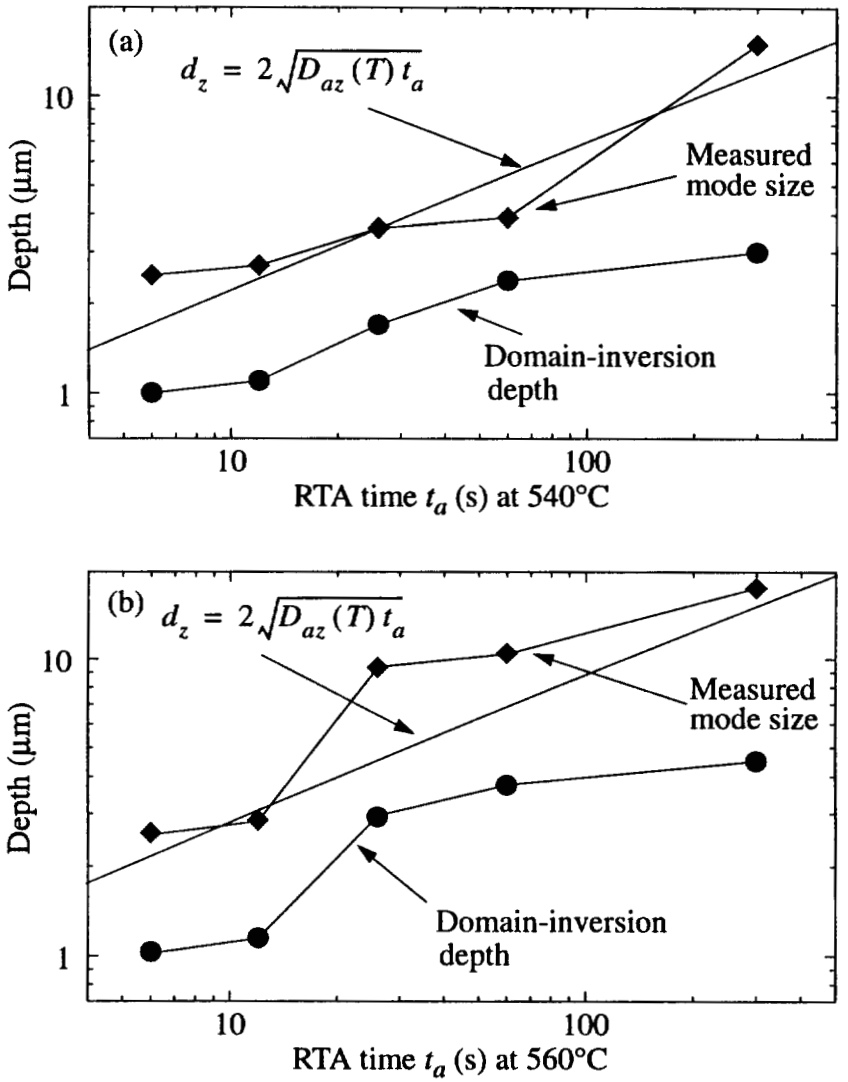

Figure 5.2 Dependence of $1/e^2$ mode size (diamonds) and domain-inversion depth (circles) on RTA times in uniform planar waveguides with (a) 540°C RTA; (b) 560°C RTA.

4.12. It is reasonable to find that the mode sizes are comparable to the proton-diffusion depths d_z. Notice that very short-time (<12 s) RTA at such high temperatures suffices to form strongly confining waveguides in $LiTaO_3$ ($1/e^2$ mode size $\leq$ 3.0 μm). For the waveguides fabricated with $t_a > 26$ s at 540°C or $t_a > 12$ s at 560°C, the guided modes are relatively weak and the mode distribution tails into the substrate, which shows that most

protons diffuse too deep into the substrate; hence, waveguiding is weakened with less protons, i.e. less index increase, in the surface region.

As mentioned in section 3.2.1, the γ constant in equation (3.13) needs to be determined to predict the waveguiding characteristics for APE waveguides in $LiTaO_3$ with given fabrication conditions. Here we present an empirical approach to relate the index increase $\Delta n_e(\lambda)$ to the annealing conditions. With fixed PE condition: 40 min at 235°C in benzoic acid, the exchange depth d_e has been calculated as 0.42 μm using eqs. (3.2) and (3.3). C_{ex}^H is fixed and independent of anneal conditions as discussed in section 3.2. For uniform planar waveguides, equation (3.12) is reduced to

$$C_{ex}^H \cdot d_e = C_0^H \int_0^\infty f(z)\, dz \tag{5.1}$$

where $f(z)$ is expressed by eq. (3.6) with d_z dependent on the anneal conditions. Using the assumption that the index increase in APE $LiTaO_3$ is proportional to the proton concentration and using equations (3.13) and (5.1), the index increase at the surface $\Delta n_e(\lambda)$ in APE $LiTaO_3$ can be written as

$$\Delta n_e(\lambda) = \gamma C_0^H = \frac{\gamma C_{ex}^H \cdot d_e}{\int_0^\infty f(z)\, dz} \tag{5.2}$$

With certain anneal conditions, $\int_0^\infty f(z)\, dz$ can be calculated by using eqs. (3.8) and (3.6),

and the surface index increase $\Delta n_e(\lambda)$ can be uniquely determined by searching for the $\Delta n_e(\lambda)$ value so that the calculated $1/e^2$ mode sizes match the measured sizes. Table 5.1 gives thus the relationship between $\Delta n_e(\lambda)$ and $1/\int_0^\infty f(z)\,dz$ at various anneal conditions. The anneal-condition data points are chosen based on two criteria. First, since our interest

Table 5.1 $\Delta n_e(\lambda)$ determined from best fit of calculated mode sizes to measured ones

Anneal condition	d_z	$1/\int_0^\infty f(z)\,dz$	Measured $1/e^2$ mode size	$\Delta n_e(\lambda)$ with the same mode sizes
6 s at 560°C	2.2 μm	0.500	2.6 μm	0.0163
12 s at 540°C	2.4 μm	0.448	2.7 μm	0.0155
12 s at 560°C	3.1 μm	0.356	2.9 μm	0.0151
26 s at 540°C	3.6 μm	0.306	3.4 μm	0.0106

is on the fabrication of the strongly confining waveguides, data with big mode sizes are insignificant. Secondly, our model discussed in section 3.2 is more accurate for well-annealed waveguides, data points with anneal conditions causing $d_z >> d_e$ are used. We found that the deduced $\Delta n_e(\lambda)$ values are consistent with the reported values in Refs. [73, 74]. The results for $\Delta n_e(\lambda)$ and $1/\int_0^\infty f(z)\,dz$ in Table 5.1 are used to generate Fig. 5.3, in which the best-fit straight line of the calculated data points has given

$$\Delta n_e(\lambda) = \frac{0.035}{\int_0^\infty f(z)\,dz} \tag{5.3}$$

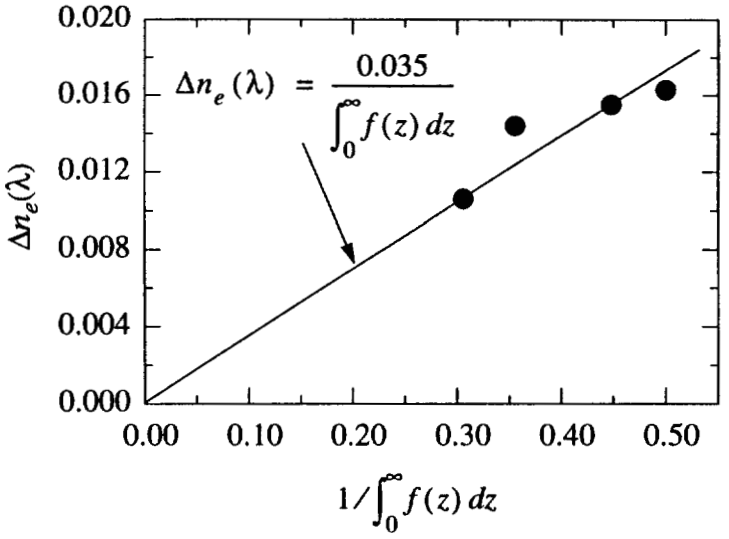

Figure 5.3 Surface index change vs. anneal conditions

Comparing eq. (5.3) with (5.2), it can be seen that

$$\gamma C_{ex}^{H} \cdot d_e = 0.035 \tag{5.4}$$

So, for an APE channel waveguide in $LiTaO_3$, using eqs. (3.12) and (5.4), the 2-D index profile shown in eq. (3.13) can be related to the RTA conditions as

$$\Delta n_e(\lambda, z, y) = \frac{0.035 w f(z)\, g(y)}{\int_{-\infty}^{\infty} g(y)\,dy \int_0^\infty f(z)\,dz} \tag{5.6}$$

where $f(z)$ and $g(y)$ are related to the RTA conditions as shown in section 3.2.1. Further-

more, considering the exchange factor $x = x_{PE}$ after PE and $x = x_{APE}$ on the surface after annealing for the $H_xLi_{1-x}TaO_3$ system, equation (5.1) gives

$$x_{PE} \cdot d_e = x_{APE} \int_0^\infty f(z)\, dz \tag{5.7}$$

By using measured data from Ref. [71] resulting in $x_{PE} = 0.80$, $d_e = 0.42$ μm as determined for our PE conditions, and combining eqs. (5.3) and (5.7), the relationship between index increase and the proton exchange factor x_{APE} can be deduced as

$$\Delta n_e(\lambda) = 0.10 x_{APE} \tag{5.8}$$

Notice that relation (5.8) is only applicable to the α-phase $H_xLi_{1-x}TaO_3$ system.

5.2.3 Simultaneous QPM structure and PS waveguides

According to the findings discussed in the previous section, fabrication of strongly confining PS QPM waveguides with a single-step process at high temperatures becomes possible. Table 5.2 summarizes the fabricated QPM waveguides with short-time RTA at high temperatures. Sample 1 has period $\Lambda = 7.5$ μm designed for 2nd-order QPM at around 860 nm with Ti-mask duty cycle $D = 0.80$. RTA for 6 s at 560°C was carried out on sample 1. Measured mode sizes are $1/e^2$ sizes for sample 1. Samples 2, 3, 4, and 5 have period $\Lambda = 5.6$ μm with Ti-mask duty cycle $D = 0.3$ or 0.4. $1/e$ mode sizes are measured

for sample 2, 3, 4, and 5. They were designed for 1st-order QPM at 980 nm but waveguiding was tested at λ = 860 nm. Given the RTA anneal conditions, the proton-diffusion depth d_z were calculated using eq. (3.8), and TM_0 mode sizes ($1/e^2$ for sample 1 and $1/e$ for sample 2, 3, 4, and 5) were calculated using the model described in section 3.2 and equation (3.24). Domain inversion depths, duty cycles, and the measured mode sizes are also listed in Table 5.2.

Table 5.2 Fabricated PS QPM planar waveguides at high temperatures in a single-step process (characterized at λ = 860 nm)

Sample number	Λ μm	D	RTA anneal	d_z μm	Inversion depth (μm)	Domain duty cycle	Measured mode size (μm)	Calculated mode size (μm)
1	7.5	0.8	6 s at 560°C	2.2	2.2	0.75	2.6 ($1/e^2$)	2.7 ($1/e^2$)
2	5.6	0.3	4 s at 607°C	2.9	2.6	0.45	3.2 ($1/e$)	3.6 ($1/e$)
3	5.6	0.4	4 s at 607°C	2.9	2.8	0.52	3.1 ($1/e$)	3.1 ($1/e$)
4	5.6	0.3	4 s at 610°C	3.0	2.8	0.52	3.4 ($1/e$)	3.6 ($1/e$)
5	5.6	0.4	4 s at 610°C	3.0	3.0	0.58	3.4 ($1/e$)	3.1 ($1/e$)

The fitting parameters M and χ, which has been used to calculate the mode sizes in Table 5.2 are listed in Table 5.3. Fig. 5.4 shows the comparison of the domain inversion depths, mode sizes (all 1/e mode sizes except for sample 1), the calculated proton-diffusion depths. It is noteworthy that even 10 s RTA at 600°C is already too long to retain the strong confining feature of the waveguides. Thus, from Table 5.2 and Fig. 3.5, it can be

Table 5.3 Fitting parameters determined to calculate the mode sizes listed in Table 5.2

Sample number	1	2	3	4	5
M	1.086	1.086	1.086	1.086	1.086
χ	0.9848	0.9909	0.9909	0.9909	0.9909

seen that short-time RTA is crucial for forming simultaneous QPM structures and strongly confining waveguides and the measured mode sizes are close to the calculated ones and comparable to the domain-inversion depths

Notice that the domain-inversion depth of the PS planar waveguide sample 1 in Table 5.2 is about two times bigger than that of the uniform planar waveguide in Fig. 5.2(b) and the domain duty cycle is obtained as 0.75 from Ti-mask D = 0.8, and further anneal (t_a > 6 s) on this sample induced domain overlap. This result indicates that the

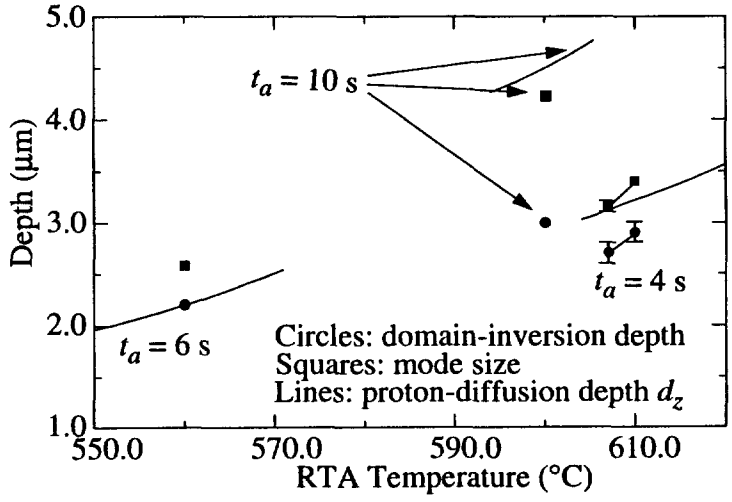

Figure 5.4 PS planar waveguides with comparable mode size and domain-inversion depth fabricated by various RTA conditions. The solid lines indicate calculated diffusion depths

domain-inverted regions interact with each other when they are close. With short-time RTA, this interaction tends to form deeper structures, which may be caused by the change of the inside electric field due to narrow space between inverted regions.

For $\Lambda = 5.6$ μm and $D = 0.3, 0.4, 0.5$, channel waveguides of width $w = 4$ μm were also fabricated using 4 s anneal at 607°C. Similar vertical mode sizes were measured at $\lambda = 860$ nm in these waveguides as compared to the planar waveguides in Table 5.2. Due to the lack of appropriate equipment, the experimental test for DBR could not be performed in these channel waveguides.

In summary, we have shown that short-time RTA for less than 6 s at temperatures from 560-610°C is crucial for one-step fabrication of QPM waveguide with comparable domain-inversion depth and waveguide size.

5.3 QPM-SHG demonstration

In order to show the quality of the fabrication process developed in the previous section, sample 1 in Table 5.2 has been tested for QPM-SHG of blue light. For the SHG experiment, a CW tunable Ti:Al_2O_3 laser was used as the source for the fundamental radiation at $\lambda \sim 0.86$ μm. A 0.4 N.A. lens was used for input coupling to the 0.55 mm long waveguide sample. The waveguide supported the TM_0 mode at both fundamental and harmonic wavelengths. With 130 mW of power at 856 nm measured at the waveguide output, we observed the generation of 3.5 μW of 428 nm radiation in the blue TM_0 mode. Fig. 5.5(a) and 5.5(c) show the guided TM_0 modes at the fundamental wavelength 856 nm and

the SH wavelength 428 nm, respectively. Using the model that we developed in this the-

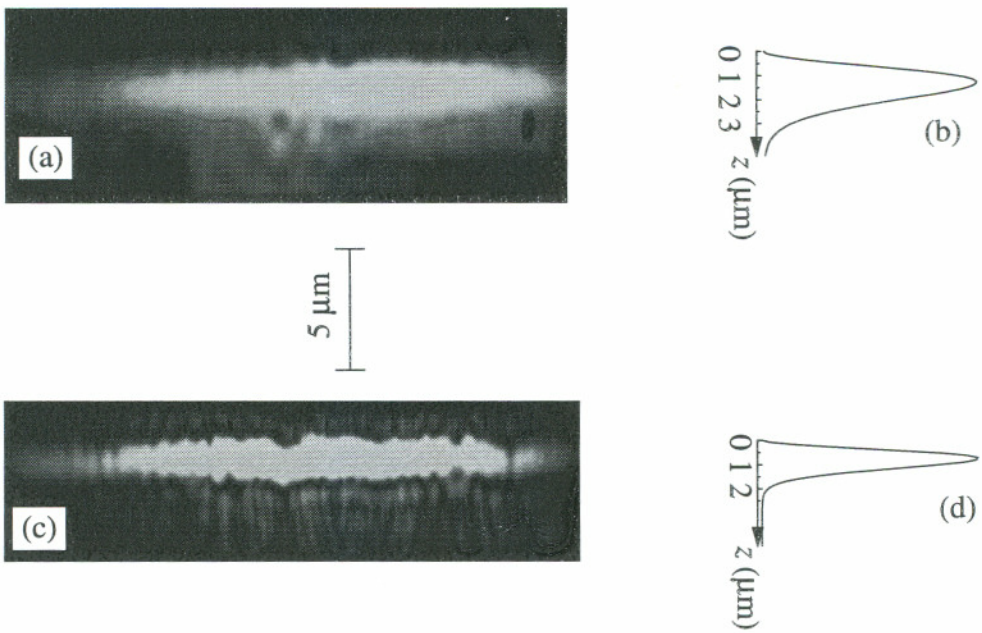

Figure 5.5 Measured and calculated fundamental and SH mode intensity profiles in the fabricated QPM planar waveguide: (a) Guided TM_0 mode profile (856 nm wavelength) exhibiting a $1/e^2$ mode size of 2.6 μm; (b) Calculated mode profile at wavelength of 856 nm (M = 1.086, χ = 0.9848); (c) Guided TM_0 mode profile (428 nm wavelength) exhibiting a $1/e^2$ mode size of 1.7 μm; (d) Calculated mode profile at wavelength of 428 nm (M = 1.086, χ = 0.9848, r = 1.36).

sis, the calculated mode intensity distributions at λ = 856 nm and λ = 428 nm (assuming the dispersion parameter defined by eq. (3.27) is 1.36, as in $LiNbO_3$) have also been shown in Fig. 5.5(b) and 5.5(d) respectively. It can be seen that they match well to the measured mode images.

Figure 5.6 displays the measured wavelength tuning curve. Using the bulk index data for $LiTaO_3$ according to relation (2.16), the theoretical wavelength tuning bandwidth $\delta\lambda$ for frequency doubling of 0.856 μm is calculated from eq. (2.14) to be 1.6 nm for a

physical length of 0.55 mm. By inserting the measured $\delta\lambda = 2.5$ nm into eq. (2.14), i.e. the FWHM acceptance bandwidth of the measured phase-matching curve (FWHM = 2.5 nm), thus indicates an *effective* interaction length of 0.35 mm. Using eq.(2.4) the length-normalized conversion efficiency is calculated as 7%/Wcm^2 for the physical length of 0.55 mm or 11%/Wcm^2 for the effective length of 0.35 mm.

The domain-inversion structure, as had been shown in Fig. 4.8(a), has almost straight domain walls, a duty cycle of ~0.75 (ideal for second-order gratings), and an inversion depth of 2.2 μm that matches the mode sizes very well. This QPM structure optimizes the device so that the length-normalized conversion efficiency can be calculated from eq. (2.12). The measured $1/e^2$ mode sizes in this waveguide at the fundamental and second-harmonic wavelength, respectively, are 2.6 μm and 1.7 μm (Fig. 5.5), which results in almost maximum mode interaction in the depth direction with domain-inversion

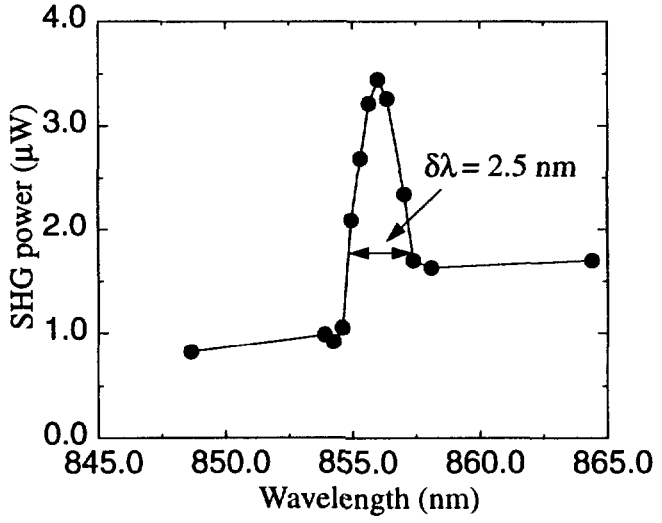

Figure 5.6 QPM-SHG tuning curve obtained with the PS planar $LiTaO_3$ waveguide of sample 1 in Table 5.2.

depth as 2.2 μm. Since the effective mode interaction area in a planar waveguide is expected to be much larger without the mode confinement laterally, an increase of normalized conversion efficiency should be expected in a channel waveguide with lateral confinement. For example, if a channel waveguide with $w = 4$ μm is fabricated using the same process, it can be calculated by using our model in section 3.2 that $A_{eff} = 17.3$ μm^2. A maximum efficiency of 105%/Wcm^2 is then predicted in a 2nd-order QPM channel waveguide. Although we cannot provide a direct comparison of the measured efficiency in the planar guide to a theoretical prediction for a channel waveguide, an 11%/Wcm^2 efficiency is already quite promising in a planar waveguide, in which, we believe, strongly confined modes and fairly deep domain-inverted structure with near-straight domain walls and ~0.75 duty cycle have played important roles.

The tuning curve for the SHG power in Fig. 5.6 exhibits unexplained tails on both sides. It is possible that this phenomenon is related to the lateral divergence of the light in the planar waveguide and its influence on the tuning condition.

Figure 5.7 shows the photographs of blue-light generation in this QPM waveguide. The upper photo was taken with a filter allowing the infrared light into the video camera, and the lower photo shows the blue light generated in the waveguide and out of the waveguide. This photo was taken with a blue-light filter in front of the video camera.

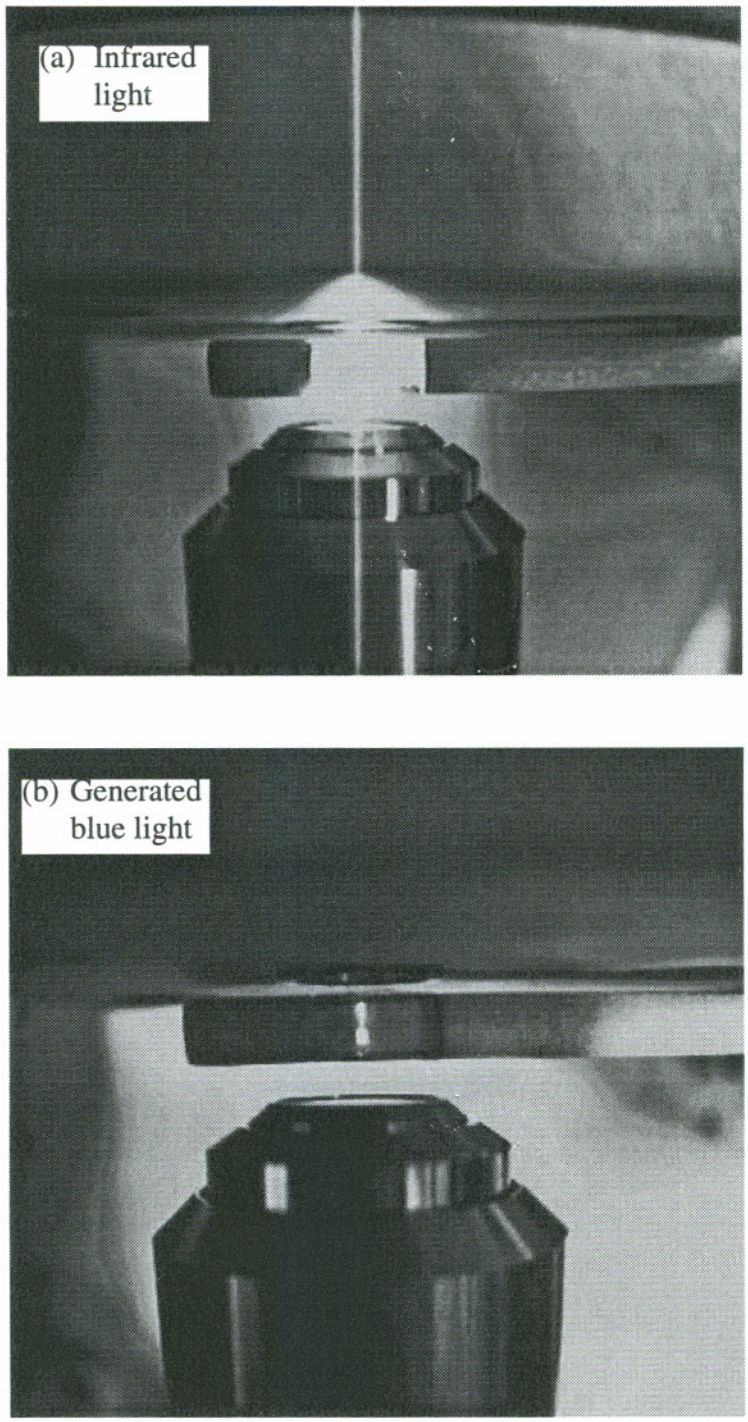

Figure 5.7 Photographs of showing QPM-SHG of blue light in the fabricated $LiTaO_3$ waveguide.

5.4 Summary and conclusions

Strongly confining waveguides on PE -c $LiTaO_3$ surfaces have been fabricated by high-temperature (540-610°C), short-time (6-12 s) RTA. A relationship between the index increase and the proton concentration in the PE $LiTaO_3$ layer has been deduced based on our experimental measurement of mode sizes, which is also found consistent with published data for an α-phase $H_xLi_{1-x}TaO_3$ system. This relationship allows the model which we developed in section 3.2 to simulate any well-annealed and strongly confined APE channel waveguides in $LiTaO_3$ with given PE and annealing conditions.

A single-step photolithography process, simultaneously producing periodic domain inversion and a well matched optical waveguide, has been successfully demonstrated for the fabrication of QPM waveguides in $LiTaO_3$. A maximum of 3.5 μW of blue light was generated in the TM_0 mode in a planar-waveguide sample for a fundamental power of 130 mW in the waveguide, resulting in a length-normalized conversion efficiency of 7%/Wcm^2 for a physical length of 0.55 mm (11%/Wcm^2 for the effective length of 0.35 mm).

Future work can be focused on one-step fabrication of 1st- and 2nd-order QPM channel waveguides in $LiTaO_3$ for blue-light generation. Already with a 2nd-order grating a 1 cm long channel waveguide with an expected efficiency in the range 7-107%/Wcm^2 would produce 0.7-10.7 mW of blue light from 100 mW of infrared input radiation. Using a 1st-order grating promises a further increase of efficiency by a factor of 4.

PS channel waveguides with $\Lambda = 5.6$ μm, $D = 0.3, 0.4, 0.5$, and $w = 4$ μm have also been fabricated and tested. However, more work needs to be done to characterize the DBR properties in these waveguides.

Chapter 6

SUMMARY, CONCLUSIONS, AND SUGGESTIONS

The goal of this research project was to design, investigate, develop, and fabricate a blue or green laser source using frequency conversion of infrared laser diode output and QPM waveguide scheme. Contrary to big-size solid-state lasers, this laser source needs to be compact, low cost, and efficient so that it is practically viable. Since the start of this project in September, 1992, several advancements, also the major contributions of this dissertation, have been made aiming at realizing such a device.

A proposed configuration of a compact QPM $LiTaO_3$ waveguide device taking into account the material properties and the developed fabrication processes has been shown to have the following advantages: (1) Devices are compact due to coplanar-mounting and butt-coupling; (2) Fabrication tolerances are greatly eased due to broadband QPM; (3) Temperature tuning is not necessary due to broadband QPM; (4) TM mode DBR only excites TM modes of the laser diode due to APE waveguides; (5) Devices should have excellent mechanical stability.

Theoretical modeling and characterization of APE uniform waveguides in z-cut $LiTaO_3$ has been performed. Analytical expressions for the mode indices and mode field profiles in APE channel waveguides have been shown to be related to PE and RTA condi-

tions. This modeling lead to the determination of the relationship of the index increase and the proton concentration using data from experimental RTA conditions as obtained in chapter 5 so that waveguide design can be performed with given PE and RTA conditions.

The investigation on analyzing and understanding of PS waveguides has resulted with a simplified method of simulating the properties of these waveguides necessary for quick device design. It has been found that the model results fit well to the experimental data reported recently by others for KTP waveguides. A mode index N_{high} in the ion-exchanged sections and an average index N_{low} in the substrate index sections of a PS channel waveguide have been introduced for calculating the DBR reflectivity directly from the PS waveguide parameters. This method also allows to predict the QPM and DBR wavelengths. Additionally, by measuring the QPM wavelength and DBR wavelength (or DBR reflectivity performance), the waveguide parameters can be easily determined. The outlined method will allow a quick design for DBR and QPM waveguide devices for even more complicated device structures.

Another advancement of the state-of-the-art was the first-time realization of high-quality short-period domain-inverted structures in $LiTaO_3$ by using benzoic rather than pyrophosphoric acid for proton exchange followed by RTA. The Curie temperature (T_c = 610°C) of $LiTaO_3$ is decreased by PE since it lowers the Li content. Because of its high dissociation constant (Ka = 2 x 10^{-2}), which is proportional to proton concentration in the acid, compared to benzoic acid (Ka = 6.2 x 10^{-5}), pyrophosphoric acid as PE source will allow higher proton content, and lower Li content. But, there was no obvious drawback been found for using benzoic acid as PE source, which, on the contrary, has the advantage

of allowing more metals to be used as the selective mask, and, thus, makes fabrication more flexible. And also, benzoic acid is less expensive.

During the domain inversion fabrication processes, domain formation behavior has been investigated based on the new observation of a double-layer of single domains with opposing polarizations forming on both c faces by RTA of proton-exchanged z-cut $LiTaO_3$ at above T_c. Depending on the RTA temperature and time either one single-domain layer is formed on each of the two c-faces (very short anneal), or a double-layer of two single domains with opposite polarization appears on each c face (somewhat longer anneal). Homogeneous multidomains are formed when annealing time is extended further. Very long anneal time generates shallow single-domain layers again. The results indicate that an internal electric field with inward direction close to the c face and outward direction somewhat deeper inside the substrate has formed at the early stage of RTA of proton-exchanged multidomain $LiTaO_3$. The observations have been discussed in relation to recently proposed models for the domain-inversion mechanism in $LiTaO_3$ and $LiNbO_3$.

One of the more significant discoveries is the realization of the importance of short-time RTA (~6-12 s) for reducing lateral domain growth and achieving near-straight domain walls so that high-quality QPM structures can be fabricated. A direct result of this realization is the discovery of utilizing the added step of pre-annealing at lower temperatures (<480°C) before the short-time RTA process to reduce lateral domain spreading for deep QPM structures, especially in case of short-period structures. A possible mechanism of this process has also been discussed based on the inside-field model. Domain-inverted structures with near-straight domain walls and inversion depths as deep as 2.2 μm for the

second-order gratings, and 3.3 μm for the third-order gratings have been realized by proton exchange in benzoic acid followed by RTA without pre-annealing process. With pre-annealing process, high-quality QPM structures with depth of 2.2 μm for the first-order gratings have been fabricated.

Perhaps the most significant discovery was the first fabrication of strongly confining waveguides on proton exchanged -c $LiTaO_3$ surfaces at very-high-temperature close to Curie temperature T_c (540-610°C) by short-time (6-12 s) RTA. It was demonstrated that single-step photolithography process, simultaneously producing periodic domain inversion and a well matched optical waveguide, is sufficient to fabricate QPM waveguides in $LiTaO_3$. Using such a waveguide SHG of 428 nm blue light has been demonstrated in strongly confined TM_0 modes ($1/e^2$ mode sizes fundamental and SH wavelength, respectively, are 2.6 μm and 1.7 μm). The measured normalized conversion efficiency is 7%/Wcm^2. Although it is impossible to provide a direct comparison of the measured efficiency in the planar guide to a theoretical prediction, 7%/Wcm^2 efficiency is already quite promising in a planar waveguide, in which, it is believed, strongly confined modes and fairly deep domain-inverted structure with near-straight domain walls and ~0.75 duty cycle have played important roles. A substantial increase of normalized conversion efficiency, theoretically as high as 107%/Wcm^2, should be expected in a channel waveguide with lateral mode confinement.

In order to realize the compact, low-cost device configuration shown in Fig. 2.9, fabrication of DBR waveguides in $LiTaO_3$ becomes the key process since the fabrication of broadband QPM waveguides in $LiTaO_3$ was already demonstrated [64]. The single-step fabrication at high temperatures developed in this thesis work is used for this fabrication

because of its simplicity. Using this process PS channel waveguides with a period of 5.6 μm in $LiTaO_3$ were fabricated with domain structures having depths of 2.5-3.0 μm and duty cycle of 0.45-0.58. These waveguides have the periods appropriate for 1st-order QPM at wavelength of 980 nm. Unfortunately, due to the limited access to high-quality measurement equipment with single-longitudinal mode and wide-range tunibility (such as a single mode CW $Ti:Al_2O_3$ laser) for DBR properties, the test experiment could not be carried out to find out whether there is DBR reflection in these waveguides or not.

In the follow-up work, the DBR-test experiment needs to be done to characterize those PS channel waveguides mentioned above. Based on its results further investigation needs to be carried out to further characterize and optimize PE and/or RTA processes. For instant, if no DBR reflection or little reflection were observed in those PS channel waveguides, one recommended change of the fabrication conditions could be to increase PE time and decrease Ti-mask duty cycles so that proton-diffusion overlapping is reduced. The annealing for domain-inversion structures can also be performed at lower temperatures or with shorter times. In addition, the fabrication of broadband QPM waveguides using the one-step process needs to be demonstrated and optimized. Finally, optimization and adjustments need to be performed to allow the fabrication of broadband QPM and DBR structures with the same PE and annealing conditions

An obvious alternate way of realizing the device configuration of Fig. 2.9 is to use a two-step process as is now common for regular QPM waveguides in $LiTaO_3$. First, fabricate broadband QPM at high temperatures; secondly, fabricate the uniform waveguide in the broadband QPM region and the DBR structures at lower temperatures.

Another way of realizing DBR structures can be mechanically etching off materials on the surface to form a periodically perturbed waveguide, which would give advantages to allow optimization of QPM structure and DBR structures separately.

REFERENCES

[1] S. Taniguchi, T. Hino, S. Itoh, K. Nakano, N. Nakayama, A. Ishibashi, and M. Ikeda, "100 h II-VI blue-green laser diode," Electronic. Lett., vol. 32, pp. 552-553, 1996.

[2] S. Nakamura, M. Senoh, S. Nagahama, N. Iwasa, T. Yamada, T. Matsushita, H. Kiyoku, and Y. Sugimoto, "InGaN multi-quantum-well-structure laser diodes with cleaved mirror cavity facets," Jpn. J. Appl. Phys., vol. 35, Part 2, pp. L217-220, 1996.

[3] D. W. Nam and R. G. Waarts, "Advanced laser diodes bring compact blue-green sources to light," Laser Focus World, vol. 30, no. 8, pp. 49-55, August 1994.

[4] J. A. Armstrong, N. Bloembergen, J. Ducuing, and P. S. Pershan, "Interaction between light waves in a nonlinear dielectric," Phys. Rev., vol. 127, pp. 1918-1939, 1962.

[5] N. Bloembergen, A. J. Sievers, "Nonlinear optical properties of periodic laminar structures," Appl. Phys. Lett., vol. 17, pp. 483, 1970.

[6] S. Somekh and A. Yariv, "Phase matching by periodic modulation of the nonlinear optical properties," Opt. Commun. vol. 6, pp. 301, 1972.

[7] G. A. Magel, M. M. Fejer, and R. L. Byer, "Quasi-phase-matched second harmonic generation of blue light in periodically poled $LiNbO_3$," Appl. Phys. Lett., vol. 56, pp. 108, 1990.

[8] D. E. Thompson, J. D. McMullen, and D. B. Anderson, "Second-harmonic generation in GaAs 'stack of plates' using high power CO_2 radiation," Appl. Phys. Lett., vol. 29, pp. 113, 1976.

[9] A. Feisst and P. Koidl, "Current induced periodic ferroelectric domain structures in LiNbO3 applied for nonlinear optical frequency mixing," Appl. Phys. Lett., vol. 47, pp. 1125, 1985.

[10] D. Feng, N. -B. Ming, J. -F. Hong, Y. -S. Zhu, Z. Yang, and Y. -N. Wang, "Enhancement of second-harmonic generation in $LiNbO_3$ crystals with periodic laminar ferroelectric domains," Appl. Phys. Lett., vol. 37, pp. 607, 1980.

[11] Y. -H. Xue, N. -B. Ming, J. -S. Zhu, and D. Feng, "The second harmonic generation in $LiNbO_3$ with periodic laminar ferroelectric domains," Chin. Phys., vol. 4, pp. 554, 1984.

[12] J. Webjörn, F. Laurell, and G. Arvidsson, "Blue light generated by frequency doubling of laser diode light in a lithium niobate channel waveguide," IEEE Photonics

Technol. Lett. vol 1, pp. 316, 1989.

[13] E. J. Lim, M. M. Fejer, and R. L. Byer, "Second-harmonic generation of green light in periodically poled planar lithium niobate waveguide," Electron. Lett., vol. 25, pp. 174, 1989.

[14] J. Webjörn, F. Laurell, and G. Arvidsson, "Fabrication of periodically domain-inverted channel waveguides in lithium niobate for second harmonic generation," J. Lightwave Technol., vol 7, pp. 1597, 1989.

[15] E. J. Lim, M. M. Fejer, and R. L. Byer, "Blue light generation by frequency doubling in periodically poled lithium niobate channel waveguide", Electron. Lett., vol. 25, pp. 731, 1989.

[16] H. Åhlfeldt, J. Webjörn, and G. Arvidsson, "Periodic domain inversion and generation of blue light in lithium tantalate waveguides", IEEE Photon. Technol. Lett., vol. 3, pp. 638-639, 1991.

[17] K. Mizuuchi, K. Yamamoto, and T. Taniuchi, "Second-harmonic generation of blue light in a $LiTaO_3$ waveguide," Appl. Phys. Lett., vol. 58, pp. 2732, 1991.

[18] C. J. van der Poel, J. D. Bierlein, J. B. Brown, and S. Colak, "Efficient type I blue second-harmonic generation in periodically segmented $KTiOPO_4$ waveguides," Appl. Phys. Lett., vol. 57, pp. 2074, 1990.

[19] R. A. Norwood and G. Khanarian, "Quasi-phase-matched frequency doubling over 5 mm in periodically poled polymer waveguide," Electron. Lett., vol. 26, pp. 2105, 1990.

[20] M. A. Mortazavi and G. Khanarian, "Quasi-phase-matched frequency doubling in bulk periodic polymeric structures," Opt. Lett., vol. 19, pp. 1290, 1994.

[21] T. Suhara, T. Moromoto, and H. Nishihara, "Optical second-harmonic generation by quasi-phase matching in channel waveguide using organic molecular crystal," Photon. Technol. Lett., vol. 5, pp. 934, 1993.

[22] P. S. Weitzman, J. J. Kester, and U. Österberg, "Electric field induced second harmonic generation in germanium doped silica planar waveguides," Electron. Lett., vol. 30, pp. 697, 1994.

[23] A. S. Kewitsch, M. Segev, A. Yariv, G. J. Salamo, T. W. Towe, E. J. Sharp, and R. R. Neurgaonkar, "Tunable quasi-phase matched using dynamic ferroelectric domain gratings induced by photorefractive space-charge fields," Appl. Phys. Lett., vol. 64, pp. 3068, 1994.

[24] M. L. Bortz, M. A. Arbore, and M. M. Fejer, "Quasi-phase-matched optical parametric amplification and oscillation in periodically poled $LiNbO_3$ waveguides," Opt. Lett., vol. 20, pp. 49-51, 1995.

[25] Q. Chen and W. P. Risk, "Periodic poling of $KTiOPO_4$ using an applied electric field," Electron. Lett. vol. 30, pp. 1516-1517, 1994.

[26] K. Mizuuchi and K. Yamamoto, "Harmonic blue light generation in bulk periodically poled $LiTaO_3$," Appl. Phys. Lett., vol. 66, pp. 2943-2945, 1995.

[27] S. Somkeh and A. Yariv, "Phase matching by periodic modulation of the nonlinear optical properties," Opt. Commun., vol. 57, pp. 2540-2542, 1990.

[28] Y. Yacoby, R. L. Aggarwal, and B. Lax, "Phase matching by periodic variation of nonlinear coefficients," J. Appl. Phys., vol. 44, pp. 3180-3181, 1973.

[29] J. D. McMullen, "Optical parametric interactions in isotropic materials using a phase-corrected stack of nonlinear dielectric plates," J. Appl. Phys., vol. 46, pp. 3076-3081, 1975.

[30] A. Yariv and P. Yeh, "Electromagnetic propagation in periodic stratified media. II. Birefringence, phase matching, and x-ray lasers," J. Opt. Soc. Amer., vol. 67, pp. 438-448, 1977.

[31] R. C. Alferness, S. K. Korotky, and E. A. J. Marcatili, "Velocity-matching techniques for integrated optic traveling wave switch/modulators," IEEE J. Quantum Electon., vol. QE-20, pp. 301-309, 1984.

[32] B. Jaskorzynska, G. Arvidsson, and F. Laurell, "Periodic structures for phase-matching in second harmonic generation in titanium lithium niobate waveguides," in Integrated Optical Circuit Engineering III, Proc. SPIE vol. 651, pp. 221-228, 1986.

[33] M. M. Fejer, G. A. Magel, and E. J. Lim, in Nonlinear Optical Properties of Materials, edited by H. R. Schlossberg and R. V. Wick, Proc. SPIE vol. 1148, pp. 213, 1989.

[34] G. Arvidsson and B. Jaskorzynska, "Periodically domain-inverted waveguides in lithium niobate for second harmonic generation: influence of the shape of the domain boundary on the conversion efficiency," Intern. Conf. on Materials for Non-linear and Electo-optics, Cambridge, UK, 1989, Int. Phys. Conf. Se. No. 103, pp. 47, 1989.

[35] H. Åhlfeldt, G. Arvidsson, and B. Jaskorzynska, "Quasi-phase-matched second harmonic generation in lithium tantalate waveguides: experiments and simulations," in Proceeding Nonlinear Guided Wave Phenomena, OSA 1991 Technical Digest Series 15, pp. 230-233. 1991.

[36] M. M. Fejer, G. A. Magel, D. H. Jundt, and R. L. Byer, "Quasi-phase-matched second harmonic generation: tuning and tolerances," IEEE J. Quantum Electron., vol. QE-28, pp. 2631-2654, 1992.

[37] D. H. Jundt, M. M. Fejer, and R. L. Byer, "Optical properties of lithium-rich lithium niobate fabricated by vapor transport equilibration," IEEE J. Quantum Electron., vol. 26, pp. 135-138, 1990.

[38] T. Y. Fan, C. E. Huang, B. Q. Hu, R. C. Eckardt, Y. X. Fan, R. L. Byer, and R. S. Feigelson, "Second harmonic generation and accurate index of refraction measurements in flux-grown $KTiOPO_4$," Appl. Opt., vol. 26, pp. 2390-2394, 1987.

[39] J. J. Bierlein, and H. Vanherzeele, "Potassium titanyl phosphate: properties and new applications," J. Opt. Soc. Am., vol. B6, no. 4, pp. 622-633, 1989.

[40] Data sheet, "Optical crystals, Lithium Niobate, Lithium Tantalate," Crystal Technology Inc., 1035 East meadow Circle, Palo, Alto, California 94303, USA.

[41] K. Yamamoto, K. Mizuuchi, and T. Taniuchi, "Milliwatt-order blue-light generation in a periodically domain-inverted $LiTaO_3$ waveguide," Opt. Lett., vol. 15, pp. 1156-1158, 1991.

[42] G. T. Boyd, "Applications requirements for nonlinear-optical devices and the status of organic materials," J. Opt. Soc. Am. B, vol. 6, pp. 685-692, 1989.

[43] Y. Suematsu, Y. Sasaki, K. Furuya, K. Shibata, and S. Ibukuro, "Optical second-harmonic generation due to guided-wave structure consisting of quartz and class film," IEEE J. Quantum Electron. vol. QE-10, pp. 222-229, 1974.

[44] M. M. Choy and R. L. Byer, "Accurate second-order susceptibility measurements of visible and nonlinear crystals," Phys. Rev., vol. B 14, pp. 1693, 1976.

[45] A. Ashkin, G. D. Boyd, J. M. Dziedzic, R. G. Smith, A. A. Ballman, J. J. Levinstein, and K. Nassau, "Optically-induced refractive index inhomogeneities in $LiNbO_3$ and $LiTaO_3$," Appl. Phys. Lett., vol. 9, pp. 72, 1966.

[46] A. M. Glass, "The photorefractive effect," Opt. Eng., vol. 17, pp. 470, 1978.

[47] D. M. Pepper, J. Feinberg, and N, V. Kuhktarev, "The photorefractive effect," Scientific American, vol. 263, no. 4, pp. 62, October 1990.

[48] M. Yamada, N. Nada, M. Saitoh, and K. Watanabe, "First-order quasi-phase matched $LiNbO_3$ waveguide periodically poled by applying an external field for efficient blue second-harmonic generation," Appl. Phys. Lett., vol. 62, pp. 435-436, 1993.

[49] J. D. Bierlein, "Second order nonlinear optical processes in $KTiOPO_4$ waveguides," in Guided Wave Nonlinear Optics, edited by D. B. Ostrowsky and R. Reinisch, Kluwer Academic, Dordrecht, 1992, pp. 49.

[50] D. Eger, M. Oron, M. Katz, and A. Zussman, "Highly efficient blue light genera-

tion in $KTiOPO_4$ waveguides," Appl. Phys. Lett., vol. 64, pp. 3208-3209, 1994.

[51] Q. Chen and W. P. Risk, "High-efficiency quasi-phase-matched waveguide device fabricated in $KTiOPO_4$ by electric-field poling," Technical Digest of the Conference on Lasers and Electro-Optics (CLEO), paper CFA2, pp. 370-371, 1995.

[52] K. Yamamoto, K. Mizuuchi, Y. Kitaoka, and M. Kato, "High power blue light generation by frequency doubling of a laser diode in a periodically domain-inverted $LiTaO_3$ waveguide," Appl. Phys. Lett., vol. 62, pp. 2599-2601, 1993.

[53] W. P. Risk, W. J. Kozlovsky, S. D. Lau, G. L. Bona, H. Jaeckel, and D. J. Webb, "Generation of 425-nm light by waveguide frequency doubling of a GaAlAs laser diode in an external-cavity configuration", Appl. Phys. Lett., vol. 63, pp. 3134-3136, 1993.

[54] K. Shinozaki, T. Fukunaga, K. Watanabe, and T. Kamijoh, "Self-quasi-phase-matched second-harmonic generation in the proton-exchanged $LiNbO_3$ optical waveguide with periodically domain-inverted regions," Appl. Phys. Lett., vol. 59, pp. 510-512, 1991.

[55] M. G. Roelofs, W. Bindloss, A. Suna, J. D. Lee, and J. D. Bierlein, "KTP Segmented waveguides as concurrent Bragg reflectors and second harmonic generators," OSA, Compact Blue-Green Laser Topical Meeting, New Orleans, 3-4 Feb. 1993.

[56] W. P. Risk, and S. D. Lau, "Distributed-Bragg-reflection properties of segmented KTP waveguides," Opt. Lett., vol. 18, pp. 272-274, 1993.

[57] W. P. Risk, S. D. Lau, and M. A. McCord, "Third-order guided-wave distributed Bragg reflectors fabricated by ion-exchange in $KTiOPO_4$," IEEE Photonics Technol. Lett., vol. 6, pp. 406-408, 1994.

[58] D. Eger, M Oren, and M. Katz, "Optical characterization of $KTiOPO_4$ periodically segmented waveguides for second-harmonic generation of blue light," J. Appl. Phys., vol. 24, pp. 4298-4302, 1993.

[59] K. Yamamoto, K. Mizuuchi, and T. Taniuchi, "Quasi-phase-matched second harmonic generation in a $LiTaO_3$ waveguide," IEEE J. Quantum Electron., vol. 28, pp. 1909-1914, 1992.

[60] H. Iwasaki, T. Yamada, N. Niizeki, H. Toyoda, and H. Kubota, "Refractive indices of $LiTaO_3$ at high temperatures," Japan. J. Appl. Phys., vol. 7, pp. 185-186, 1968.

[61] T. Suhara and H. Nishihara, "Theoretical analysis of waveguide second-harmonic generation phase matched with uniform and chirped grating," IEEE J. Quantum Electron., vol. 26, pp. 1265-1276, 1990.

[62] M. Nazarachy and D. W. Dolfi, "Spread-spectrum nonlinear-optical interaction: quasi-phase matching with pseudorandom polarity reversals," Opt. Lett., vol. 12, pp. 823-835, 1987.

[63] M. L. Bortz, M. Fujimura, and M. M. Fejer, "Increased acceptance bandwidth for quasi-phasematched second harmonic generation in $LiNbO_3$ waveguides," Electron. Lett. vol. 30, pp. 34-35, 1994.

[64] K. Mizuuchi, K. Yamamoto, M. Kato, and H. Sato, "Broadening of the phase-matching bandwidth in quasi-phase-matched second-harmonic generation," IEEE J. Quantum Electron., vol. 30, pp. 1596-1604, 1994.

[65] J. Wu, C. -Q. Xu, H. Okayama, M. Kamahara, T. Kondo, and R. Ito, "Broad-band second-harmonic generation in $LiNbO_3$ waveguide using optimized domain-inverted grating," Jpn. J. Appl. Phys. Part 2, vol. 33, pp. L1163-L1166, 1994.

[66] J. M. Chwalek, "Forced TM-mode operation of a GaAlAs laser diode by use of annealed proton-exchanged $LiNbO_3$ and $LiTaO_3$ waveguides," Opt. Lett., vol. 20, pp. 186-188, 1995.

[67] J. D. Bierlein, A. Ferretti, L. H. Brixner, and W. Y. Hsu, "Fabrication and characterization of optical waveguides in $KTiOPO_4$," Appl. Phys. Lett., vol. 50, pp. 1216-1218, 1987.

[68] N. Anastassopoulou and G. M. Davis, "Characterization of benzoic acid ion exchange waveguides in lithium tantalate," Appl. Phys. Lett., vol. 66, pp 2295-2297, 1995.

[69] C. E. Rice and J. L. Jackel, "Structural changes with composition and temperature in rhombohedral $Li_{1-x}H_xNbO_3$," Mater. Res. Bull., vol. 19, pp. 591, 1984

[70] S. Chen, P. Baldi, M. De Micheli, D. B. Ostrowsky, A. Leycuras, G. Tartarini, and P. Bassi, "Loss mechanisms and hybrid modes in high-δn_e proton-exchanged planar waveguides," Opt. Lett., vol. 18, pp. 1314, 1993.

[71] P. J. Matthews, A. R. Mickelson, and S. W. Novak, "Properties of proton exchange waveguides in lithium tantalate," J. Appl. Phys., vol. 72, pp. 2562-2574, 1992.

[72] W. Charczenko, P. S. Weitzman, H. Klotz, M. Surette, J. M. Dunn, and A. R. Mickelson, "Characterization and simulation of proton exchanged integrated optical modulators with various dielectric buffer layers," J. Lightwave Technol., vol. 9, pp. 92-100, 1991.

[73] V. A. Fedorov and Yu. N. Korkishko, "Crystal structure and optical properties of proton-exchanged $LiTaO_3$ waveguide," Ferroelectrics, vol. 160, pp. 185-208, 1994.

[74] K. El Hadi, P. Baldi, S. Nouh, M. P. De Micheli, A. Leycuras, V. A. Fedorov, and Yu. N. Korkishko, "Control of proton exchange for $LiTaO_3$ waveguides and the crystal structure of $H_xLi_{1-x}TaO_3$," Opt. Lett., vol. 20, pp. 1698-1670, 1995.

[75] R. M. Knox and P. P. Toulios, "Integrated circuits for the millimeter through optical frequency range," in Proc. MRI Symp. on Submillimeter Waves, J. Fox, Ed. Brooklyn, NY: Polytechnic Press, 1970.

[76] E. Strake, G. P. Bava, and I. Montrosset, "Guided modes of $LiNbO_3$ channel waveguides: A novel quasi-analytical technique in comparison with the scalar finite-element method," J. Lightwave Technol., vol. 6, pp. 1126-1135, 1988.

[77] X. Cao, J. Natour, R. V. Ramaswamy, and R. Srivastava, "Effect of waveguide uniformity on phase matching for frequency conversion in channel waveguides," Appl. Phys. Lett., vol., 58, pp. 2331-2333, 1991.

[78] M. Abramovitz and I. Stegun. Handbook of Mathematical Functions. New York: Dover, 1972, ch.22.

[79] L. Li and J. J. Burke, "Linear propagation characteristics of periodically segmented waveguides," Opt. Lett., vol. 17, pp. 1195-1197, 1992.

[80] Z. Weissman and A. Hardy, "Modes of periodically segmented waveguides," J. Lightwave Technol., vol. 11, pp. 1831-1838, 1993.

[81] D. Marcuse, Light Transmission Optics. New York: Holt, Reinhart and Winston, 1985, ch. 5.

[82] A. Yariv and P. Yeh, Optical Waves in Crystals. John Wiley & Sons, New York, 1984, ch. 6.

[83] W. P. Risk, "Fabrication and characterization of planar ion-exchanged $KTiOPO_4$ waveguides for frequency doubling," Appl. Phys. Lett., vol. 58, pp. 19-21, 1991.

[84] K. Nakamura and H. Shimizu, "Ferroelectric inversion layers formed by heat treatment of proton-exchanged $LiTaO_3$," Appl. Phys. Lett., vol. 56, pp. 1535-1536, 1990.

[85] K. Mizuuchi and K. Yamamoto, "Characteristics of periodically domain-inverted $LiTaO_3$," J. Appl. Phys. vol., 72, pp. 5061-5069, 1992.

[86] K. Mizuuchi and K. Yamamoto, "Domain inversion in $LiTaO_3$ using proton exchange followed by heat treatment," J. Appl. Phys., vol. 75, pp. 1311-1318, 1994.

[87] K. Yamamoto and T. Taniuchi, "Characteristics of pyrophosphoric acid proton-exchanged waveguides in $LiNbO_3$," J. Appl. Phys., vol. 70, pp. 6663-6668, 1991.

[88] N. Ohnishi, "An etching study on a heat-induced layer at the positive-domain surface of $LiTaO_3$," Jpn. J. Appl. Phys., vol. 16, pp. 1069, 1977.

[89] K. Nakamura, H. Ando, and H. Shimizu, "Ferroelectric domain inversion caused in $LiNbO_3$ plates by heat treatment," Appl. Phys. Lett., vol. 50, pp. 1413-1414, 1987.

[90] S. Miyazawa, "Ferroelectirc domain inversion in Ti-diffused $LiNbO_3$ optical waveguide," J. Appl. Phys., vol. 50, pp. 4599-4603, 1979.

[91] K. Nakamura and H. Shimizu, "Ferroelectric inversion layers formed by heat treatment of proton-exchanged $LiTaO_3$," Appl. Phys. Lett., vol. 56, pp. 1535, 1990.

[92] H. Åhlfeldt, "Single-domain layers formed in heat-treated $LiTaO_3$," Appl. Phys. Lett., vol. 64, pp. 3213-3215, 1994.

[93] M. Tasson, H. Legal, J. C. Peuzin, and F. C. Lissalde, "Mécanismes d'orientation de la polarization spontanée dans le niobate de lithium au voisinage du point de Curie," Phys. Status Solidi A, vol. 31, pp. 729, 1975.

[94] V. D. Kugel and G. Roseman, "Domain inversion in heat-treated $LiNbO_3$ crystals," Appl. Phys. Lett., vol. 62, pp. 2902-2904, 1993.

[95] L. Huang and N. A. F. Jaeger, "Discussion of domain inversion in $LiNbO_3$," Appl. Phys. Lett., vol. 65, pp. 1763-1765, 1994.

[96] K. Mizuuchi, K. Yamamoto, and H. Sato, "Fabrication of periodic domain inversion in an x-cut $LiTaO_3$," Appl. Phys. Lett., vol. 62, pp. 1860-1862, 1993.

[97] K. Nakamura and A. Tourlog, "Single-domain surface layers formed by heat treatment of proton-exchanged multidomain $LiTaO_3$ crystals," Appl. Phys. Lett., vol. 63, pp. 2065-2066, 1993.

[98] H. Åhlfeldt and J. Webjorn, "Single-domain layers formed in multidomain $LiTaO_3$ by proton exchange and heat treatment," Appl. Phys. Lett., vol. 64, pp. 7-9, 1994.

[99] Y. Zhu, S. Zhu, Z. Zhang, H. Shu, J. Hong, C. Ge, and N. Ming, "Formation of single-domain layers in multidomain $LiNbO_3$ crystals by proton exchange and quick heat treatment," Appl. Phys. Lett., vol. 66, pp. 408-409, 1995.

[100] H. Åhlfeldt, Thesis, "Proton-exchanged lithium tantalate for guided-wave nonlinear optics," Royal Institute of Technology, ISSN 0280-316X, TRITA-FYS 2140, pp. 52, 1994.

[101] S. Zhu, Y. Zhu, Z. Zhang, H. Shu, J. Hong, C. Ge, and N. Ming, "The mechanism for domain inversion in $LiNbO_3$ by proton exchange and rapid heat treatment," J.

Phys.: Condens. Matter, vol. 7, pp. 1437-1440, 1995.

[102] Z. Zhang, Y. Zhu, S. Zhu, H. Shu, H. Wang, J. Hong, C. Ge, and N. Ming, "Study on the formation mechanism of a complex domain structure in $LiNbO_3$," J. Appl. Phys., vol. 77, pp. 4136-4138, 1995.

VITA

Cangsang Zhao was born on December 28th, 1965 in the Province of Gui Zhou, P. R. China. In September, 1984, he enrolled in the Physics Department of Peking University, Beijing, China, and graduated with a B.S. degree in Physics in 1988 and a M.S. degree in Solid-State Physics in 1991.

In September, 1991, he was accepted into Oregon Graduate Institute of Science & Technology in Portland, Oregon, and started working with Dr. Reinhart Engelmann on a Motorola-funded project "Frequency doubling of diode lasers for compact blue-green sources" using quasi-phase-matching waveguides in September, 1992. The work with Dr. Engelmann has led to 6 published papers. In April, 1993, he obtained a M.S.E.E degree. Continuing at the same institution, he worked toward his Ph.D. and completed all requirements for the degree Doctor of Philosophy in Electrical Engineering in May, 1996.

He is leaving to accept a position of senior design engineer at Intel, Hillsboro, Oregon.

List of publications

1. C. Zhao and R. Engelmann, "Short-time rapid thermal annealing processes for periodically domain-inverted structures with nearly straight domain walls in proton-exchanged $LiTaO_3$," SPIE Proceedings on Nonlinear Frequency Generation and Conversion, 1996 (in print).

2. C. Zhao and R. Engelmann, "Double-layers of single domains formed by rapid thermal annealing of proton-exchanged $LiTaO_3$," Appl. Phys. Lett. 67 (13), 25 Sept. 1995.

3. C. Zhao and R. Engelmann, "Pre-annealing for fabrication improvement of short-period domain-inverted structures in $LiTaO_3$," presented at the OSA Annual Meeting/ILS-XI, 10-15 Sept., 1995.

4. C. Zhao and R. Engelmann, "Fabrication of strongly confined waveguides with simultaneous domain inversion by high-temperature rapid thermal annealing of proton-exchanged $LiTaO_3$," Technical Digest, the Conference on Lasers and Electro-Optics (CLEO'95), pp. 371-372, 1995.

5. C. Zhao and R. Engelmann, "Fabrication of periodically domain-inverted structures in $LiTaO_3$ by proton exchange in benzoic acid followed by rapid thermal annealing," OSA Proceedings on Advanced Solid-State Lasers, pp. 63-66, 1995.

6. C. Zhao and R. Engelmann, "Simulation of periodically segmented waveguides as concurrent Bragg reflectors and quasi-phase-matched second-harmonic generators," Proceedings of the Third International Workshop on Computational Electronics, pp. 310-312, 1994.

7. C. Zhao and R. Engelmann, "Single-step fabrication of strongly confining quasi-matching waveguides in $LiTaO_3$," (to be submitted for publication).